Transport dynamics in secondary active glutamate transporters

Inaugural-Dissertation

zur Erlangung des Doktorgrades
der Mathematisch-Naturwissenschaftlichen Fakultät
der Heinrich-Heine-Universität Düsseldorf

vorgelegt von

Felix Niklas Groß-Esser
aus Düsseldorf

Aachen, Februar 2022

Aus dem Institut für Biologische Informationsprozesse
Molekular- und Zellphysiologie (IBI-1)
des Forschungszentrums Jülich

Gedruckt mit der Genehmigung der
Mathematisch-Naturwissenschaftlichen Fakultät der
Heinrich-Heine-Universität Düsseldorf

Berichterstatter:

1. Prof. Dr. Christoph Fahlke

2. Prof. Dr. Holger Gohlke

Tag der mündlichen Prüfung: 19.08.2022

Contents

List of Figures

List of Tables

Chapter 1

Abstract

Clearance of glutamate from the synaptic cleft is a vital component of synaptic signal transmission. Excitatory amino acid transporters (EAATs) are secondary active transporters and feature rapid binding of glutamate and consequent transport into neurons and glial cells surrounding the synaptic cleft. They actively modulate and terminate synaptic signal transmission and keep extracellular glutamate concentration below neurotoxic levels. Under physiological conditions, glutamate flux is cell inward but can be reversed under nonphysiological conditions, including pathological conditions like ischemic, hemorrhagic stroke or malign mutations. Pathological conditions can lead to high glutamate concentrations in the extracellular space, which causes glutamate excitotoxicity due to overstimulation of excitatory synapses, further escalating these life-threatening conditions. This causality makes the ability to modulate the activity of EAATs highly desirable.
EAATs transport glutamate against its gradient by cotransport of three sodium ions, one proton and counter transport of a single potassium ion along their gradients. By exploiting the energy stored in these gradients, EAATs can maintain a glutamate gradient with nanomolar concentration extracellular and millimolar values intracellular, with no need for a primary energy source. Additionally, they feature an anion-selective channel which is chloride conductive under glutamate transport conditions.

Recently, progress has been made in understanding the binding and release of ligands and the associated conformational changes required. This was the result of combining structural data from X-ray crystallography, cryogenic electron microscopy and molecular dynamic simulations. X-ray crystallographic structures of EAAT1 and the close relative neutral amino acid transporter ASCT2 as well as archaebacterial homologue glutamate transporters (Glt) Glt_{Ph} and Glt_{Tk} were made available over the last 17 years. Notably, those obtained using Glt_{Ph} exhibit large conformational diversity, including conformations in the two end states and multiple putative intermediates.

Based on the published structures, an elevator-like movement of the transport domain relative to the trimerization domain was postulated, which allows the transport domain to switch between two distinct conformations, outward-facing (OFC) and inward-facing (IFC). This mechanism is a variant of the alternating access mechanism and requires, at least, vertical translation across the membrane and rotation of the transport domain. During this translational-rotational motion, the bound ligand is moved through the lipid bilayer and accessibility of the binding site is switched. This mechanism has been initially described for the prototypical elevator-like aspartate transporter Glt_{Ph}, but in the following years, numerous transporters were found to operate according to this mechanism. For the published intermediates, their location in the conformational landscape and relevance are still up for debate. In particular, understanding of the formation and physiological role of the anion channel, forming during transport, is lacking.

To investigate the conformational changes required for the physiological OFC to IFC translocation of a fully bound Glt_{Ph} protomer, the "accelerated weight histogram" (AWH) method was combined with Markov state modeling.

The complete transformational change required for the OFC-IFC transition was captured and the elevator-like mechanism was characterized as a multistep process. This includes formation of the anion pore, which is not an obligatory step during translocation. A possible influence of the lipid bilayer on transport dynamics and pore formation was found by comparison of asymmetric trimers. Additionally, a previously uncharted region in the conformational landscape was found, structurally similar to the IFC but featuring a more accessible binding site.

Chapter 2

Introduction

2.1 Glutamate as a neurotransmitter

Glutamate may be best known for its common, and often critically viewed, use as a taste-enhancing substance in the food industry and less for its role as the major excitatory transmitter in the mammalian central nervous system. This presence in the mammalian brain depends on a surprisingly tightly controlled uptake and release cycle. Its concentration, location and dwell time determine whenever a signal is either properly mediated or adjacent cells malfunction due to a process termed excitotoxicity [1, 2]. This neurotoxicity by extended exposure to glutamate might be toxic for neurons and glial cells due to high calcium influx caused by overstimulation of N-methyl-D-aspartate (NMDA) and some α-amino-3-hydroxy-5-methyl-4-isoxazolepropionic acid (AMPA) receptors which potentially triggers apoptosis [1, 2, 3]. To understand how extracellular glutamate concentration is kept below neurotoxic level, in the nanomolar range [4, 5], it is helpful to have a close look at the synaptic cleft. Here, cells with glutamate sensing and binding proteins are next to cells packed with vesicles, which are loaded with glutamate concentrations in the millimolar to molar range [6, 7, 8]. During signal propagation rapid release and, equally rapid, clearance of glutamate can be observed [9, 10]. On one side, the presynaptic terminal, glutamate filled vesicles are docked to the intracellular side of the cell membrane and await activation, upon which they fuse with the cell membrane and release glutamate into the synaptic cleft [10, 11]. These vesicles are loaded by a special type of glutamate transporter, vGLUT. This transporter exploits a proton gradient between the inside of the vesicles and the intracellular space, which is maintained by multiple proton pumps [12, 13]. Docking and fusing with the cell membrane are mediated by large membrane-bound receptors, [14] which are crucial for rapid and controlled glutamate release. The other side,

the postsynaptic terminal, is densely packed with arrays of glutamate receptors that can sense glutamate concentration but lack the ability to remove it. Activation of ionotropic (AMPA, NMDA and kainate) receptors causes them to become permeable for sodium, potassium and sometimes calcium ions, this influx of positively charged ions causes membrane depolarization and contributes to action potential formation [15, 16]. Additionally, glutamate activates metabotropic glutamate receptors, which modify neuronal excitability through intracellular biochemical cascades [17, 18, 19].

Since the mentioned glutamate receptors feature no mechanism for glutamate uptake, an additional family of proteins is needed which removes it promptly due to its neurotoxicity mentioned above and potential crosstalk if it should reach neighboring neurons. This is the role of the **E**xcitatory **A**mino **A**cid **T**ransporters, short EAATs.

2.2 Excitatory amino acid transporters and family

As their name suggests, their primary function is glutamate transport from the extracellular into the intracellular space under physiological conditions [20]. In total, five mammalian EAATs are known today, all of them are secondary active transporters and cotransport three sodium ions plus one proton along with one glutamate molecule into the cell. For the reverse translocation, they exploit a potassium gradient by counter transport of a single potassium ion [21, 22]. A special property of EAATs is that all of them feature an anion channel that requires glutamate binding, but is thermodynamically uncoupled to its transport [23, 24, 25]. Among EAATs family members, their expression pattern and relative conductance as well as specificity towards glutamate varies. In terms of extracellular glutamate mediation EAAT2 is the most important one, it is expressed on astrocytes near the synaptic cleft along with EAAT1 and is responsible for about 90% of the glutamate reuptake in the brain [26, 27]. There is some evidence that EAAT1 may play a role during brain maturation as its expression pattern changes and EAAT2 might not be expressed in astrocytes in early development stages [28, 29].

EAAT3 and EAAT4, on the other hand, are mainly found on neurons. EAAT4 has a high glutamate affinity but low transport rates, [30] and EAAT3 can transport the neutral amino acid cysteine [31]. EAAT5 is expressed in retina cells and features a high chloride conductance and is believed to mediate light responses in depolarizing bipolar cells through its anion channel activity [32]. Impaired function of these proteins is associated with neurological diseases like Alzheimer's [33], Parkinson's [34, 35], schizophrenia [36], depression [37, 38, 39] and multiple sclerosis [40, 41, 42, 43] probably due to excitotoxicity or in the case of EAAT3 protection from oxidative stress

by conversion of cysteine to glutathione (GSH) [44], while upregulation was found to improve cognitive ability in an Alzheimer's mouse model [45, 46]. Close relatives of the EAATs are the alanine, serine, cysteine transporters (ASCT1 and ASCT2), also heavily expressed in the brain but not limited to it. Other noteworthy relatives are archaebacterial glutamate transporter from *Pyrococcus horikoshii* [47] ($\mathrm{Glt_{Ph}}$) and *Thermococcus kodakarensis* [48] ($\mathrm{Glt_{Tk}}$). While they feature a sequence identity of only 36% with EAATs [49], their structural and functional similarity is astonishingly high.

2.3 Mechanism and structure

As mentioned, all EAATs are secondary active transporters, the energy needed to transport glutamate against its gradient does not come from a chemical reaction like conversion of ATP to ADP but a chemical gradient, in this case, sodium, potassium and protons [50, 51, 52]. In the present case, the symport of three sodium ions and one proton along their gradient supplies the energy needed to transport one glutamate molecule against its gradient. This is achieved by inducing conformational changes of the protein into the inward-facing conformation (IFC) which exposes the binding site to the cytosol. Unbinding of glutamate and the symported molecules completes the first half of the transport cycle. To reverse the conformational change and reset the protein in its outward-facing conformation (OFC) EAATs harvest the necessary energy by transporting a single potassium ion along its gradient from the cytosol into the extracellular space. The cotransported ions do not only supply the needed energy to induce the conformational change, but also influence the conformational equilibrium of a hairpin structure termed hairpin 2 (HP2). HP2 acts as a gate that shields the binding site from solvent and regulates substrate binding [53, 54, 55]. This hairpin 2 can change between two metastable conformations, open and closed. In its open conformation, it allows molecules like glutamate to enter the binding site and simultaneously blocks movement of the transport domain, thus preventing the switch between the outward and inward-facing states [56, 53]. In the outward-facing conformation, the binding of a sodium ion to two of the three sodium binding sites (NA1 and NA3) leads to stabilization of the open hairpin conformation and allows glutamate to access the binding site [57, 58]. The binding of glutamate leads to another shift in the conformational preferences of HP2, and it may now assume a closed or closed-like conformation. The third and final, sodium may now bind to the NA2 binding site which is formed partly by residues in HP2 and TM7 and is assumed to stabilize the closed hairpin conformation [59, 57, 60]. Analogously, it was shown that, in the

inward-facing conformation, the binding of potassium shifts the conformational equilibrium of HP2 towards the closed state and thus enables the protomer to return into the outward-facing conformation [55]. All EAATs are trimers with two major domains per protomer, one termed transport domain (TD) and one scaffold or trimerization domain (SD) [61, 62]. The transport domain features the binding sites for sodium, potassium and glutamate and is undergoing a huge conformational change which moves the binding site approximately 20 Å up- or downwards, through the membrane [63].

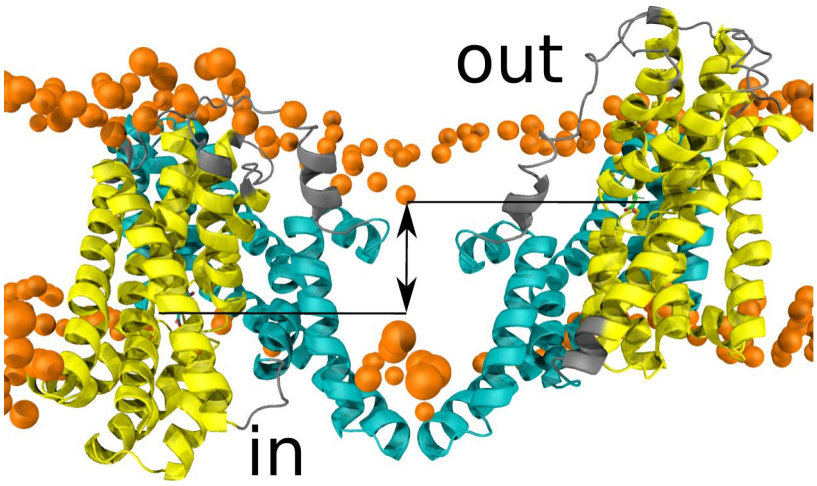

Figure 2.1: Outward facing (PDB code *2NWX* [57], right) and inward facing (PDB code *3KBC* [63], left) conformations of the aspartate/glutamate transporter Glt_{Ph}. The black arrow indicates the 20 Å movement of the binding site across the membrane normal. Transport domain in yellow, trimerisation domain in cyan, lipid headgroups in orange.

While the transport domain forms the majority of contacts with the lipid bilayer, it has no direct contact with other protomers. Multiple publications suggest that protomers show no cooperativity and any conformational change is solely due to binding and unbinding of sodium, glutamate, potassium and pure chance [64, 65]. The trimerization domain on the other hand is in close contact with its two protomeric copies. It is assumed that it anchors the protomer in the membrane through interactions with the membrane and the trimerization interface and acts as a "counterweight" for the transport domain [63]. Since only insignificant conformational changes of the trimerization domain were observed in crystal structures, it was assumed that its position relative to the membrane does not change either. Recent coarse-grained molecular dynamics simulations challenged that theory [66] and cryo-EM structures published shortly [56] afterwards seem to confirm an upward, respectively, downward movement of the trimerization domain relative to the membrane, depending on the location of the transport domain. The motion performed by the transport domain was described

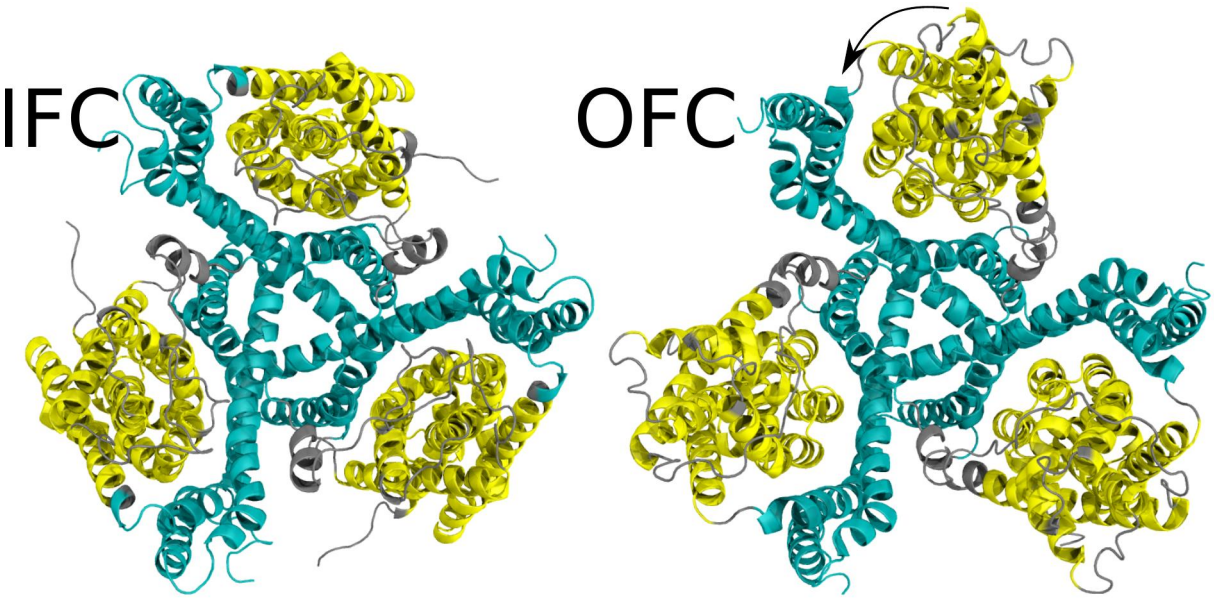

Figure 2.2: Outward facing (PDB code *2NWX* [57], right) and inward facing (PDB code *3KBC* [63], left) conformations of the aspartate/glutamate transporter Glt_{Ph}. The black arrow indicates the 37° rotation of the transport domain. Transport domain in yellow, trimerisation domain in cyan, lipid headgroups in orange.

as a rigid body motion or elevator translocation since crystal structures suggested that both domains undergo no significant internal reorganization, and the transport domain slides along the SD up and downwards like an elevator [57, 63]. As mentioned above the archaebacterial homologs Glt_{Ph} and Glt_{Tk} are highly similar to EAATs [67], they feature the same segmentation into two domains [49] and the same cotransport of sodium [68], although they do not feature transport of the proton [69]. Also, they do not rely on the transport of potassium for the inward to outward translocation [69, 68]. But they do feature chloride conductance, which is glutamate-dependent but thermodynamically uncoupled [70], just like described above for EAATs. A thermostabilized variant of EAAT1 was successfully crystallized in the outward-facing conformation, and ASCT2 was crystallized in an inward-facing conformation. For Glt_{Ph} 36 crystal structures were published, in ligand-bound and unbound states and inward as well as outward-facing conformations. Additionally, multiple intermediate conformations [71, 72] were published, including potentially open channel conformations [73]. This availability of structural data, combined with the high structural and functional similarity, is the reason Glt_{Ph} was chosen as a model for the mammalian glutamate transporters and all further research was conducted on it.

Chapter 3

Methods

3.1 Molecular dynamics simulations

All simulations were run using the GROMACS software package [74, 75] and used the CHARMM36m force field [76] in combination with the included TIP3 model for water molecules. Each system was prepared by the following protocol. Initial protein structures were obtained from the protein data bank (PDB) and prepared using the MODELLER software package 9.11 [77] to ensure a symmetric trimer. All mutations introduced to aid crystallization were reversed, and missing atoms were added to ensure that all conformations span the same range of residues. The fixed trimer was aligned manually, guided by the corresponding model from the OPM database [78], to a preequilibrated 1-palmitoyl-2-oleoyl-sn-glycero-3-phosphocholine (POPC) lipid bilayer in a box of water with approximately 0.5M NaCl and embedded into this bilayer by utilizing the membed function implemented in GROMACS [79] to obtain a combined system with a minimum of perturbation. The final box was 145 Å in X and Y plane and a height of 110 Å, this was enough to have a distance of at least 30 Å between each protomer and any protomeric mirror image over periodic boundary conditions. Previous publications, experimentally, established that Glt_{Ph} is active in a POPC bilayer [80] and has been extensively used in *in silico* studies of Glt_{Ph} and EAATs [81, 82, 83]. This assembled system was then subject to three rounds of equilibration. In the first round, all protein atoms were restrained by harmonic potentials in XYZ direction, phosphor atoms of the lipid head groups were restrained in Z-axis only. Position restrains on the lipid atoms ensured that the bilayer was not perturbated irreversible by close contacts between protein and lipids and during a 5 ns simulation lipids and solvent molecules were able to resolve artifacts from embedding. In the second round, restrains on lipid atoms were lifted while keeping restrains on all protein atoms, al-

lowing the system to adapt to the frozen protein structure while keeping the protein reasonably close to the initial conformation. These simulations were run until the system reached a stable density, for most simulations this was reached after about 500ns. During equilibration runs the pressure was kept at 1 bar using the Berendsen barostat [84], during production runs the alternative Parrinello-Rahman barostat [85] was used to obtain canonical sampling. The temperature in all simulations was kept at 310.15K by the Bussi-Donadio-Parrinello thermostat [85] with velocity rescale [86]. The LINCS algorithm [87] was employed to constrain hydrogen bonds, water molecules were constrained using the SETTLE algorithm [88]. All protein residues were modelled in their default protonation state. Structural representations of proteins were generated with PyMOL [89].

3.2 Enhanced sampling

Since no spontaneous translocations were observed in unbiased MDs started from the published crystal structures *2NWX* [57] and *3KBC* [63] an enhanced sampling method called "accelerated weight histogram method" (AWH) [90, 91] was employed to enforce transitions of one protomer, out of three, between the outward-facing and inward-facing states. The enhanced sampling method "Accelerated weight histogram method" is an iterative scheme similar to other enhanced sampling techniques like metadynamics [92] or umbrella sampling [93]. To start the algorithm an initial estimate of the free energy f_k must be chosen, this can be a simple flat distribution. Afterwards, N_x updates to the configuration x are performed for a fixed parameter m. A new set of parameters m' is selected by a Gibbs sampler and accepted based on the conditional probability of m' given the current configuration x.

$$w_{m'm}(x) = P(m'|x) = \frac{e^{-E_{m'}(x)+f_{m'}}}{\sum_t w_{km_t}(x_t)} \tag{3.1}$$

The transition probabilities of $x \to m'$ computed as in Eq. 3.1 are used to update a weight histogram W_k (Eq. 3.2) and reweigh sampled observables as in Eq. 3.3.

$$W_k \leftarrow W_k + w_{km}(x), \quad \forall k \tag{3.2}$$

$$\langle A \rangle_k = \frac{\sum_t A(x_t,k) w_{km_t}(x_t)}{\sum_t w_{km_t}(x_t)} \tag{3.3}$$

After N_I updates to the weight histogram have been made the free energy estimate for each k is updated, the adjusted free energy estimate is then used to update the weight histogram (Eq. 3.5).

$$\Delta f_k = -ln(\frac{W_k M}{N}) \tag{3.4}$$

$$W_k \to W_k e^{\Delta f_k} = \frac{N}{M} \tag{3.5}$$

With N being the total number of samples collected and M being the total number of parameters m visited so far. If f reached the desired accuracy, sampling is stopped, otherwise, a new m' is selected and more samples are collected to update W and finally f. Multiple simulations were started from equilibrated snapshots of *2NWX* [57] (as a model for the outward-facing state) and *3KBC* [63] (as a model for the inward-facing state) with different settings and biased them along two reaction coordinates. For an overview of known structures and corresponding annotations, see Table 4.2. The first reaction coordinate is the horizontal distance between the center of mass of the

transport domain and the center of mass of the trimerization domain, along the X and Y-axis. This coordinate was introduced to include a possible "unlocking" [71] of the transport domain in our description of the transport cycle. The second reaction coordinate is the vertical distance along the Z-axis between the center of mass of the transport and trimerization domain, capturing the approximately 2 nm shift of the transport domain. Due to the system's non equilibrium character, pressure was controlled by the Berendsen barostat [84]. Simulations were started with different energy barrier cut-offs ($300\frac{kJ}{mol}$ and $1000\frac{kJ}{mol}$) and different diffusion speeds ($10^{-4}\frac{nm^2}{ps}$ and $10^{-3}\frac{nm^2}{ps}$), all simulations are listed in Table 4.1. One favorable property of AWH is that a single simulation covers the reactions coordinates multiple times, potentially exploring multiple pathways in a single simulation.

3.2.1 Principal Component Analysis

To obtain a single value that represents the current state of a protomer, principal component analysis was used. It consists of the construction of a covariance matrix M with the shape $3N \times 3N$ and is constructed with the XYZ coordinates of each atom of interest. After diagonalizing M the eigenvectors and corresponding eigenvalues can be extracted, after reordering according to the eigenvalues the first eigenvector represents the biggest correlated linear motion in the investigated atom group [94, 95]. The first eigenvector was visually confirmed to represent a motion reassembling a plausible translocation, eigenvectors with lower eigenvalues represented smaller fluctuations that were of no interest.

3.3 Markov state models

Markov state models are based on transition probabilities between states. It is based on the assumption that the dynamics of a system, when viewed from the right "distance" are "memoryless". This distance is called lag time (τ) and describes the time between two frames which needs to pass for the next step to only depend on the current state and not any previous one. A system that fulfills this property is called Markovian. One advantage is that Markov state models (MSMs) can be built from a virtually unlimited amount of independent simulations, which suits today's hardware capabilities when using compute enabled graphic processing units (GPUs) available at most high-performance computing facilities. Another advantage is that a valid MSM describes the system dynamics well beyond the longest timescale of the source simulations. Just like other enhanced sampling methods Markov state models need some sort of reaction coordinate that describes the process of interest. In the case of MSMs this reaction coordinate can be derived from the molecular dynamics data and can be redefined easily during modeling.

3.3.1 Featurization

We computed distances between $C\alpha - C\alpha$ pairs of the transport and trimerization domain using NumPy [96] and MDAnalysis [97, 98]. To reduce redundant calculations, we excluded highly flexible loop regions and computed only every fifth $C\alpha - C\alpha$ pair, resulting in 770 distances for each frame.

3.3.2 Dimensionality reduction and clustering

As a first approximation, we reused the reaction coordinates of the AWH systems with no need for further dimensionality reduction. After completion of the first round of simulations, we used time-lagged independent component analysis (TICA) [99, 100] as implemented in PyEMMA [101] to reduce the 770 $C\alpha - C\alpha$ pairs described previously down to two dimensions. The number of dimensions to reduce to was determined visually with the help of an implied timescales plot (ITS) and identification of a gap between the bulk of components and significantly slower ones. The TICA lag time was selected using an ITS plot, see Figure 4.13, as well as the shape of the landscape along the first two components, interpreting an insignificant change of the landscape as an indication of a small gain in encoded information. The number of cluster centers was chosen based on the VAMP2 score [102] of Markov state models build with a different number of cluster centers, see Figure 4.14. While the molecular dynamics simulations

provided one frame every 40 ps we decided to use only every fifth, resulting in a time step of 200ps. We assumed this to be justified as frames from molecular dynamics are highly correlated on short timescales, comparing models build with a time step of 40 ps and 200 ps confirmed that.

3.3.3 Markov state model estimation

Markov state models were built using PyEMMA [101] by utilizing the discretized trajectories described in the previous section. All models used in this work were built with a lag time of 50 ns which was chosen based on their implied timescales and data availability and verified by computing a Chapman-Kolmogorov test (CK test) [103] for each model.

3.3.4 Adaptive sampling

Given a set of simulations K a set of transition matrices T can be sampled from which a standard deviation σ can be derived [104]. To evaluate how adding m new simulations would change T and σ one can scale σ by $\frac{K}{K+m}$, yielding $\bar{\sigma}$. After subtracting the scaled $\bar{\sigma}$ from σ, the sum $\sum_i$ of each row i represents the expected change of uncertainty after adding m new simulations starting in state i. To achieve better convergence m simulations were not started exclusively in the state with the highest $\sum_i$ but one for each top m $\sum_i$. Also using σ^2 instead of σ helps to increase the gap between states with small changes.

3.3.5 Discretization

VAMPNets [105] were recently introduced as an end-to-end alternative to the classical featurization →dimension reduction →discretization →coarse-graining workflow of building Markov state models. They are based on Koopman theory [106, 107], which states that a function exists which transforms a set of non-linear evolving features into a set of features that do evolve linearly. In this case, a transformation x_0 of data X at time t multiplied by a matrix $\mathbf{K}$ should be approximated by a transformation x_1 of data X at time $t+\tau$ with tau > 0 (Eq. 3.6).

$$x_1(X_{t+\tau}) \approx \mathbf{K}^\top x_o(X_t) \tag{3.6}$$

The matrix $\mathbf{K}$ can be derived from the covariance matrices C_{00} and C_{01} [108, 109, 110].

$$C_{00} = x_0(X_t)x_0(X_t)^\top \tag{3.7}$$

$$C_{01} = x_0(X_t)x_1(X_{t+\tau})^\top \tag{3.8}$$

$$C_{11} = x_1(X_{t+\tau})x_1(X_{t+\tau})^\top \tag{3.9}$$

VAMPnets train the missing functions x_0 and x_1 using unsupervised training of a deep neural network with two independent lobes. They are trained on pairs of features (X) at time t and $t + \tau$ derived from continuous MD trajectories and are optimized to maximize the VAMP2-score as given in Eq. 3.10.

$$\hat{R}_2[x_0, x_1] = \left\| \mathbf{C}_{00}^{-\frac{1}{2}} \mathbf{C}_{01} \mathbf{C}_{11}^{-\frac{1}{2}} \right\|_F^2 \tag{3.10}$$

We trained VAMPNets for all possible combinations of lag times in the range from 30 ns to 60 ns in 5 ns increments and four to 16 states with the implementation in the DeepTime library [111]. The models were trained using 70% of the trajectories, the remaining 30% were exclusively used to calculate the validation score. Each model was constructed with an input layer of 770, corresponding to the number of $C\alpha - C\alpha$ distance pairs, followed by three fully connected layers with 100 neurons. The last two layers were another fully connected layer with 30 neurons and a final output layer with N neurons, with N corresponding to the number of states. The ELU activation function was used for all layers except the output layer, here a linear activation was used and combined with a softmax function to obtain values summing to 1. Models were trained for a maximum of 300 epochs and stopped early if the validation score improved by less than 0.05% in five consecutive epochs. To select the best model, a score for each trained model was computed using the slope of the slowest implied timescale and the total error of the Chapman-Kolmogorov test from an MSM build using the VAMPnet assignments, see Figure 4.16.

3.3.6 Detection of water permeation

The simulations box was divided into three compartments, upper, lower and transition. The upper compartment was defined as the space above 10 Å of the lipid bilayers center of mass, the lower compartment as the space below 10 Å of the lipid bilayers center of mass. To define the transition zone, a convex hull for Cα of the translocating protomer was constructed. Using these compartments, each water molecule was assigned to one of them, for every frame in a trajectory. Molecules in the upper compartment were assigned a 1, those in the transition zone a 2 and those in the lower compartment a 3. The resulting matrix, shape NxM with N the number of frames in the trajectory and M the number of water molecules, could now be searched for the sequences 1-(2)-3 or 3-(2)-1, with no limit on the repetitions of (2). Sequence 1-(2)-3 corresponding to a

water molecule moving through the protein from the upper to the lower compartment, and sequence 3-(2)-1 for the reverse movement.

3.3.7 Determine water permeation probability

To assign a water permeation probability to each metastable state, 5 ns windows were constructed from the continuous MD data. The probability of observing a water permeation per time unit given a single window is the number of permeations N divided by the length of the window t.

$$p^w = \frac{N}{t} \tag{3.11}$$

To convert from time to the states used in the MSM Eq. 3.11 can be written as Eq. 3.12, with S being the number of states, i being one of those states and fi^S the frequency of each state in the window.

$$p^w = \sum_i f_i^S p_i \tag{3.12}$$

Adopting Eq. 3.12 for multiple windows, a p_i can be found that minimizes Eq. 3.13 and gives the best estimate of observing water permeation in a frame assigned to state i.

$$\sum_{w=1}^{W} (p^w - \sum_i f_i^S p_i)^2 \tag{3.13}$$

Chapter 4

Results

4.1 Enhanced sampling of transition pathways

In total, 34 AWH simulations were started and analyzed. In the outward-facing conformation, 17 simulations were started and in the inward-facing conformation, additional 17 simulations were started. Two sample simulations are shown in Figure 4.1. In total 129 transition events were obtained from these 34 simulations, 64 OFC to IFC transitions and 65 IFC to OFC from a total of 7.989 μs of simulation time. An overview of all simulations with the parameters used and the number of transition events observed can be found in Table 4.1. To distinguish unbiased simulations started from 2NWX (OFC) or 3KBC (IFC) and all three protomers in the same state, from simulations subjected to enhanced sampling with one monomer translocating these, will be referred to as OOX and IIX. These terms shall illustrate that two protomers are in the outward (**OO**X) or inward (**II**X) state, while the third one (OO**X** or II**X**) is translocating and in an intermediate conformation most of the time.

Index	Initial conformation	Length [ns]	Transition events	Maximum bias $\frac{kJ}{mol}$	Diffusion rate $\frac{nm^2}{ps}$
1	3KBC	115	2	1000	10^{-4}
2	3KBC	113	1	1000	10^{-4}
3	3KBC	114	3	1000	10^{-4}
4	3KBC	116	1	1000	10^{-4}
5	3KBC	114	1	1000	10^{-4}
6	3KBC	115	2	1000	10^{-4}
7	3KBC	115	2	1000	10^{-4}
8	3KBC	113	2	1000	10^{-4}
9	3KBC	114	3	1000	10^{-4}
10	3KBC	113	3	1000	10^{-4}
11	3KBC	331	5	1000	10^{-3}
12	3KBC	726	4	1000	10^{-4}
13	3KBC	253	3	1000	10^{-4}
14	3KBC	565	7	1000	10^{-3}
15	3KBC	696	5	1000	10^{-4}
16	3KBC	146	0	300	10^{-3}
17	3KBC	123	0	300	10^{-4}
18	2NWX	115	3	1000	10^{-4}
19	2NWX	112	3	1000	10^{-4}
20	2NWX	116	2	1000	10^{-4}
21	2NWX	115	2	1000	10^{-4}
22	2NWX	115	1	1000	10^{-4}
23	2NWX	115	1	1000	10^{-4}
24	2NWX	114	1	1000	10^{-4}
25	2NWX	113	3	1000	10^{-4}
26	2NWX	115	2	1000	10^{-4}
27	2NWX	115	2	1000	10^{-4}
28	2NWX	448	4	1000	10^{-3}
29	2NWX	790	7	1000	10^{-4}
30	2NWX	569	5	1000	10^{-3}
31	2NWX	720	5	1000	10^{-4}
32	2NWX	86	4	300	10^{-3}
33	2NWX	91	3	300	10^{-3}
34	2NWX	144	3	300	10^{-4}

Table 4.1: Table of enhanced sampling simulations using the accelerated weight histogram method, showing the initial structure (3KBC for IFC and 2NWX for OFC), simulation length, number of complete transition events observed, upper limit for added bias and the initial guess of the diffusion rate of the process of interest.

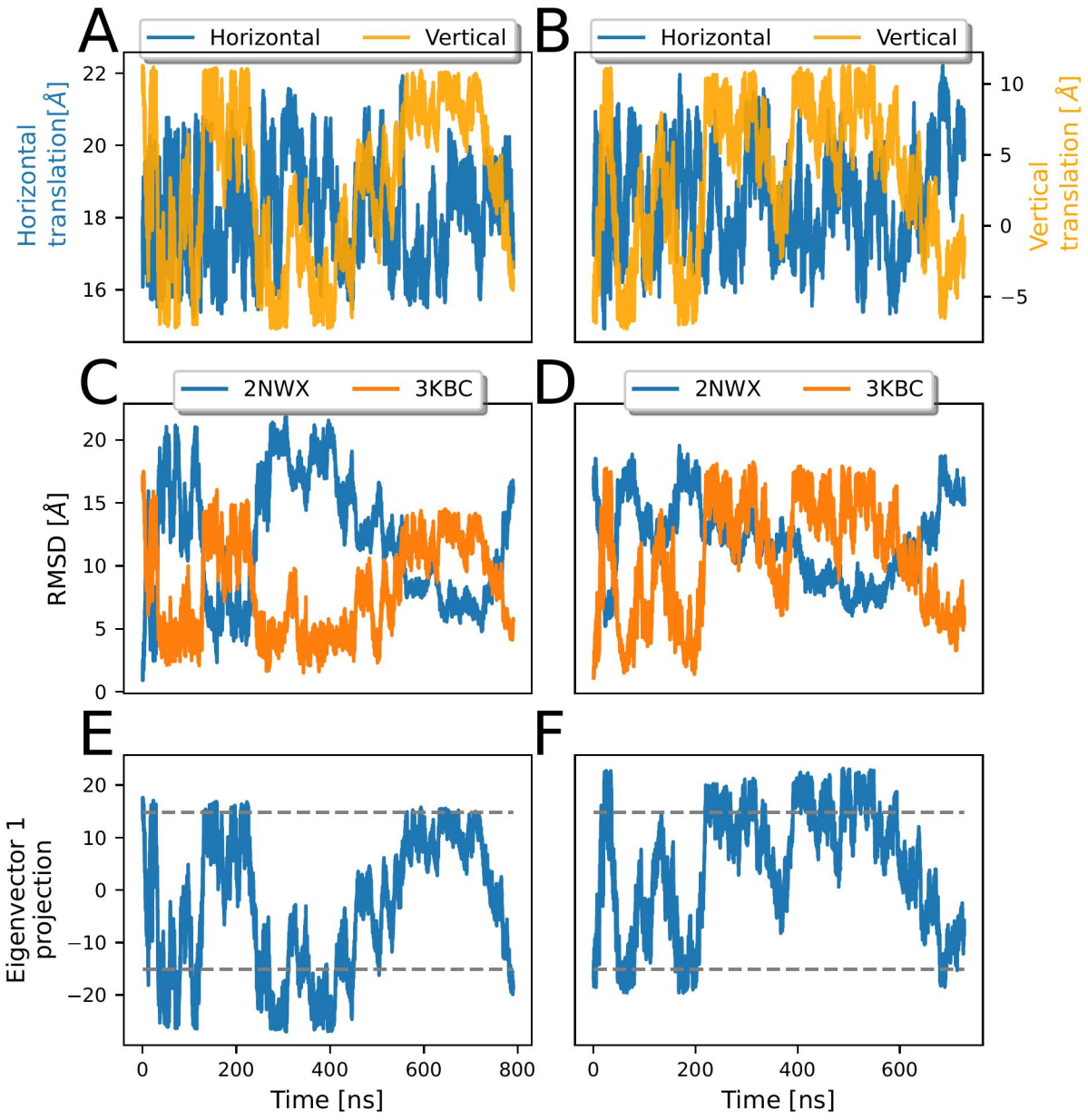

Figure 4.1: Representative AWH simulations started from outward (left, simulation 31, started from 2NWX) and inward facing conformations (right, simulation 12, started from 3KBC). **A** and **B**: Course of reaction coordinate one (**Horizontal** distance between the two domains) and reaction coordinate 2 (**Vertical** offset of the transport domain). **C** and **D**: RMSD of the biased protomer towards crystal structures 2NWX and 3KBC. **E** and **F**: Projection of the biased protomers coordinates along eigenvector one with outward and inward cutoffs as grey dotted lines.

4.1.1 Structural diversity along the reaction coordinate

It was quickly noticed that convergence of the two-dimensional energy profile from enhanced sampling was rather slow and even after 800 ns no signs of a converging energy profile were observable. It was assumed that the chosen reaction coordinates, while separating the two end states properly, failed to differentiate between structurally distinct conformations along the transition pathway. To verify this assumption, we binned conformations into a 50 by 50 grid along the two reaction coordinates and computed the average RMSD in each bin. Figure 4.2 depicts the average RMSD of structures inside the same bin, the dark upper patch, encircled by a blue ellipsoid, represents the outward-facing state and the lower one, encircled by an orange ellipsoid, represents the inward-facing state. The RMSD is low (about 1 Å) in areas, which are also explored by unbiased simulations started from 2NWX or 3KBC. It increases as the system explores conformations in between the outward and inward-facing state, here the RMSD ranges from 2 Å to 5 Å and significantly increases with RC1.

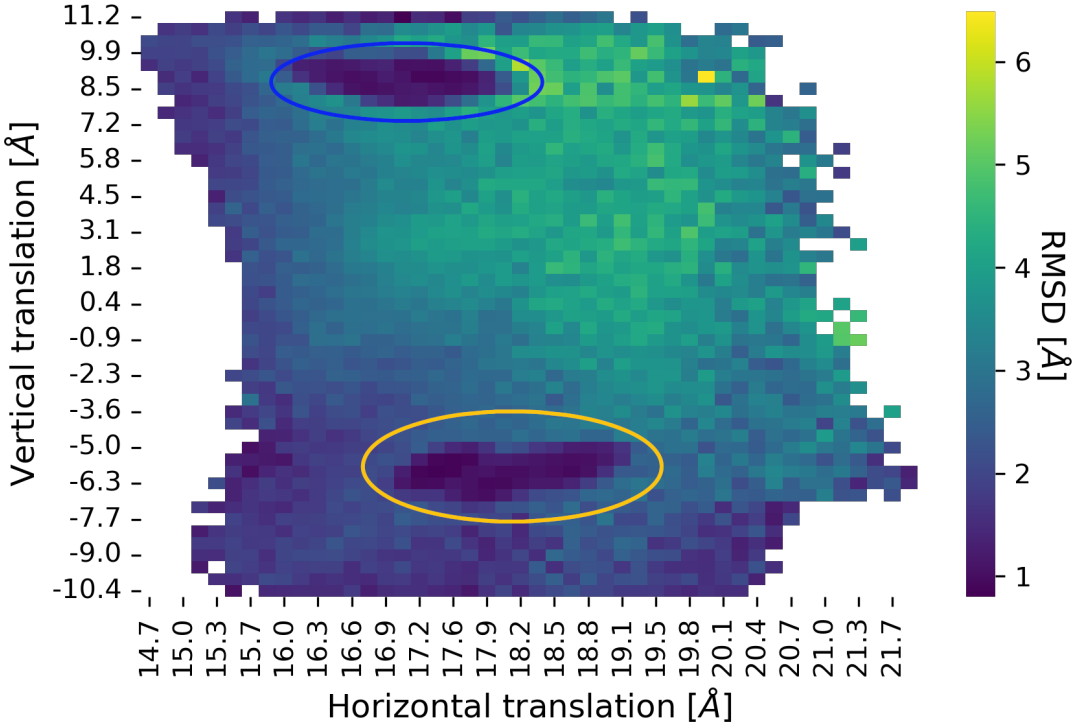

Figure 4.2: Averaged RMSD between structures with the same reaction coordinates in a histogram, with 50 bins along the X- and Y-axis. Reaction coordinates are the horizontal distance between the two domains and the vertical translocation of the transport domain, as defined for enhanced sampling. Ellipsoids mark the area also explored in unbiased simulations started from 2NWX (blue) and 3KBC (orange). Data shown is from OOX and IIX simulations which were subjected to enhanced sampling.

4.1.2 Stability of the biased protomer

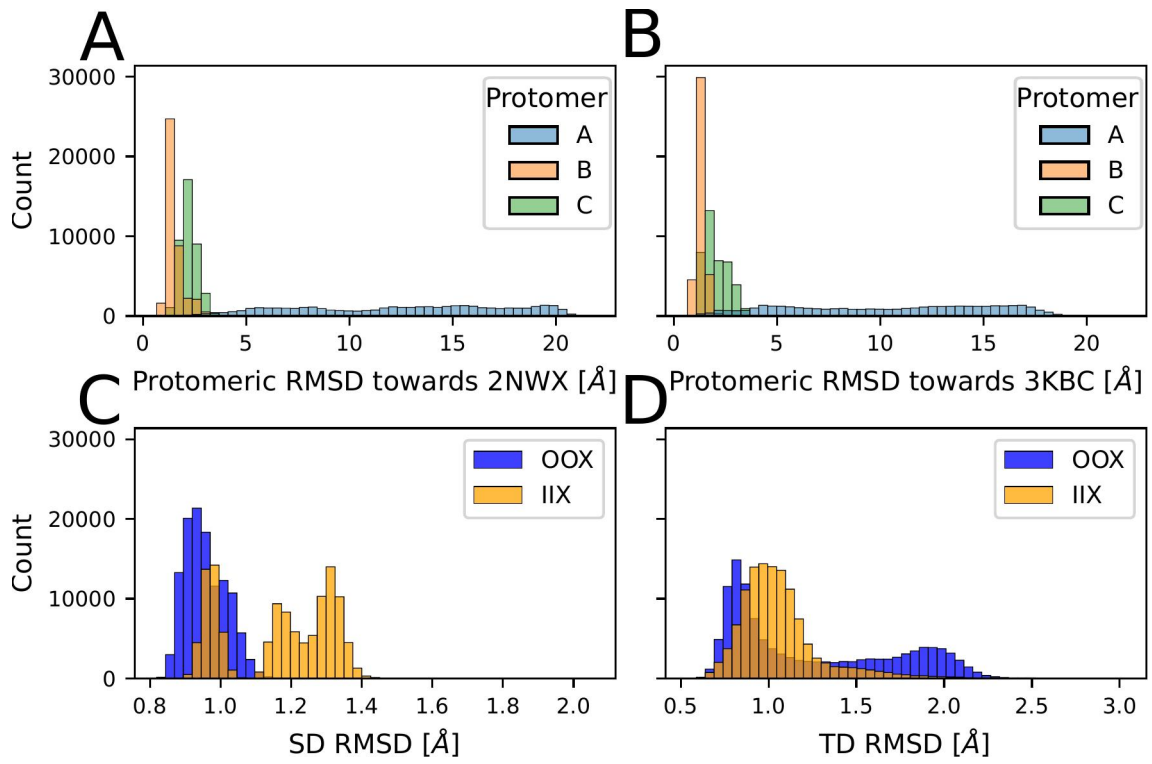

Figure 4.3: **A and B**: Stability of whole protomers in OOX (**A**) and IIX (**B**) with protomer A being subjected to biasing. The RMSD shown is computed towards the corresponding starting structure, as indicated on the X-axis. **C and D**: Internal stability of the trimerization (SD, **C**) and transport (TD, **D**) domain during enhanced sampling simulations. The RMSD shown is computed towards the corresponding initial conformation, 2NWX for OOX and 3KBC for IIX.

Since AWH introduces substantial perturbations into the system, there were concerns that the two unbiased protomers might undergo unwanted deformation. But fast transitions of the biased protomer had no destabilizing effect on the two unbiased ones, as seen in Figure 4.3 A and B. The trimerization domain of the biased protomer featured high stability in all simulations (Figure 4.3C), slightly higher RMSD values observed in IIX simulations were also observed in unbiased simulations started from the crystal structure. The RMSD of the TD of protomer A, seen in Figure 4.3D seems to be correlated with the opening of hairpin 2, as seen in Figure 4.4, which seems to open at the start or towards the end of the range of vertical translocation, as seen in Figure 4.5. These results indicate that the bias from enhanced sampling and the resulting, fast, translocations had no destabilizing effect on the neighboring protomers and introduced no artificial conformational changes in the biased protomer.

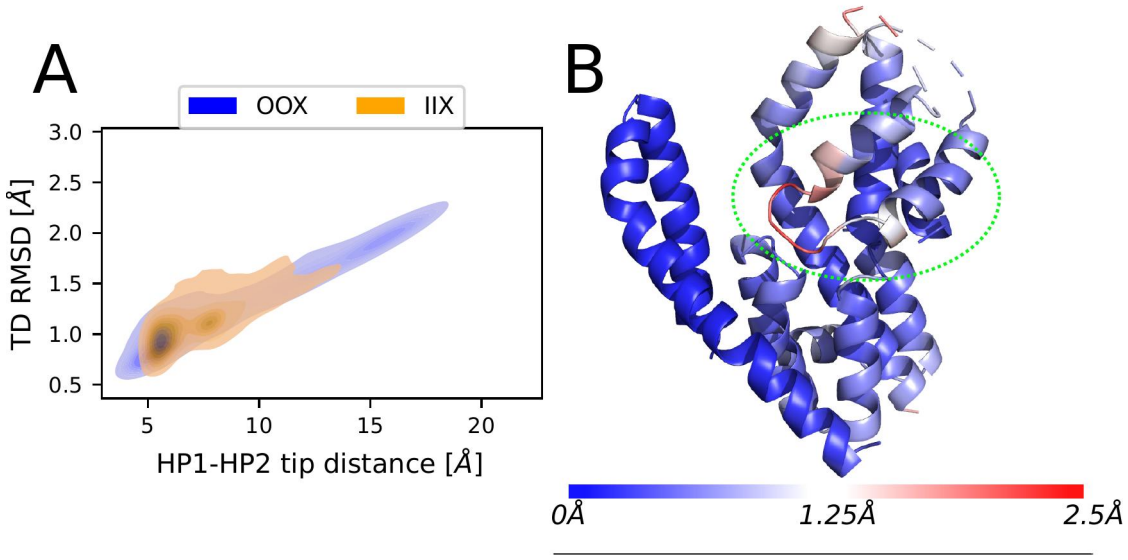

Figure 4.4: **A**: Internal RMSD of the transport domain depending on the distance between the tips of hairpin 1 and hairpin 2. **B**: Structure of a protomer in the outward conformation, colored according to structural fluctuations (RMSF) during an enhanced sampling simulation. Blue regions are stable, red areas feature a higher degree of structural fluctuations. The green circle indicates the location of Hairpin 2.

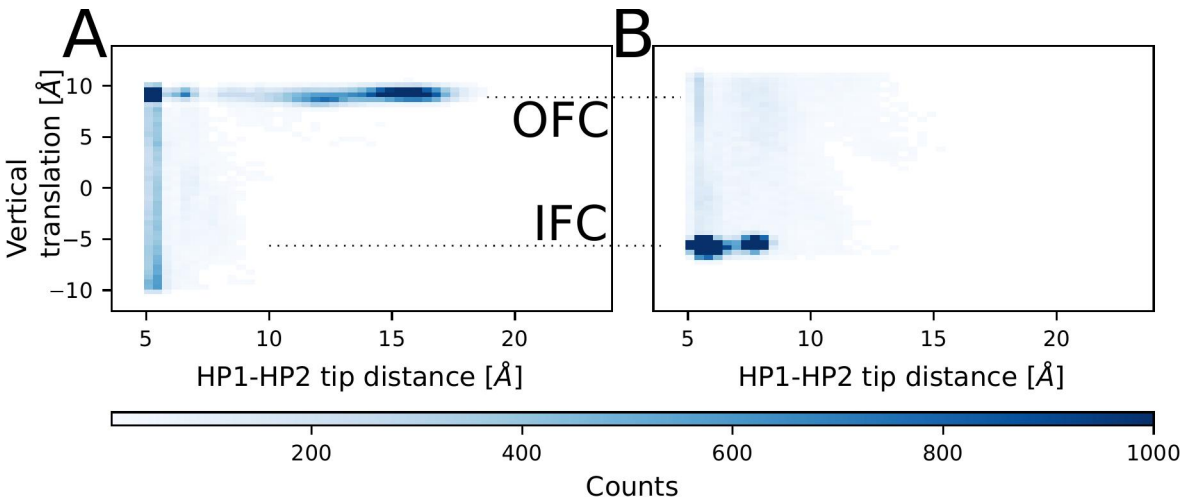

Figure 4.5: Distance between tips of hairpin 1 and hairpin 2 along the vertical translocation during enhanced sampling in OOX (**A**) and IIX (**B**) systems. Dotted lines mark values observed for unbiased protomers in the outward or inward-facing conformation.

4.1.3 Extraction of transition events

Splitting AWH simulations, into transition events was done to obtain a set of initial conformations which coarsely cover the whole conformational space, for this the projection along the first eigenvector was used, see section 3.2.1 and Amadei et al. [94, 95]. This allowed the definition of one value for the OFC, derived from an unbiased 2NWX simulation, and one for the IFC, derived from a 3KBC simulation. This was found to be a more reliable way to detect transitions than solely using the RMSD towards the two crystal structures, 2NWX and 3KBC. The start and endpoints of an event were defined as the frame when the simulation's projection crossed one of the two cut-offs. In Figure 4.7A, a representative example of a simulation separated into transition events is shown.

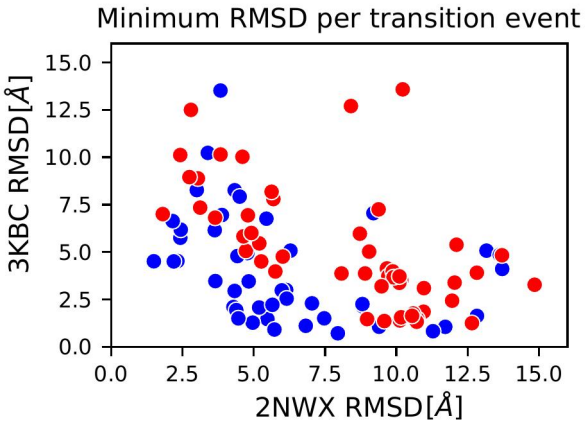

Figure 4.6: Minimal RMSD towards 2NWX and 3KBC crystal structures observed in each transition event. Red dots represent an event from a simulation with two protomers in the inward facing state. Blue dots represent an event from a simulation with two protomers in the outward facing state.

Furthermore, splitting the simulations into transition events allowed us to judge how close the protomer approached its target structure and how successful it returned into the initial conformations. Figure 4.6 shows that there are only two events that approached both (2NWX and 3KBC) conformations with an RMSD below 4 Å but in multiple simulations, the target structure is closely approached or the protomer returned into a conformation very close to its initial one. These transition events were used to compute all-to-all RMSD maps, with the RMSD of every frame from one event to each frame of a second event. For each event pair, one map was computed, and the maps were oriented to ensure that the lower left corner always represented the outward-facing state in both events and the upper right corner the inward-facing state. A python implantation of the A* algorithm [112] was used to search for the least-costly

path from the lower left (OFC) to the upper right (IFC) corner, here cost is equal to the RMSD and thus the path represents the minimum RMSD path. Similarity between two transition events was defined as the maximum RMSD along the minimum RMSD path from the lower left corner to the upper right corner. Afterwards, all transition events were clustered based on the maximum RMSD similarity metric and all events, which were not assigned to a cluster, were excluded from further analysis. Clustering was done using the python implementation of "Ordering Points To Identify the Clustering Structure" (OPTICS) with its default parameters in scikit-learn [113, 114, 115]. This filtering was done to reduce the possibility of artificial conformations to taint further analysis, due to high forces in AWH simulations, as it is assumed that if an event was observed multiple times it is more likely to represent a valid pathway. The complete workflow is depicted in Figure 4.7.

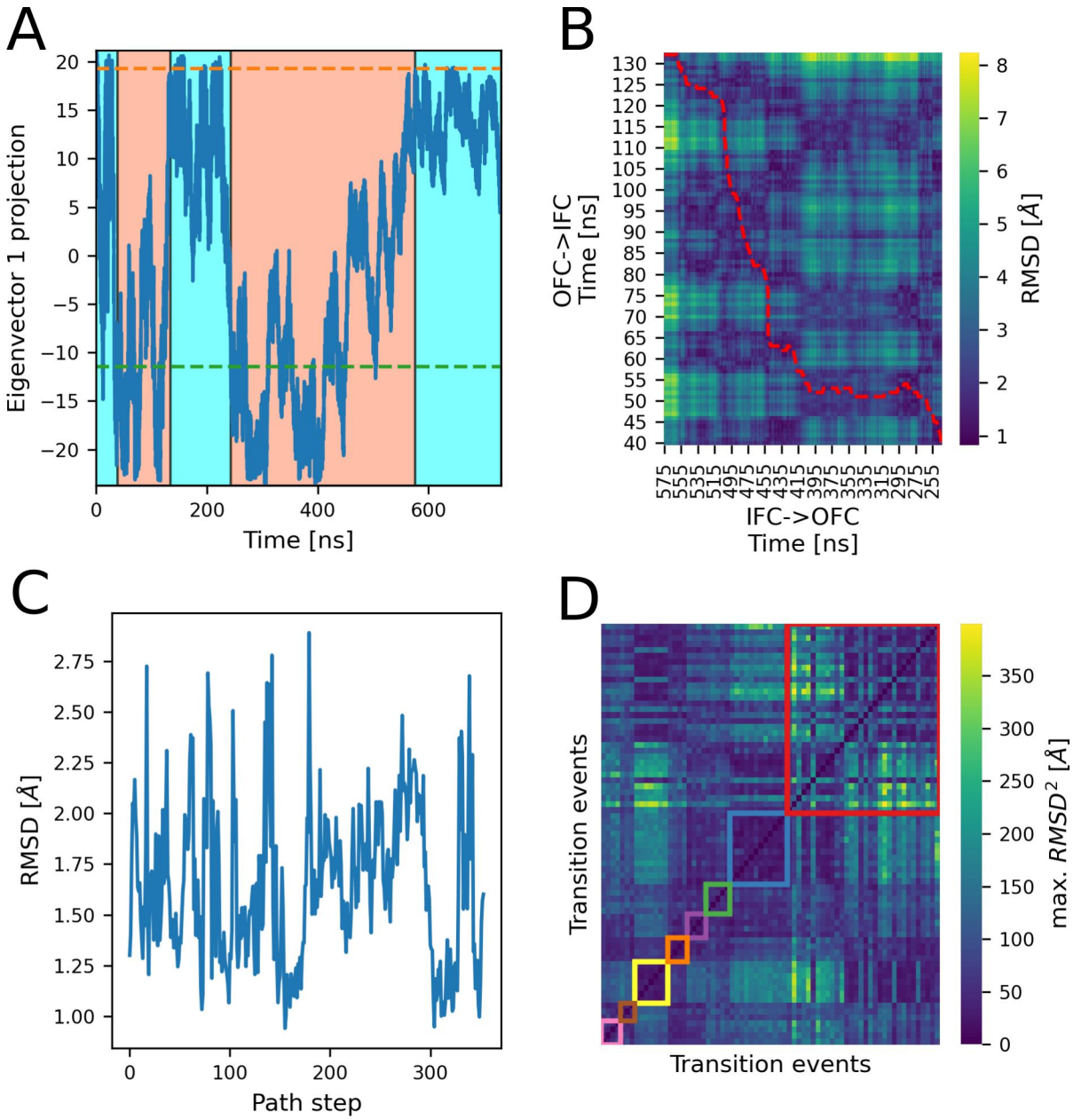

Figure 4.7: Workflow for the generation of initial structures: **A**: Enhanced sampling simulations are split into single transition events. **B**: Pairwise RMSD maps were computed for each pair of transition events, the path along the minimal RMSD (shown in red) was used to score similarity between two events. **C**: RMSD along the minimal RMSD path (shown in red in B). **D**: Transition events (on X and Y axis) were clustered using the OPTICS clustering algorithm and the squared maximum RMSD along the minimal RMSD path between both events as features. Clusters found are marked by colored squares. In total seven clusters were found, the big red square in the upper right contains all transition events which were not assigned to one of the seven clusters.

4.2 Markov state modelling

4.2.1 Unbiased simulations for Markov state modeling

From the transition events extracted from enhanced sampling simulations, 100 snapshots were selected to seed unbiased simulations. These 100 snapshots were selected by binning all frames, after filtering, based on their reaction coordinates into a 10 by 10 histogram and randomly drawing one frame from each bin. From these initial simulations, new simulations were started, according to an adaptive sampling scheme described in [104] and Section 3.3.4, to obtain better coverage of the conformational landscape and the underlying processes. The position of the initial simulations in the reaction coordinate and TICA space can be seen in Figure 4.8 as red dots, positions of simulations started by adaptive sampling are shown as gray dots. In total, 1144 simulations with an aggregated total time of 594 µs were used for Markov state modeling, 539 of those were started with two protomers in the inward-facing state resulting in 280 µs of simulation time, and 605 with two protomers in the outward-facing state for a total of 315 µs of simulation time.
Most analysis will be done separately for both datasets to identify possible influences of the trimer configuration on dynamics of the translocating protomer, as some results indicated a difference between the systems. The average simulation length was 500 ns, as depicted in Figure 4.9.

During biased simulations fluctuations in the transport domain were found to be slightly above the values found in unbiased simulations started from the crystal structures *2NWX* [57] (OFC) and *3KBC* [63] (IFC). Since it is assumed that the translocation is a rigid body motion [63], the structural differences of the trimerization domain and transport domain towards the initial conformations (Figure 4.10) were compared to values found during unbiased simulations started directly from these crystal structures. A high structural difference would indicate deformations caused by the bias introduced during enhanced sampling. For the trimerization domain, both datasets feature conformations with a slightly higher RMSD towards both reference structures compared to the unbiased crystal simulations. Especially in the IIX dataset, the RMSD towards both structures rises well above 2 Å. While the RMSD is lower in the OOX dataset, the SD assumes conformations that are "equally different" from the two references, with an RMSD of just below 2 Å. Internal stability of the transport domain on the other hand is lower in the OOX dataset with values up to 3 Å while its stays below 2 Å in the IIX dataset (Figure 4.11). It should be noted that flexible loops and the most flexible part of hairpin 2 were excluded from the compared selections. According

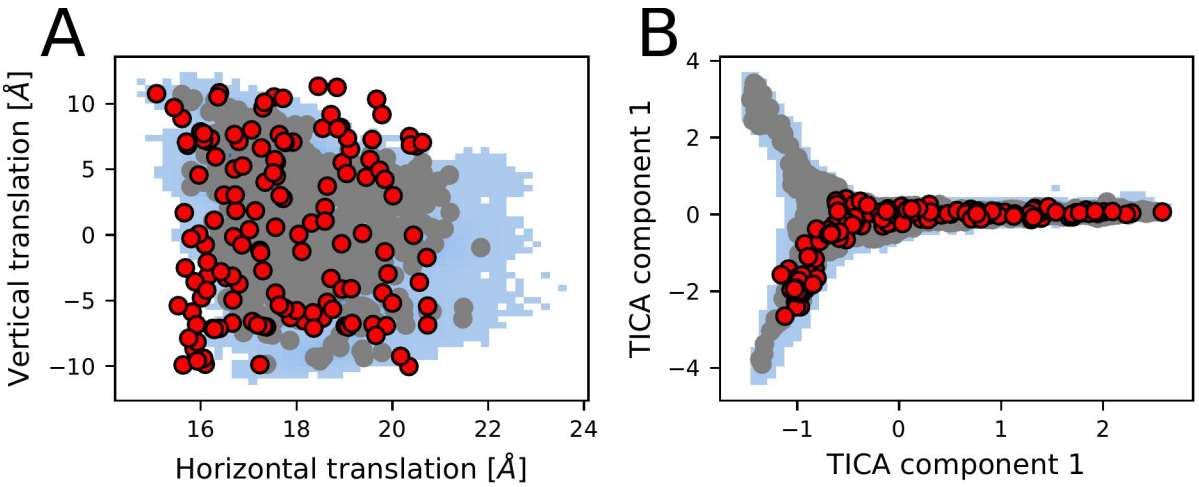

Figure 4.8: Each grey dot indicates the starting position of a OOX or IIX simulation used for markov state modelling, red dots indicate starting position of simulations directly derived from AWH simulations. **A**: Mapped along the two reaction coordinates used in AWH simulations **B**: Mapped into the OOX TICA space described in Section 4.2.3. The blue histogram in the background is computed on frames from all unbiased simulations and represents the complete conformational space explored.

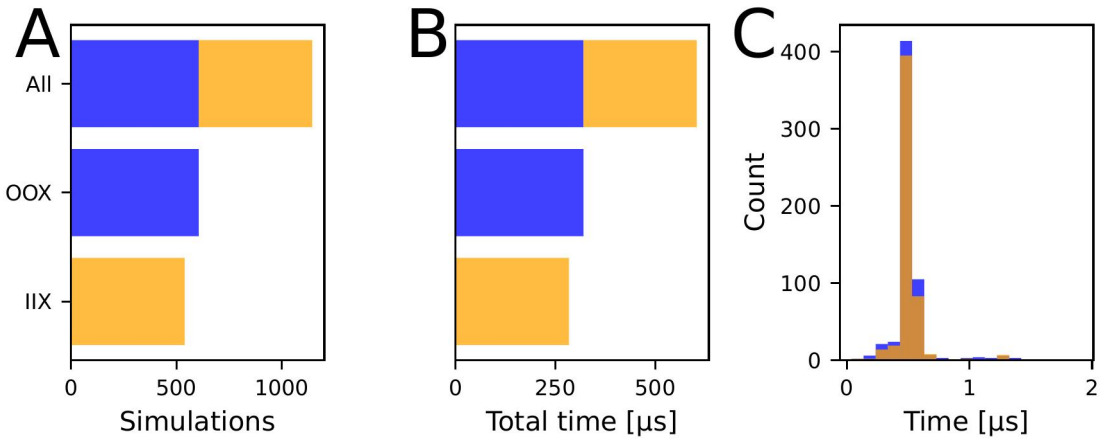

Figure 4.9: Aggregated number of simulations (**A**) and simulation time (**B**) of unbiased simulations used for the Markov state models as well as (**C**) a histogram depicting simulation lengths. Blue bars represent data from unbiased OOX simulations and orange bars represent data from unbiased IIX simulations.

to the RMSD, both end states (*2NWX* [57]/OFC and *3KBC* [63]/IFC) are reached with adequate precision, the *2NWX* [57] crystal structure, with an RMSD of 0.7 Å in OOX and IIX simulations, the *3KBC* [63] crystal structure with an RMSD of 0.7 Å in IIX simulations and 1.3 Å in OOX simulations (Figure 4.11). The published structures of the intermediate outward-facing (*3V8G* [72]), unlocked (*4X2S* [71]) and the allegedly chloride permeable state (ClCS, *6WYK* [73]) are described with an RMSD of 1.0 Å, 1.5 Å and 1.1 Å respectively in both datasets (Figure 4.11B and 4.11C). In contrast to these low RMSD values, both datasets feature an RMSD towards the *in silico* proposed and experimentally verified chloride conductive conformation (*ChC* [82]) of 2.3 Å (Figure 4.11C). For an overview of published structures and associated annotations, see Table 4.2.

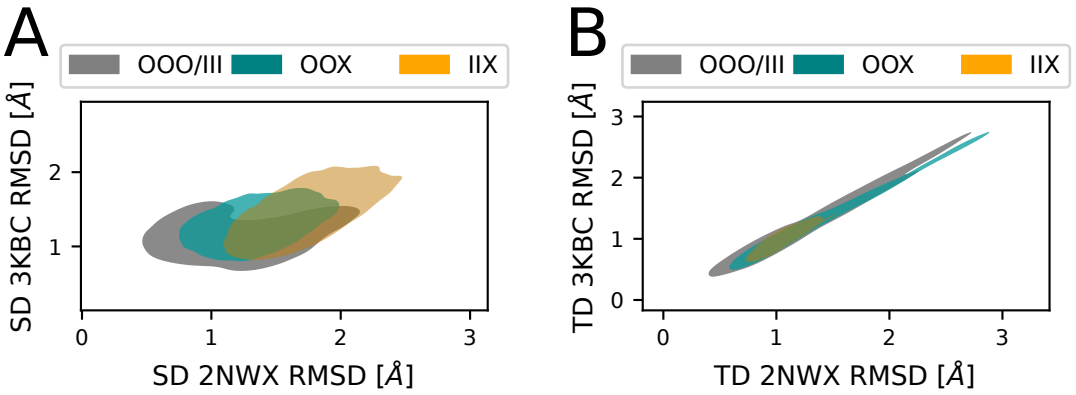

Figure 4.10: Internal RMSD of transport and trimerization domain during unbiased simulations of OOX and IIX trimers towards the outward- and inward-facing crystal structures.

Structure identifier PDB identifier	Annotation	Reference
IFC 3KBC	-Inward-facing state -Cross-linked	[63]
OFC 2NW	-Outward-facing state	[57]
iOFC 3V8G	-Possible intermediate -Close to OFC	[72]
Unlocked 4X2S	-Possible intermediate -Close to IFC -High horizontal distance between SD and TD -Cross-linked	[71]
ClCS 6WYK	-Possible intermediate -Close to IFC -Continuous water density between SD and TD -Cross-linked	[73]
ChC -	-Possible intermediate -Inbetween OFC and IFC -Anion pore formed and chloride permeations observed -Obatined via computational electrophysiology -Experimentally verified	[82]

Table 4.2: Table of published reference structures, their annotation, presumable relevance for translocation and the reference publication.

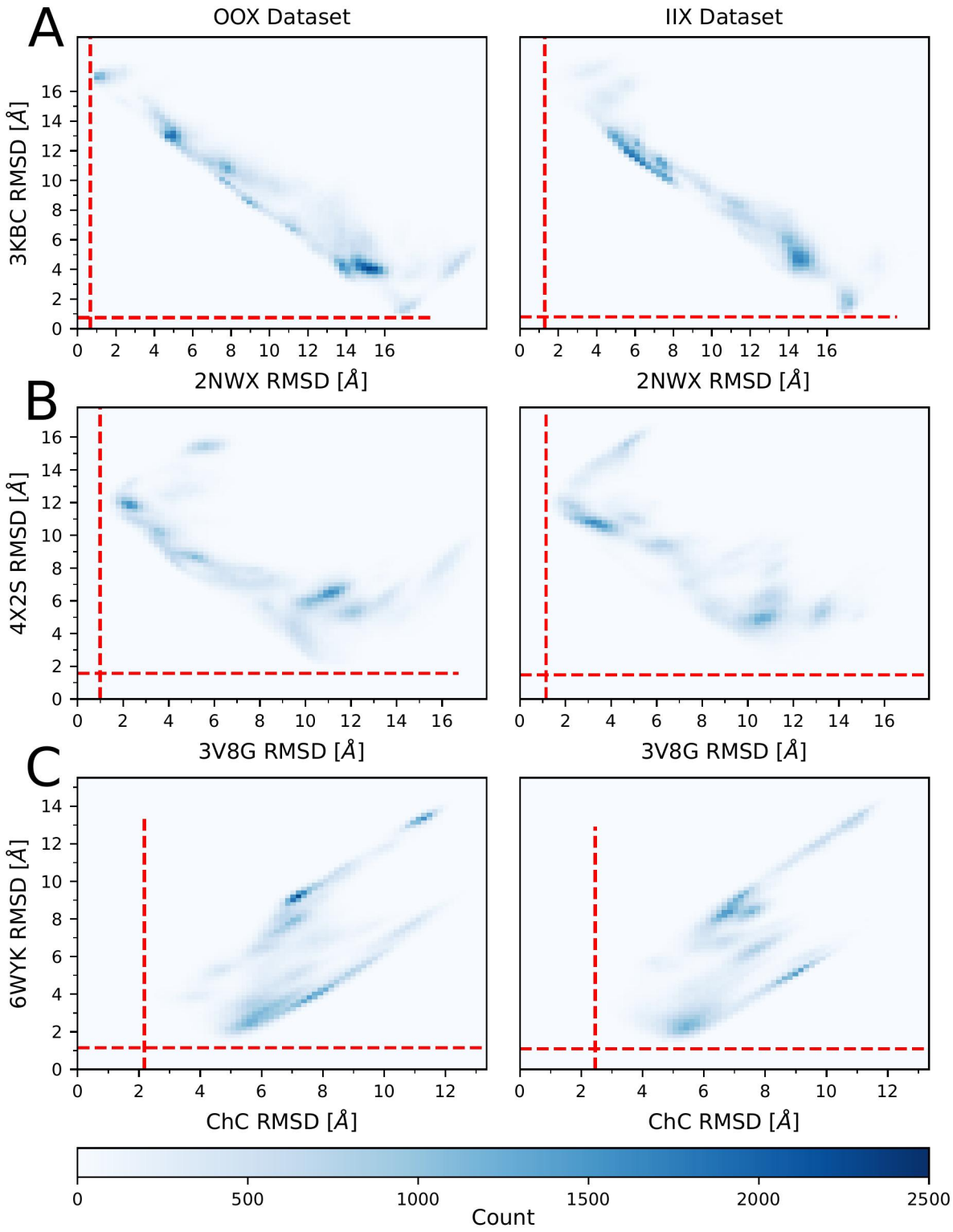

Figure 4.11: RMSD towards the published structures in the OOX (left) and IIX (right) dataset. **A**: 2NWX and 3KBC (OFS and IFS), **B**: 3V8G (intermediate OFC) and 4X2S (unlocked), **C**: ChC (chloride conductive conformation) and 6WYK (intermediate chloride conducting state). Dotted red lines indicate the minimum RMSD towards the origin axis in the OOX or IIX dataset.

4.2.2 Lipid density

To check whether there was an influence of the trimer configuration on the translocating protomer, density maps were computed for lipids in proximity to the translocating protomer. To obtain density maps with the translocating protomer in the same, or at least very similar, conformation all frames were assigned to one of 400 clusters. Clustering was done using K-means clustering [116] based on the first two TICA components obtained from the Cα-Cα distances of the OOX dataset. Frames from the same simulation and which were assigned to the same cluster were concatenated and used to construct 5 ns windows, these 5 ns windows were then used for density maps calculation. Next, the similarity between these density maps was computed using cross-correlation [117], it was found that density maps in the same cluster with the same protomer configuration showed a high correlation (one transitioning, two in outward or inward state) but density maps with different trimer configurations featured a low correlation (Figure 4.12). This resulted in a significantly lower average similarity between OOX and IIX density maps compared to OOX-OOX and IIX-IIX pairings. These differences hint either at substantial differences between the lipid-protomer interactions of OOX and IIX trimers, or protomer-lipid interactions that require specific conformations of the protomer and long timescales to form. To verify, or dispute, this finding further analysis was done for OOX and IIX systems separately.

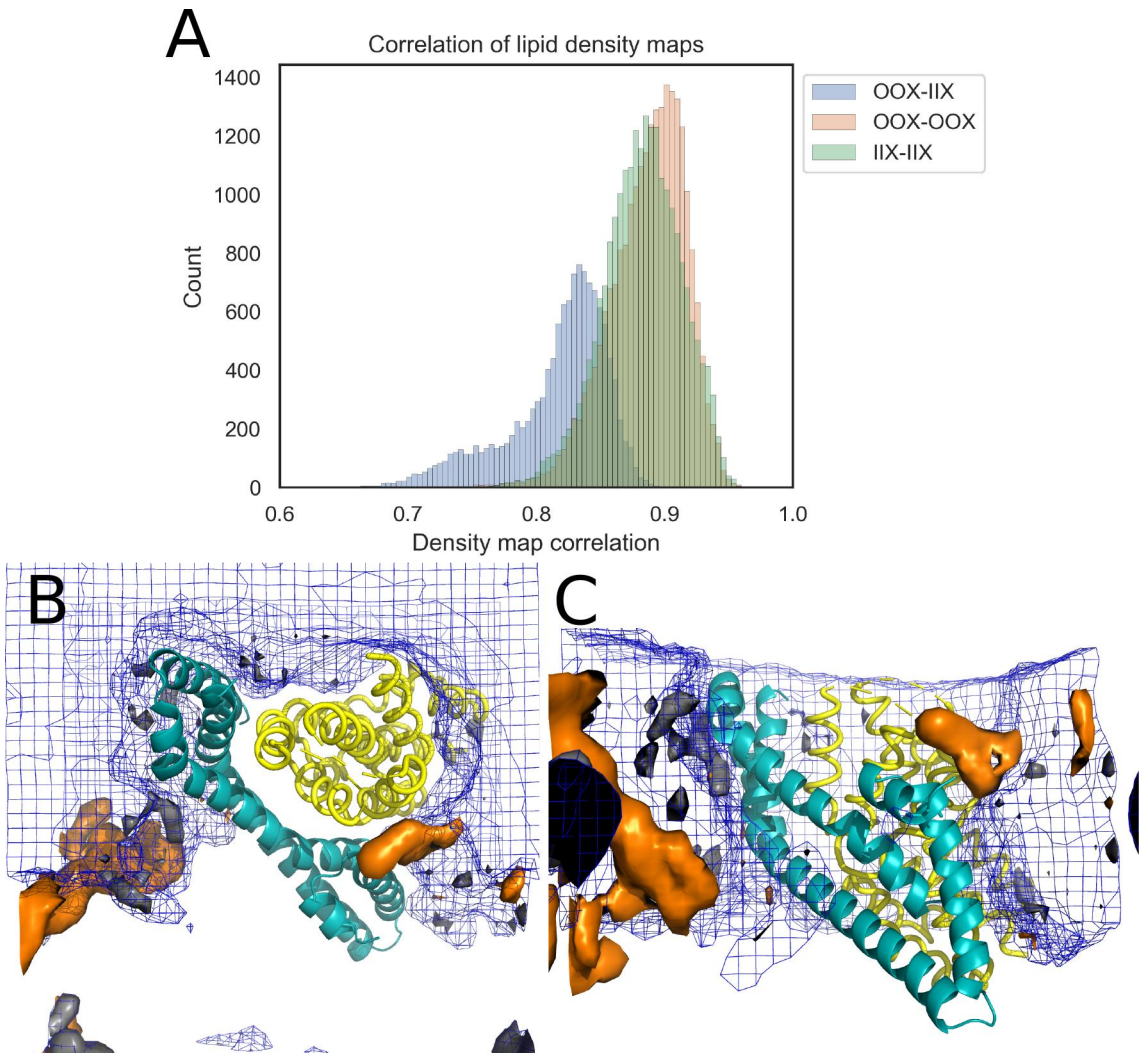

Figure 4.12: **A**: Histogram of cross-correlation between lipid density maps. **B** and **C**: Top (**B**) and (**C**) side view of a representative clusters averaged protomer embedded in the lipid bilayer with corresponding lipid density maps. Trimerization domain in cyan, transport domain in yellow. Lipid density from OOX simulations in blue. Orange surface represents lipid density exclusive to IIX simulations, grey surface represent lipid density exclusive to OOX simulations.

4.2.3 Free energy landscape of translocation

Two dimensions were determined to be appropriate for dimensionality reduction with TICA, since visually two dominant slow components in the OOX ITS plot (Figure 4.13) could be identified. Additional dimensions did not show an increase in descriptive power of the model, instead, the higher dimensionality resulted in lower cluster populations and worse models. Analysis of the implied time scales showed that the speed of the slowest component keeps decreasing up until a lag time of 300 ns. At around 50 ns the increase of the slowest component starts to slow down, while all faster components appear to be constant. Convergence of the two-dimensional TICA landscape was observed at 50ns and this lag time was used for all further analysis. While a higher lag time would have been favorable when considering the implied time scales, the average simulation length of 500 ns limited the maximum lag time to 50 ns. In the last step, the data was discretized into 400 microstates using K-means clustering [116] as implemented in PyEMMA [101]. Clustering was guided by the VAMP2-score [110] of MSMs build with a varying number of clusters, VAMP2-score for different numbers of clusters is shown in Figure 4.14. Mapping OOX and IIX data separately, along the first two TICA eigenvectors, reveals very different landscapes and indicates different dynamics for a protomer with two neighbors in outward or inward-facing conformation, as seen in Figure 4.15.

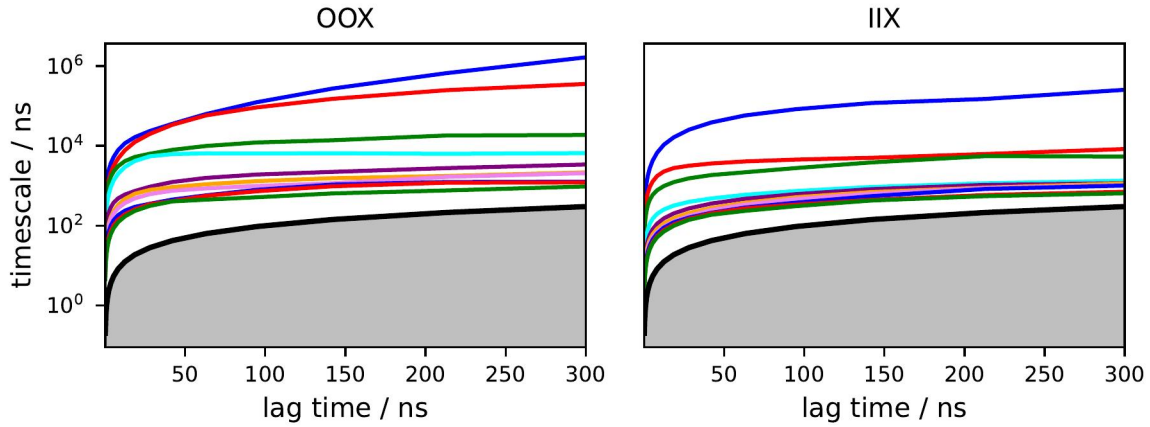

Figure 4.13: Implied timescales plot for the OOX and IIX datasets based on Cα-Cα distances between every fifth Cα of transport and trimerization domain, used for TICA lagtime selection.

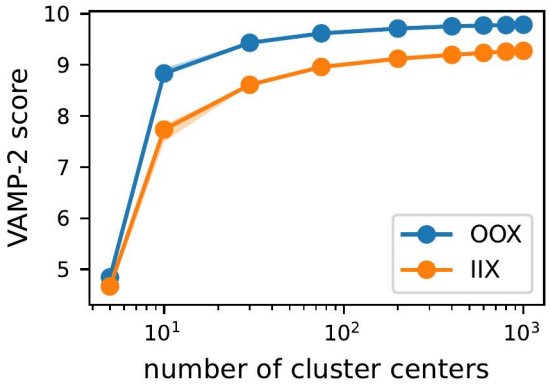

Figure 4.14: Number of cluster centers vs. VAMP2-score of MSMs build using these discretizations. Used for computation of cross-correlation between lipid density maps.

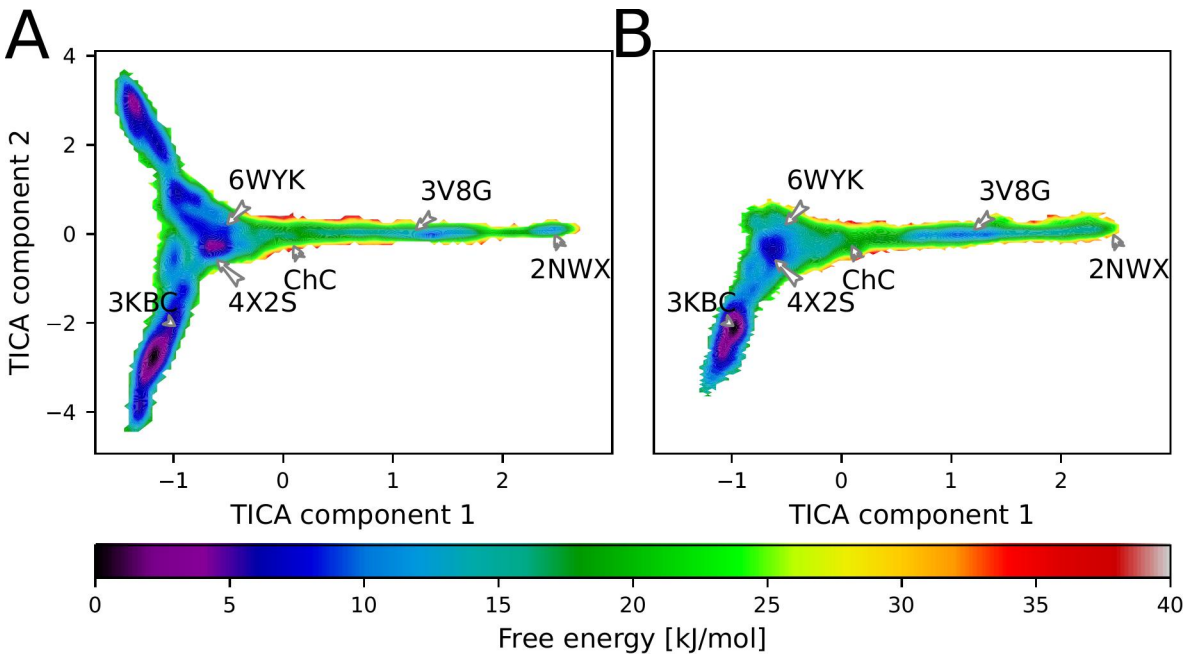

Figure 4.15: Free energy along the first two TICA components of unbiased simulation from the OOX (**A**) dataset and from the IIX (**C**) dataset. Energy profiles were computed based on a high resolution 400 state MSM and weighted according the stationary distribution.

4.2.4 Machine learning guided few-state discretization

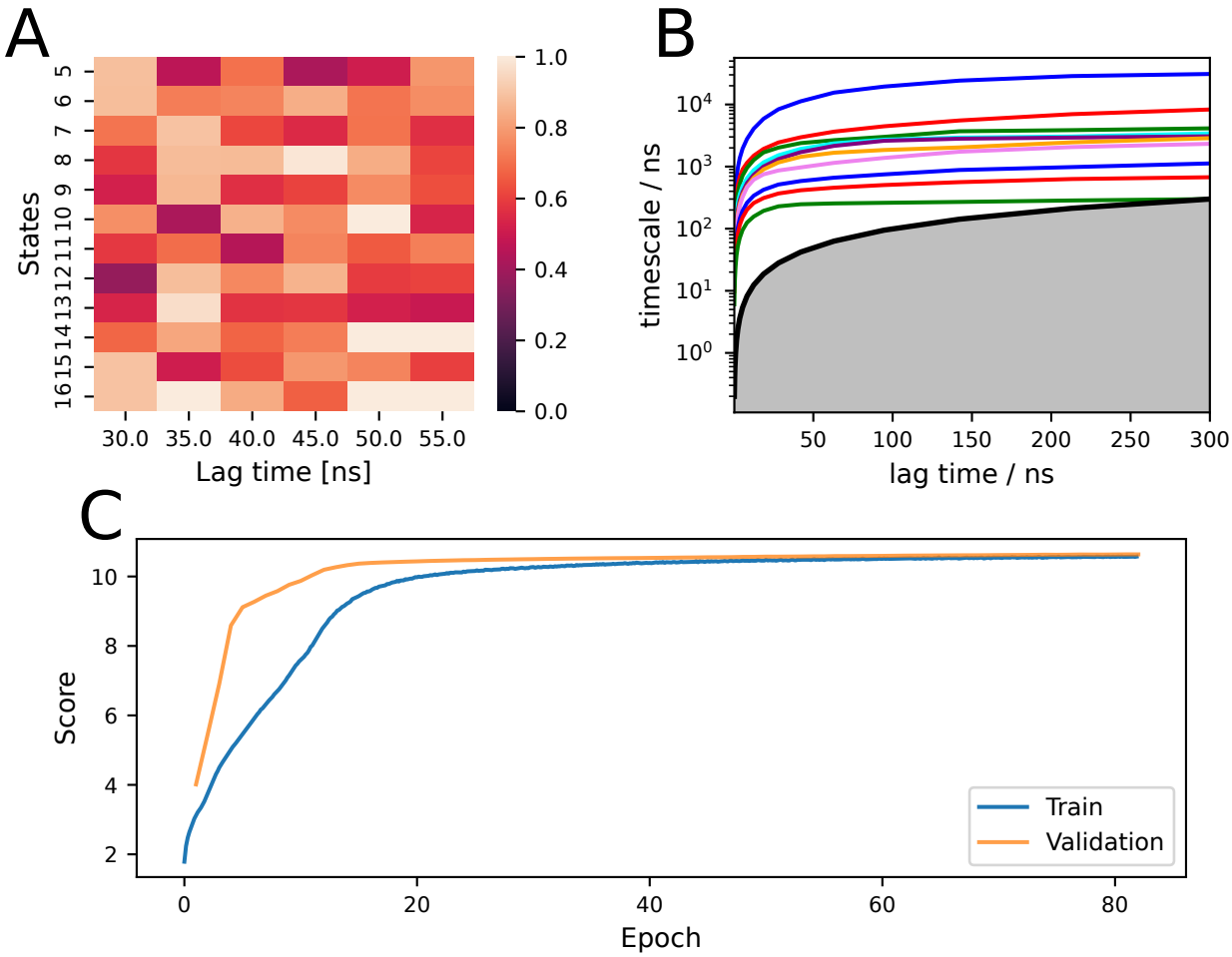

Figure 4.16: **A**: Combined error from ITS and CK test for VAMPNet models trained with different lag times and number of states. **B**: Implied timescales of the best performing model with 12 states and a lag time of 30ns. **C**: Test and validation score during training of a 12 state VAMPNet with a lag time of 30ns on simulations of the OOX dataset.

According to the method described in Section 3.3.5, all models trained on the OOX dataset were evaluated. A 12 state model with a lag time of 30 ns was found to yield the lowest combined error from the ITS and CK test, which is shown in Figure 4.16. Both tests used to verify the performance of the resulting MSM, CK and ITS plot, showed an advantage for the VAMPNet based MSMs. Especially in the ITS plot the implied timescales were quicker to converge, 30 ns for the VAMPNet based model and 300 ns for the traditional one. This analysis was limited to the unbiased OOX simulations since preliminary results indicated that the energy landscapes of a IIX timer is substantially different from a OOX trimer and the fully bound OOX trimer represents a physiological relevant state compared to a less physiological fully

bound IIX trimer. In Figure 4.16, the validation score is above the training score during the first training phase. One explanation for this is the use of dropout layers during training, every time the network is fed another batch, the connectivity between nodes changes, which makes it more difficult for the network to fit the data. During calculation of the validation score, all connections are used, and the complete network can describe the given validation batch better than the truncated one used to calculate the training score. An alternative explanation is an imbalance of the validation and training dataset, it is possible that rare conformations are not represented in the validation dataset. These rare conformations might be hard to fit, and thus the training score will suffer, if the validation dataset contains mainly common conformations the network will score better on this dataset. The distribution of the 12 states along the two TICA components is shown in Figure 4.17. Figures 4.19 and 4.20 depict representative structures for each state shown from the front, side and top.

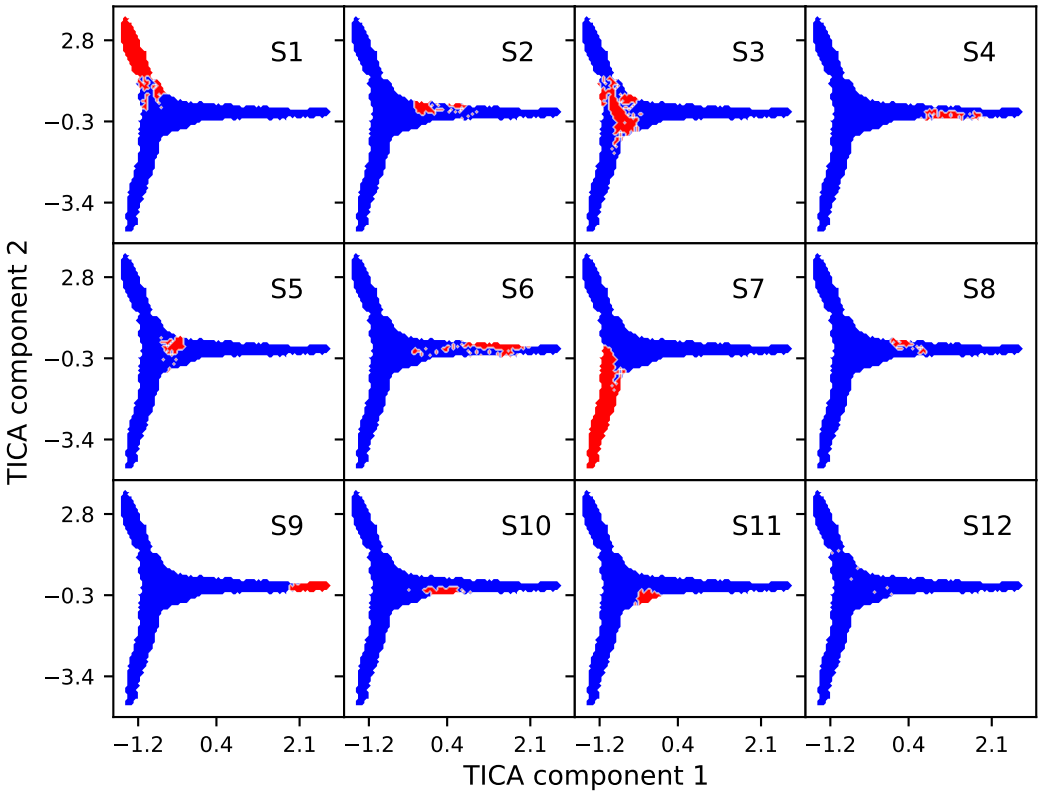

Figure 4.17: Distribution of the 12 VAMPNet states in TICA space. Red indicates area assigned to the state shown in the upper right, blue indicates area assigned to a different state.

To get a first impression of the functional relevance of each state, the minimum RMSD of all known structures towards each state was computed, results are shown in Table 4.3.

State	Samples	2NWX RMSD	3KBC RMSD	3V8G RMSD	4X2S RMSD	6WYK RMSD	ChC RMSD
1	143.814	12.0 Å	2.57 Å	8.19 Å	2.54 Å	1.81 Å	4.24 Å
2	168.702	4.36 Å	6.94 Å	2.09 Å	4.55 Å	4.06 Å	4.56 Å
3	366.363	10.78 Å	2.25 Å	6.84 Å	3.54 Å	1.20 Å	3.01 Å
4	179.615	2.36 Å	8.81 Å	**0.99**Å	8.74 Å	5.63 Å	4.87 Å
5	149.979	9.30 Å	3.00 Å	6.32 Å	**1.56**Å	1.30 Å	3.62 Å
6	173.804	2.52 Å	5.14 Å	1.98 Å	5.43 Å	2.79 Å	4.28 Å
7	165.489	14.11 Å	**0.75** Å	10.90 Å	2.78 Å	2.42 Å	6.04 Å
8	103.308	5.99 Å	6.23 Å	2.20 Å	5.66 Å	3.35 Å	3.74 Å
9	80.172	**0.66** Å	14.05 Å	2.75 Å	13.06 Å	10.82 Å	8.87 Å
10	66.232	7.07 Å	4.72 Å	3.01 Å	6.16 Å	2.21 Å	**2.18** Å
11	32.561	9.45 Å	4.11 Å	5.08 Å	4.41 Å	2.00 Å	4.24 Å
12	10.170	4.35 Å	1.98 Å	2.24 Å	2.94 Å	**1.16** Å	3.35 Å

Table 4.3: Table of minimum RMSD towards each published structure for each VAMPNet state. Bold text indicates the lowest RMSD towards the corresponding reference structures. A green background indicates the lowest RMSD in the corresponding state.

When transforming Cα-Cα distances from unbiased simulations started from the crystal structures *2NWX* [57] (OFC) and *3KBC* [63] (IFC) into VAMPNet states, only states $S9$, respectively, $S7$ are visited. This is consistent with the minimum RMSDs since the closest structure for $S9$ is *2NWX* [57] and *3KBC* [63] for $S7$. The structure of $S9$ is visually indistinguishable from *2NWX* [57] and $S7$ is very close to *3KBC* [63] except for HP1, which is slightly further inward (1.8 Å) in 7 compared to the crystal structure. In state $S4$ conformations with a minimum RMSD of 0.99 Å towards *3V8G* [72] were found. The structure of $S4$ shows the same slightly more inward transport domain, compared to *2NWX* [57], one can find in *3V8G* [72], but the rotation is less pronounced. For the supposedly chloride-permeable *6WYK* [73] state, $S12$ represents the closest match with a minimal RMSD of 1.16 Å, followed by state $S3$ with an RMSD of 1.20 Å. In $S12$ the biggest structural difference to *6WYK* [73] is an approximately half a helix turn upward shift (about 2.3 Å) of the transport domain. In the structures of $S3$ HP1 is 3.3 Å closer to the trimerization domain than in *6WYK* [73]. For the chloride permeable conformation (*ChC* [82]), proposed by computational electrophysiology, state $S10$ features the lowest RMSD (2.18 Å), here the transport domain of the structure of $S10$ is 2.5 Å closer to the trimerization domain compared to *ChC* [82]. State $S5$ shows the highest similarity to the "unlocked" conformation *4X2S* [71] (RMSD of 1.56 Å), but the RMSD towards *6WYK* [73] (1.3 Å) is even lower. $S5$

is the state with the largest horizontal TD-SD distance (20 Å). Compared to *4X2S* [71], the transport domain of the structure of $S5$ is more outward (about 7 Å) and the distance between the tips of hairpin 1 and hairpin 2 is 8.8 Å vs. 5 Å in the crystal structure. Compared to *6WYK* [73], $S5$ features a lower rotation of the transport domain but the same vertical position. The states $S2$, $S6$, $S8$, $S10$ and $S11$ do not feature an RMSD below 2 Å towards any known structure. The structures of $S2$, $S6$ and $S8$ are similar and halfway between *3V8G* [72] and *6WYK* [73], with $S2$ featuring the highest horizontal distance of the three. A second group is formed by $S10$ and $S11$, these are roughly 3.5 Å further inward than the previous group and feature a horizontal distance between transport and trimerization domain of only 16.5-17 Å. $S10$ is the state with the lowest horizontal TD-SD distance (16.5 Å) and $S5$ features the highest distance (19.96 Å). Notably, $S10$ is also the state which is closest to *ChC* [82] with an RMSD of 2.18 Å. The stationary distribution, shown in Figure 4.18, of the states and their associated Free Energy show that states $S3$, $S1$, $S5$ and $S7$ seem to be dominant. In states $S10$ and $S11$, the hairpin is closed, in states $S8$ and $S9$ the overwhelming

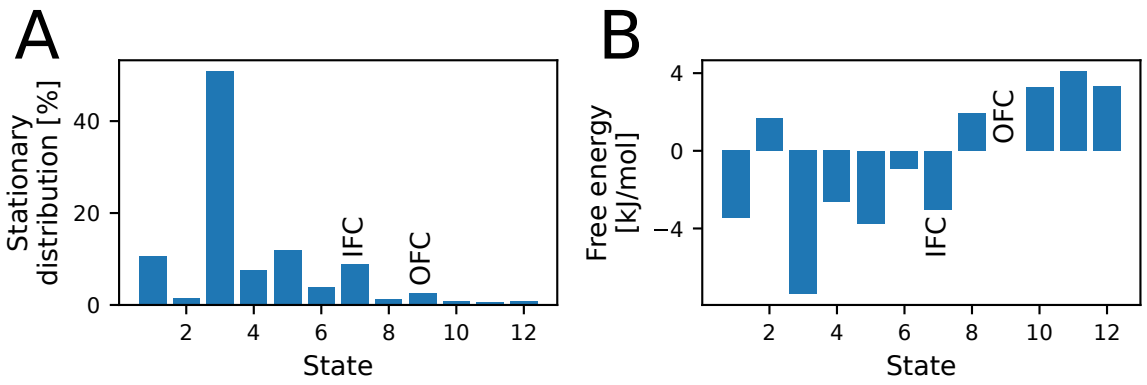

Figure 4.18: Stationary distribution (**A**) and associated Free Energy (**B**) for each of the 12 states defined by the best performing VAMPNet model. In **B**, the OFC state ($S9$) was set equal to zero and all values were adjusted accordingly.

majority of conformations feature a closed hairpin. Open hairpin conformations can be found in states $S1$, $S5$ and $S7$, here the majority features an open or half-open (7 Å-10 Å) state. The states $S6$ and $S12$ show ambiguous distributions, two populations in state $S12$ (closed and half-open) and two or three in state $S6$ (closed, half-open, open)

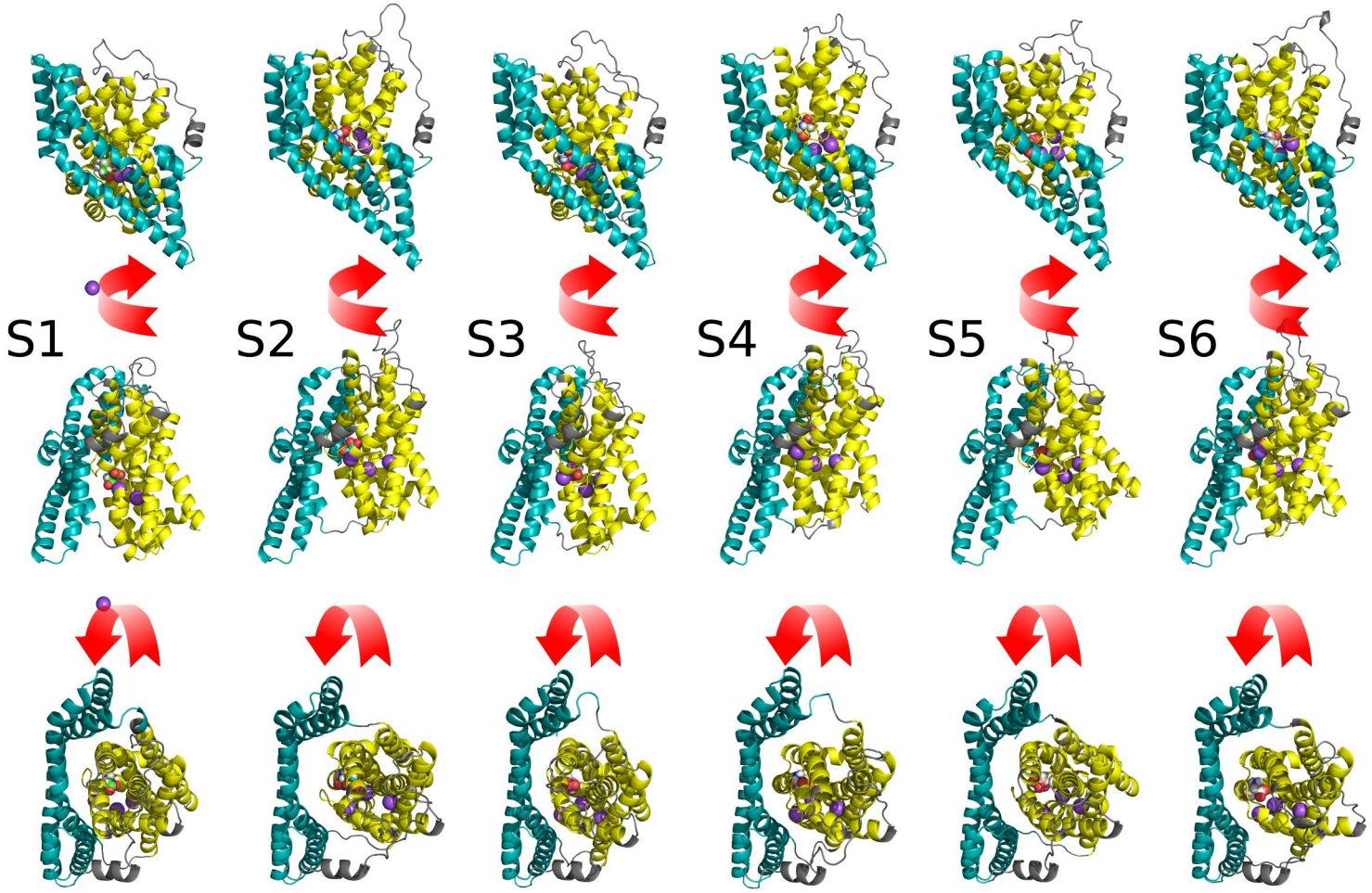

Figure 4.19: Front (A), Side (B), Top (C) view of representative structures for each VAMPNet state. Trimerization domain in cyan, transport domain in yellow, bound sodiums magenta spheres, red, blue and white spheres represent a bound aspartate molecule.

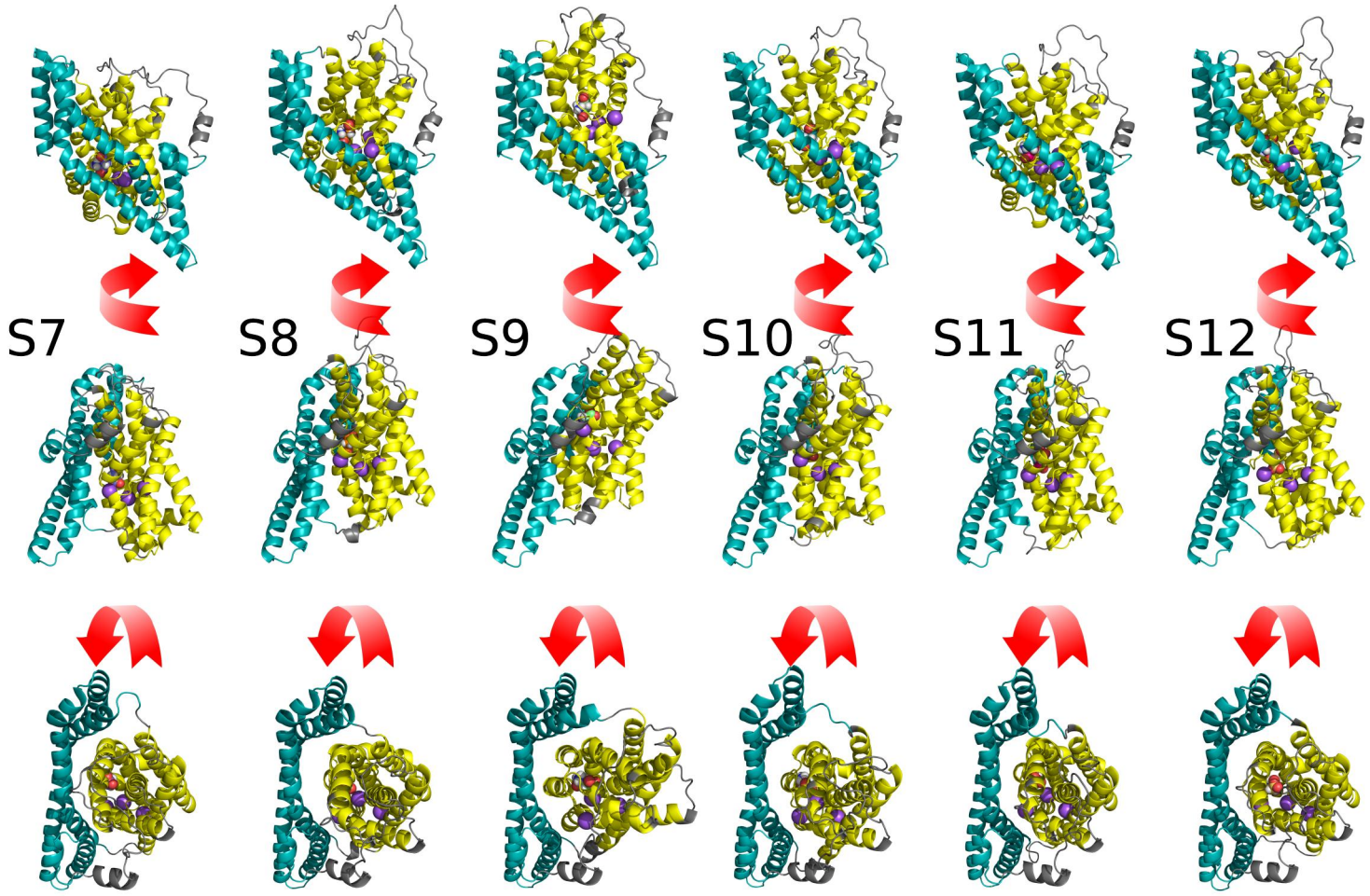

Figure 4.20: Front (A), Side (B), Top (C) view of representative structures for each VAMPNet state. Trimerization domain in cyan, transport domain in yellow, bound sodiums magenta spheres, red, blue and white spheres represent a bound aspartate molecule.

4.2.5 Mapping experimental structures on the conformal landscape

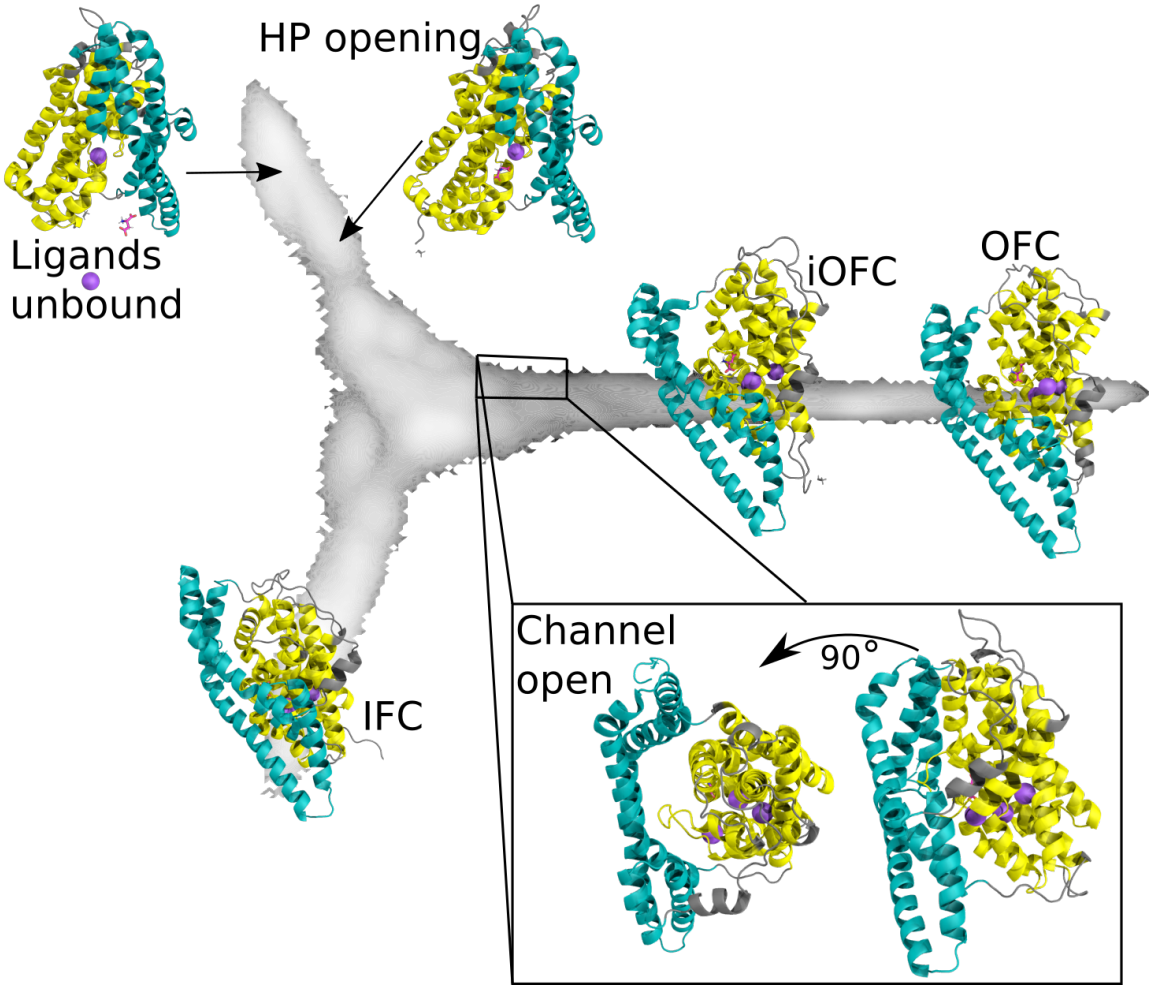

Figure 4.21: Landscape of the OOX dataset in OOX TICA space with prominent structural features highlighted.

In both datasets the inward- and outward-facing states are well separated along the first two TICA components. The maximum separation between the OFC (*2NWX* [57]) and IFC (*3KBC* [63]) is found along the first component (Figure 4.21), while the second component separates the inward-facing state from intermediate ones (*4X2S* [71], *6WYK* [73]). Mapping previously published structures into this space places them in between the two extremes (IFC and OFC) and their distance towards the two extremes lines up with their proposed relationships along the translocation between OFC and IFC. For example, the *3V8G* [72] structure is described as an outward-facing conformation that moved slightly inward. In the TICA projection it is placed close to

2NWX [57], slightly shifted along TICA component one, towards *ChC* [82] which has been described as being more inward than *3V8G* [72]. The unlocked structure *4X2S* [71] is placed in-between the inward conformation and the two channel associated structures, in agreement with its description when published. It is noteworthy, that all structures obtained experimentally (*2NWX* [57], *3KBC* [63], *3V8G* [72], *4X2S* [71], *6WYK* [73]) are placed in or nearby local energy minima, while the structure proposed by computational electrophysiology *ChC* [82] is placed in a region in-between the minima with a slightly higher energy. The location of these minima depends on the dataset. In the IIX dataset, the minimum nearby the *4X2S* [71] structure is shifted downward compared to its counterpart from the OOX dataset. The minimum next to *3KBC* [63], on the other hand, is shifted slightly upward in the IIX data, now matching the position of the inward-facing conformation *3KBC* [63]. In the OOX dataset, the corresponding minimum seems to be slightly more inward than the published inward-facing conformation.

4.2.6 Inward open state

Another prominent difference between the datasets is the presence of a novel region in the OOX dataset, see Figure 4.15 for a comparison of the OOX and IIX energy landscape. This region is missing in IIX simulations, here the free energy profile indicates an energy barrier at the joint region, while this is a local minimum in the OOX data. Of the previously described protein conformations, none is placed in this area. Mapping distances between the two hairpin tips, which form the intra- and extracellular gate onto the TICA surface, reveals that conformations in the upper region do feature a higher distance between the hairpin tips than conformations around the *3KBC* [63] crystal structure in the OOX dataset (Figure 4.24). This region also features higher distances towards NA2, and the majority of simulations with ligand unbinding are located here (Figure 4.22). By means of structural similarity, this region is most similar to the *6WYK* [73] structure with a minimum RMSD of 1.81 Å. We did not observe permeations during simulations in this area, although the hairpin is wide open in the representative conformation, and the most similar crystal structure (*6WYK* [73]) represents an open channel conformation. In the IIX dataset, on the other hand, while the upper region is non-existing and values for HP-HP, NA2 and ligand distance are different, too.

For example, the hairpin opens up wider in conformations slightly below the crystal inward-facing conformation with values similar to those in the upper region in the OOX dataset. Based on these results the conformations in the novel region presumable represent an alternative inward-facing state with an easily accessible binding site.

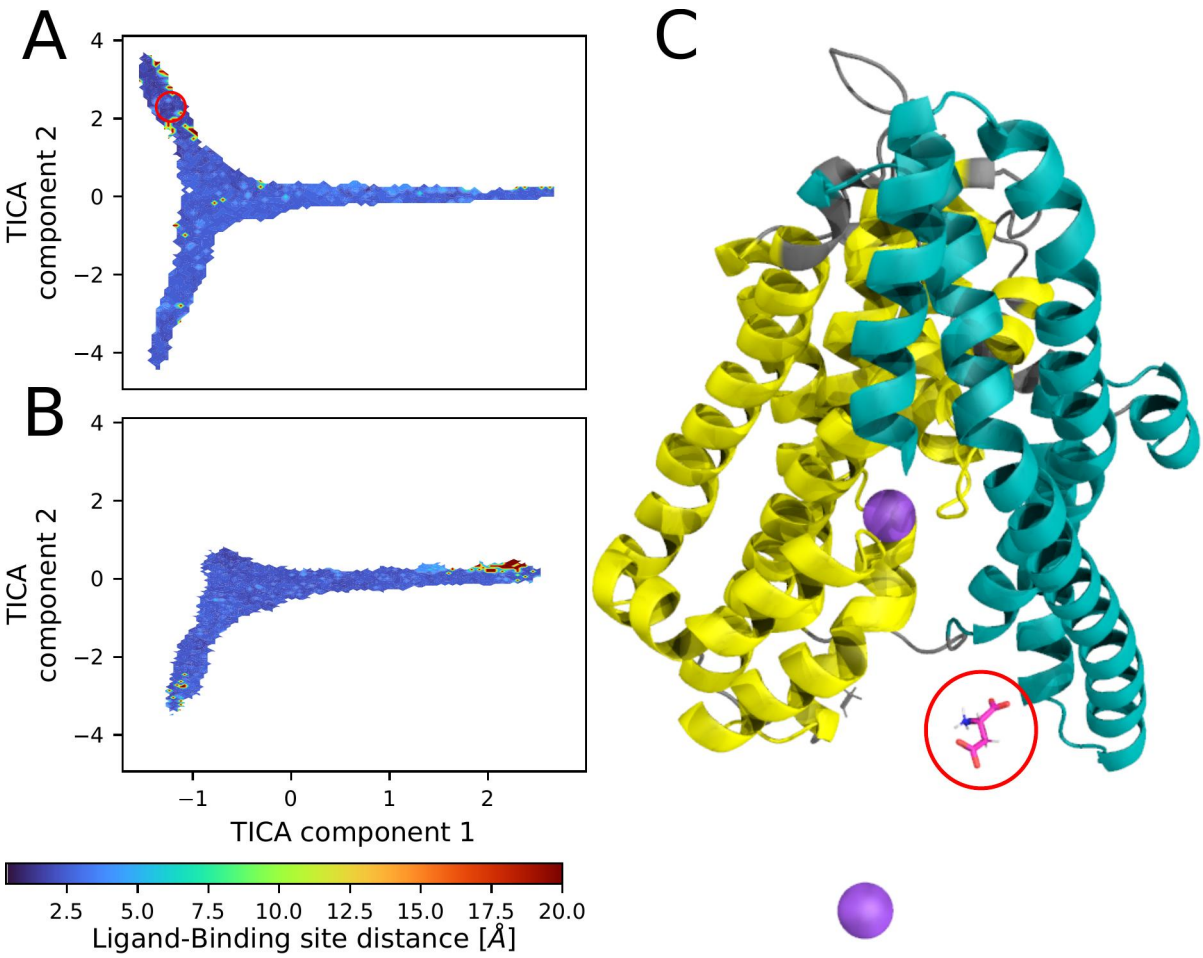

Figure 4.22: Distance between the bound amino acid and its binding site in the translocating protomer (capped at 20 Å) mapped onto the landscape of the OOX (**A**) and IIX (**B**) dataset in the TICA space derived from the OOX dataset. **C** shows a representative structure of a conformation with a unbound ligand (red circle) extracted from the red encircled region in A. Transport domain in yellow, trimerisation domain in cyan.

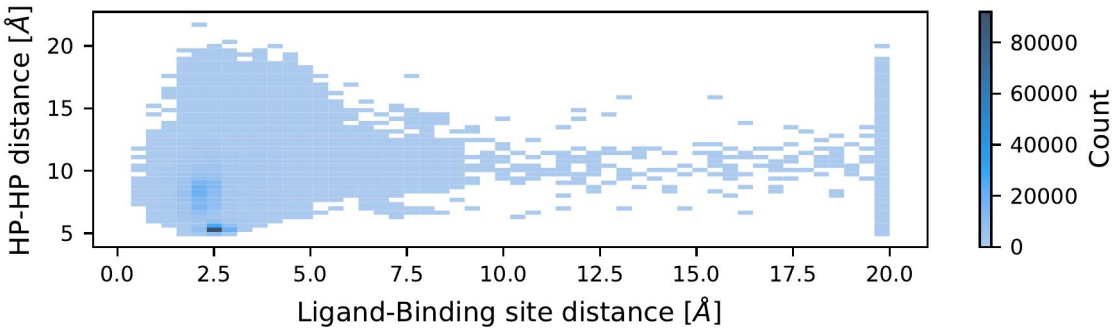

Figure 4.23: Distance between the transported amino acid and its binding site (capped at 20 Å) versus the distance between tips of hairpin 1 and hairpin 2.

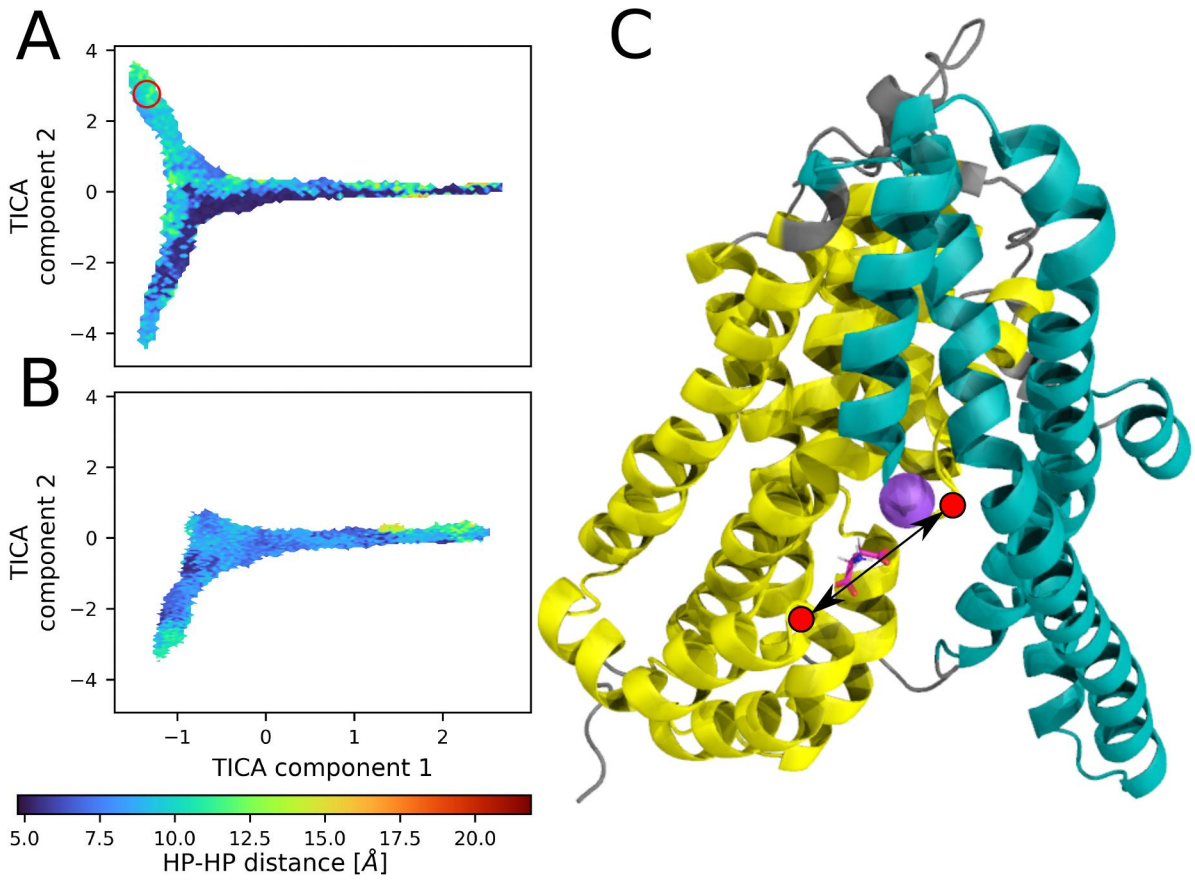

Figure 4.24: Distance between tips of hairpin 1 and hairpin 2 mapped onto the landscape of the OOX (**A**) and IIX (**B**) dataset in OOX TICA space. **C**: Representative structure of a open hairpin conformation extracted from the red encircled region in the OOX dataset in **A**. Transport domain in yellow, trimerisation domain in cyan.

4.2.7 Channel activity and water permeations

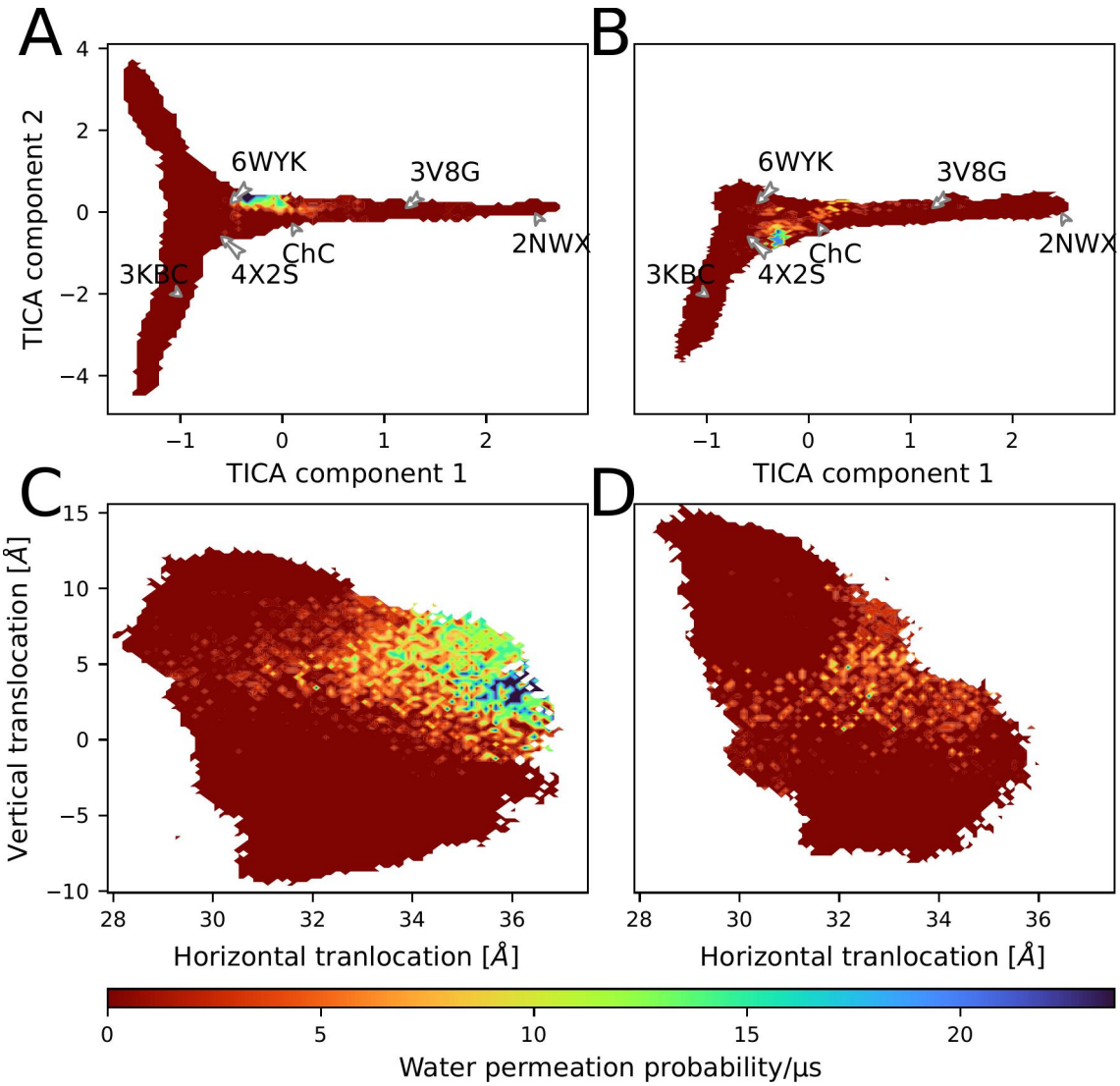

Figure 4.25: Permeation probability per μs computed on 400 microstates in OOX (**A**) and IIX (**B**) simulations mapped along the first two TICA components. **C** and **D**: Permeation probability mapped along the reaction coordinates defined for enhanced sampling.

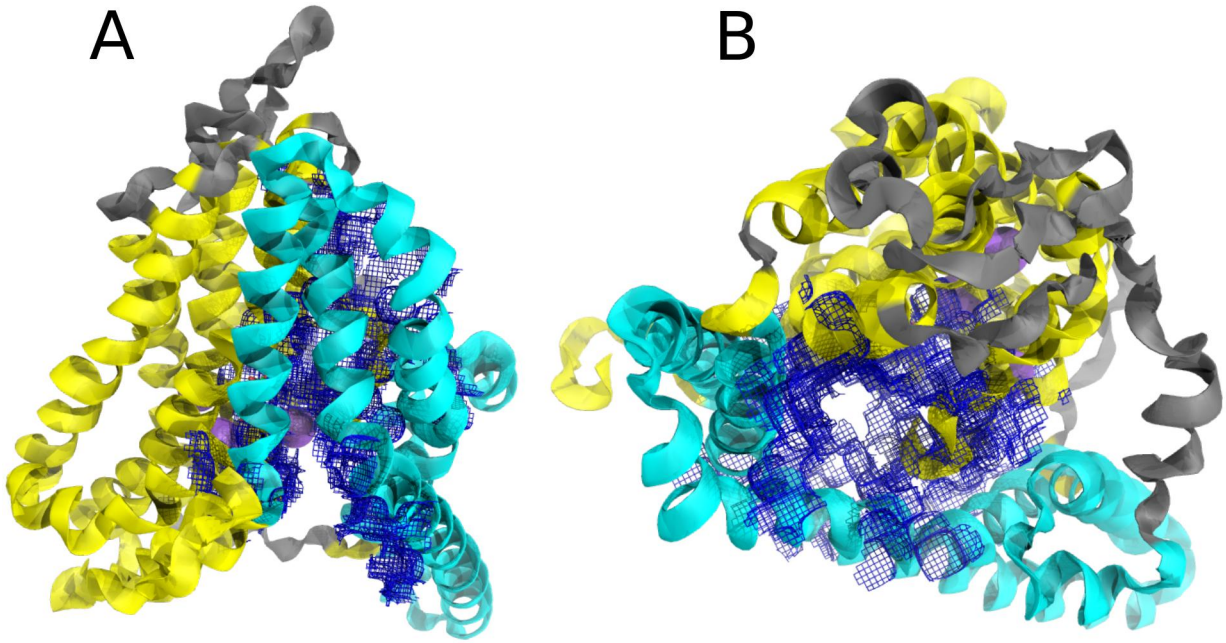

Figure 4.26: Top (**A**) and side (**B**) view of a representative water permeable conformation extracted from an unbiased simulation of the OOX dataset, water density (0.05σ) is represented by a blue mesh. Transport domain in yellow, trimerization domain in cyan.

An open question is at which point along the translocation pathway the protomer is able to enter a chloride permeable conformation. We used water permeations through the protein, as a proxy for chloride permeability, as we assume that water-permeability is a prerequisite for chloride permeability, although not a guarantee. Using water permeability as a proxy offered the advantage that there are about 50k water molecules in the simulation system compared to 217 chloride ions, making water permeation more likely than observing chloride permeation. In total, we found 489.224 water permeation events in the OOX dataset and an additional 125.300 events in the IIX dataset. It is noteworthy, that we found 3.9 times more permeations in the OOX simulation than in IIX simulations, while the ratio of data is only 1.16 in favor of OOX data. When projecting permeations in TICA space, like done in Figure 4.25, it becomes clear that water-permeable conformations are confined to a small but well-defined area in both datasets. Said area is adjacent to three published structures, one crystal structure which is said to represent an open channel conformation (*6WYK* [73]) another crystal structure representing an unlocked state (*4X2S* [71]) and one proposed by computational electrophysiology (*ChC* [82]). None of the published structures is located within the permeable region of the OOX dataset, but for the IIX dataset, the *ChC* [82] structure is inside the permeable region, as seen in Figure 4.25A and B. When comparing the permeable regions in the OOX and IIX datasets, it can be seen

that in the IIX data it is shifted downwards compared to OOX and thus closer to the structures of *4X2S* [71] and *ChC* [82]. This shift of the permeable region can also be seen in Figure 4.25C, which shows permeability along the vertical transition and the horizontal distance between the two domains. The permeable conformations form defined regions inside the TICA space, but none of the TICA components correlates well with the permeation probability.

Mapping permeability on the 12 states, as done in Figure 4.27, shows that states S2 and S5 feature higher permeation probability.

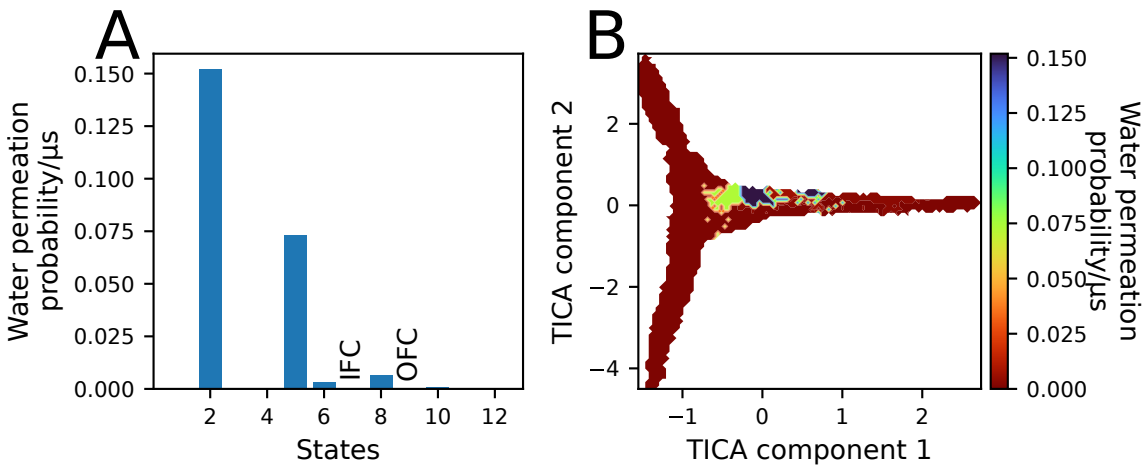

Figure 4.27: **A**: Water permeation probability per μs per state as defined by the 12 state VAMPnet. **B**: Water permeation probability computed on 12 states as defined by VAMPNet and mapped along the first two TICA components.

4.2.8 Translocation pathways

Transition paths were derived from a Bayesian MSM, build using the state probabilities obtained from the 12 state VAMPNet, which was identified as the best performing one. The highest flux pathway represents 18.9% of the total flux and the top four pathways represent 55% of the total flux (Figure 4.28A). Figure 4.28B and C show that paths responsible for a large fraction of transitions feature very low permeation probabilities, while those with a high permeation probability feature low transition rates. Figure 4.30 depicts the mean first passage time (MFPT) between the states along the four highest flux pathways for the physiological relevant outward to inward transition. All pathways feature two or more transitions with an MFPT above or close to 40 μs. The MFPT for the physiological transition of a fully bound protomer from the outward-facing into the inward-facing conformation is 46 μs with a standard deviation of 2.5 μs, compared to 345 μs ($\pm$ 34 μs) for the nonphysiological fully bound inward to outward transition.

Path	Most similar conformations along path
1	S9 OFC (0.66 Å) ⇒ S4 iOFC (0.99 Å) ⇒ S6 iOFC (1.98 Å) ⇒ S3 ClCS (1.20 Å) ⇒ S7 IFC (0.75 Å)
2	S9 OFC (0.66 Å) ⇒ S4 iOFC (0.99 Å) ⇒ S6 iOFC (1.98 Å) ⇒ S2 iOFC (2.09 Å) ⇒ S5 ClCS (1.30 Å) ⇒ S3 ClCS (1.20 Å) ⇒ S7 IFC (0.75 Å)
3	S9 OFC (0.66 Å) ⇒ S4 iOFC (0.99 Å) ⇒ S8 iOFC (2.20 Å) ⇒ S12 ClCS (1.16 Å) ⇒ S3 ClCS (1.20 Å) ⇒ S7 IFC (0.75 Å)
4	S9 OFC (0.66 Å) ⇒ S4 iOFC (0.99 Å) ⇒ S8 iOFC (2.20 Å) ⇒ S2 iOFC (2.09 Å) ⇒ S5 ClCS (1.30 Å) ⇒ S12 ClCS (1.16 Å) ⇒ S7 IFC (0.75 Å)

Table 4.4: Table of minimum RMSD along transition paths obtained from a markov state model build on the states assigned by a 12-state VAMPNet model.

Assigning the closest crystal structure to each state along the path, like shown in Table 4.4, reveals that the first three paths show the same pattern of transitioning from the OFC to an iOFC state, from iOFC to a ClCS like conformation and finally into the IFC, this is also visualized in Figure 4.29. Although all paths feature high similarity (RMSDs of 1.2 Å) towards a proposed permeable channel structure (ClCS), none of them feature considerable water permeation. Inspecting Figures 4.31, 4.32, 4.33 and 4.34, which depict vertical movement (translocation), horizontal distance between SD and TD and rotation of the TD, shows that all paths feature vertical translocation and rotation. All four pathways feature a linear decreasing rotation, starting at 70° until about 63°, here a rather steep change of rotation from 64° to 56° occurs. This jump is followed by another section with a linear decline from 56° to 54°. In only half of the pathways this jump is accompanied by a negative difference in energy Δ -6 kJ/mol (Figure 4.31D) for the first pathway and Δ -7 kJ/mol (Figure 4.34D) in the

fourth pathway. For pathways two and three the change in energy is less favorable, Δ -4 kJ/mol (Figure 4.32D) and Δ -0.5 kJ/mol (Figure 4.33D), respectively. Just as all four pathways show declining rotation, they do show an increasing distance between the two domains.

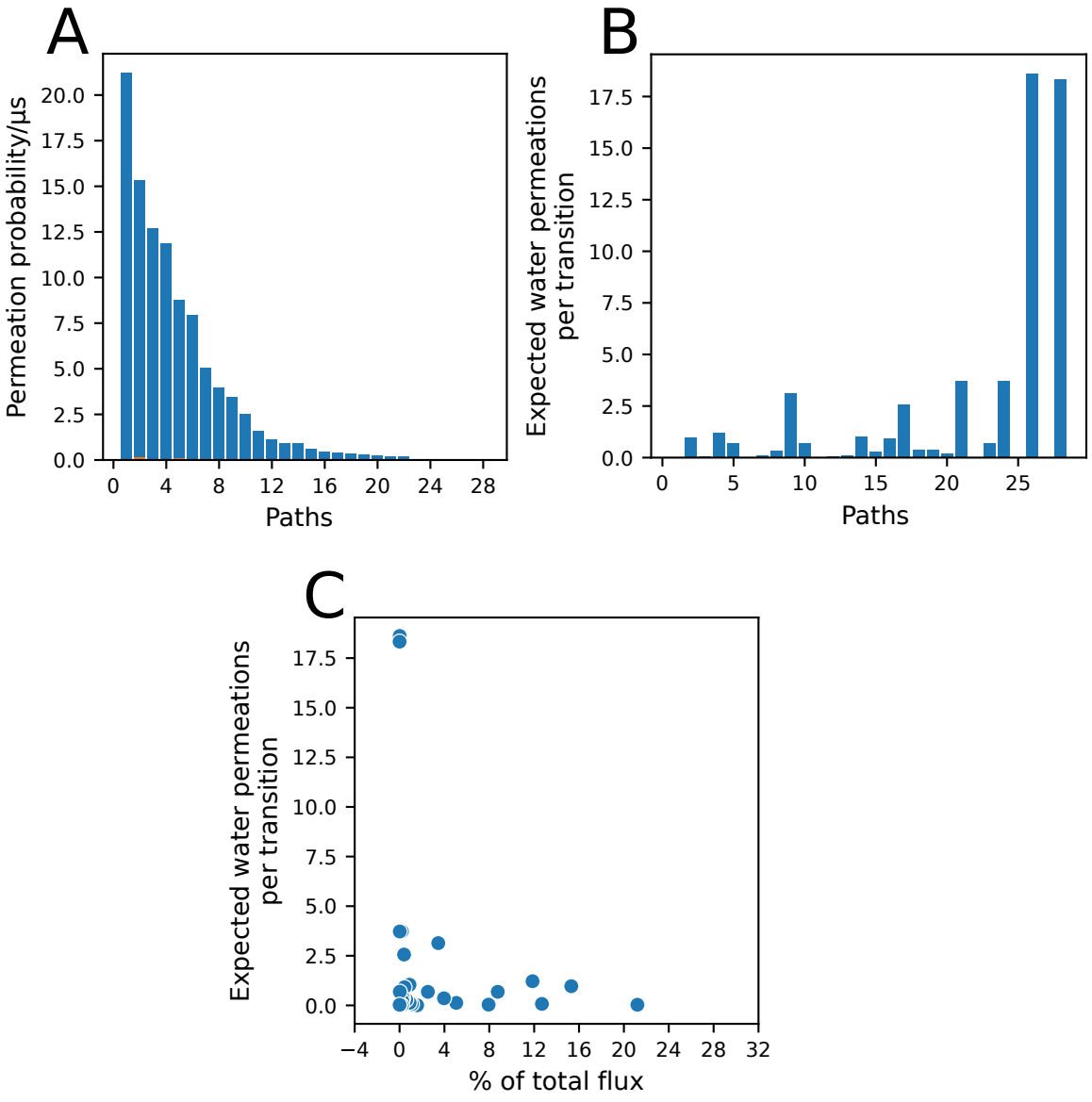

Figure 4.28: **A**: Share of the total flux from the outward-facing state to the inward-facing state, states were assigned based on unbiased simulations started from *2NWX* [57] (OFC) and *3KBC* [63] (IFC) crystal structures. **B**: Expected permeations per outward to inward-facing transition pathway. **C**: Expected permeations along with the share of total flux per transition pathway. The number of expected permeations was calculated based on the mean first passage time interpreted as a residence time for the source state and the water permeations probability of each state as shown in Figure 4.27.

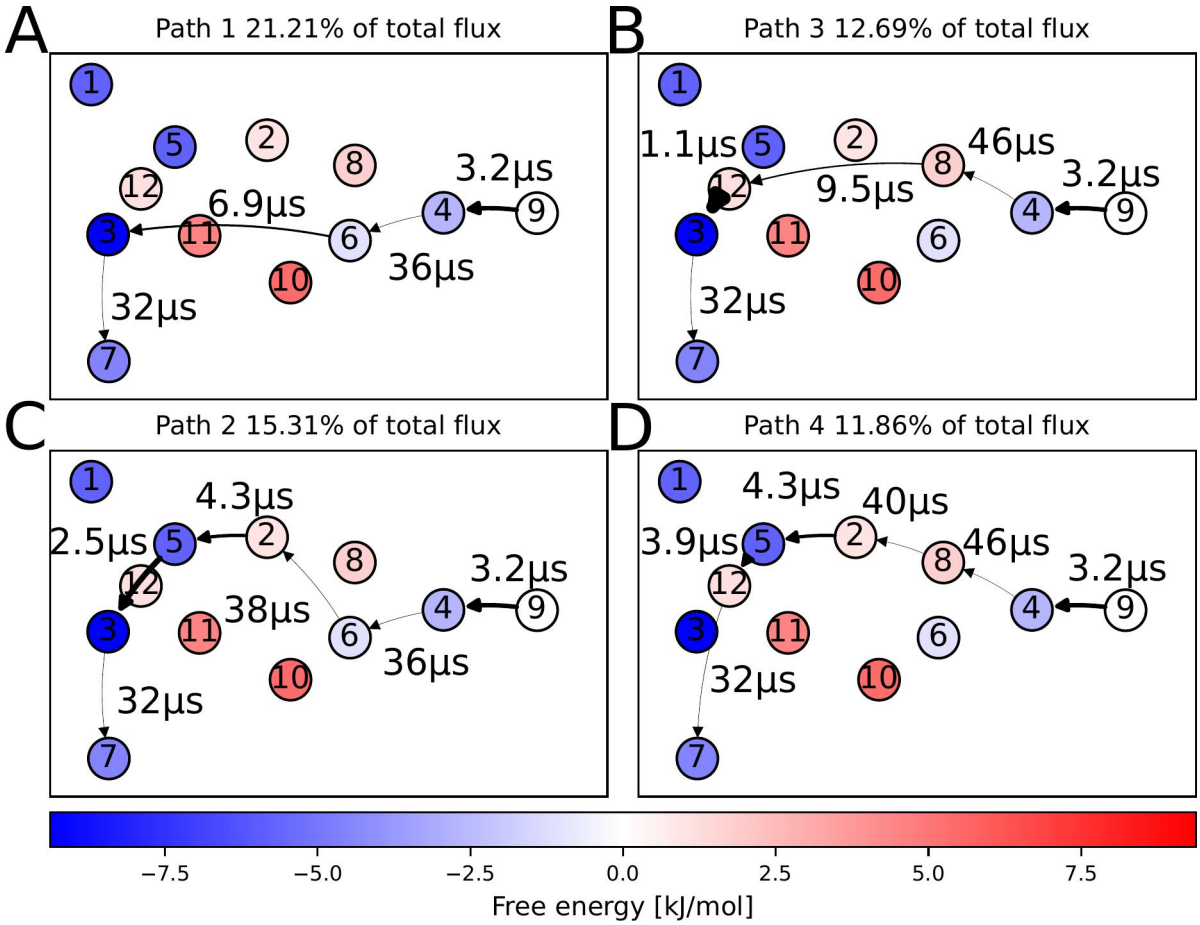

Figure 4.29: State networks for the 4 highest flux pathways for the outward to inward transition as obtained from transition path theory of a 12 state MSM. Color of each state represents the associated free energy according to the color bar below. Thickness of the arrows represents the mean first passage time between the states.

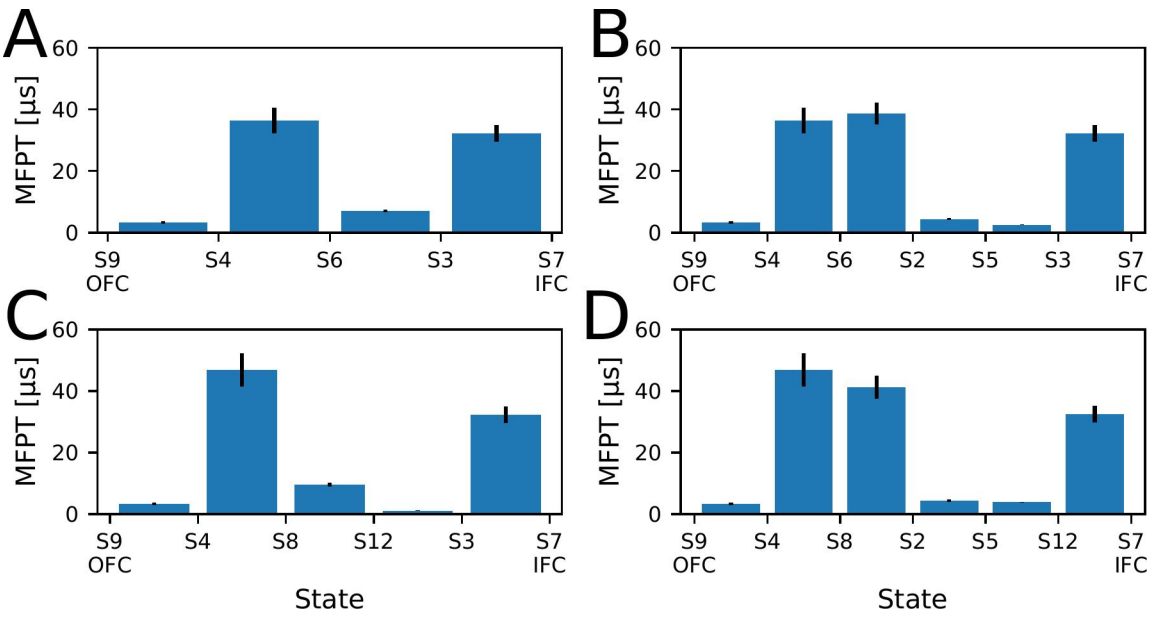

Figure 4.30: Mean first passage time (MFPT) for transitions between the states of the 4 highest flux pathways (**A**: Path 1, **B**: Path 2, **C**: Path 3, **D**: Path 4) for the outward to inward transition. MFPT was derived from a 12 state MSM build using the 12 VAMPnet states.

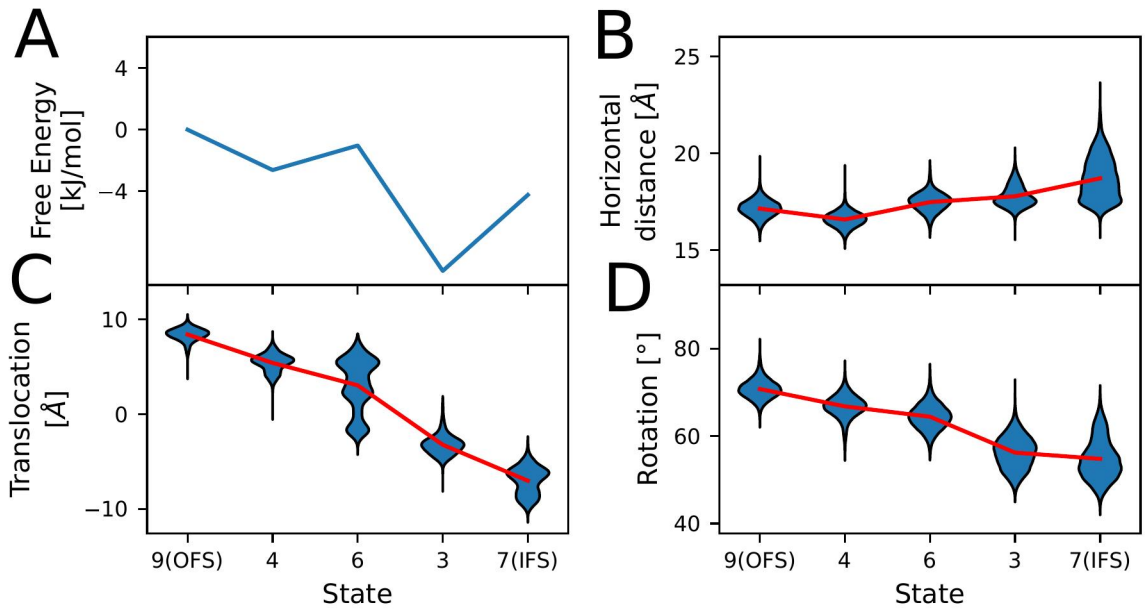

Figure 4.31: Properties along the highest flux path.

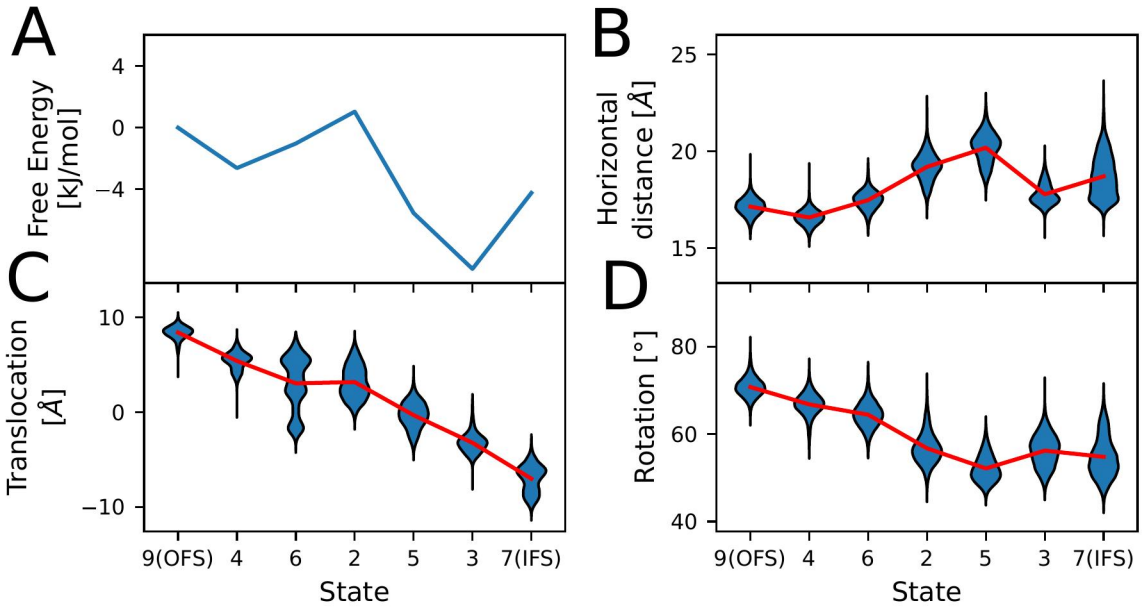

Figure 4.32: Properties along the second highest flux path.

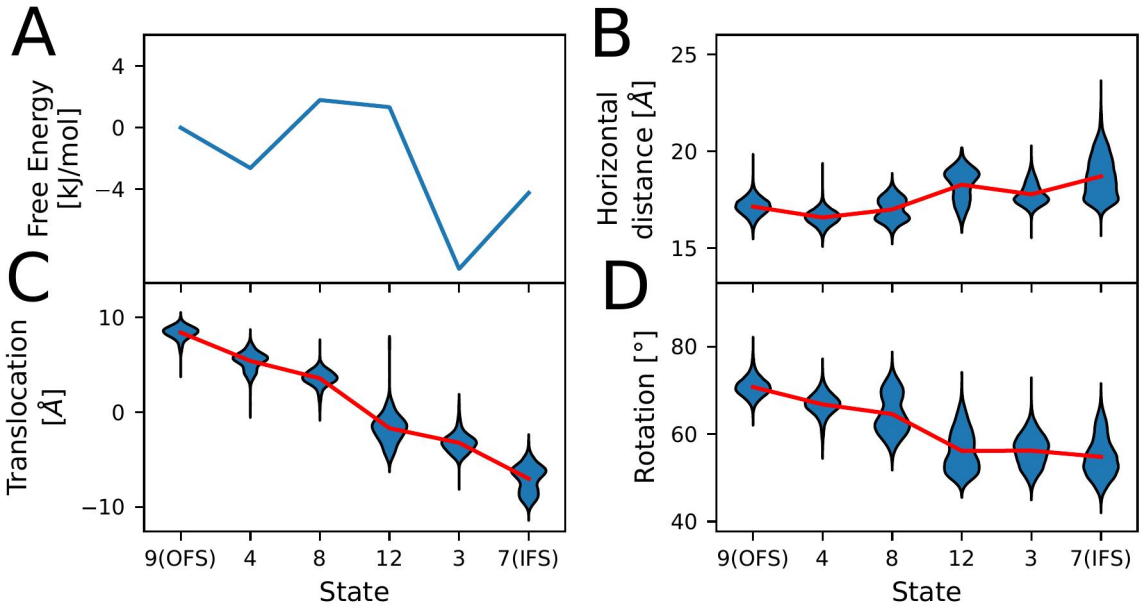

Figure 4.33: Properties along the third highest flux path.

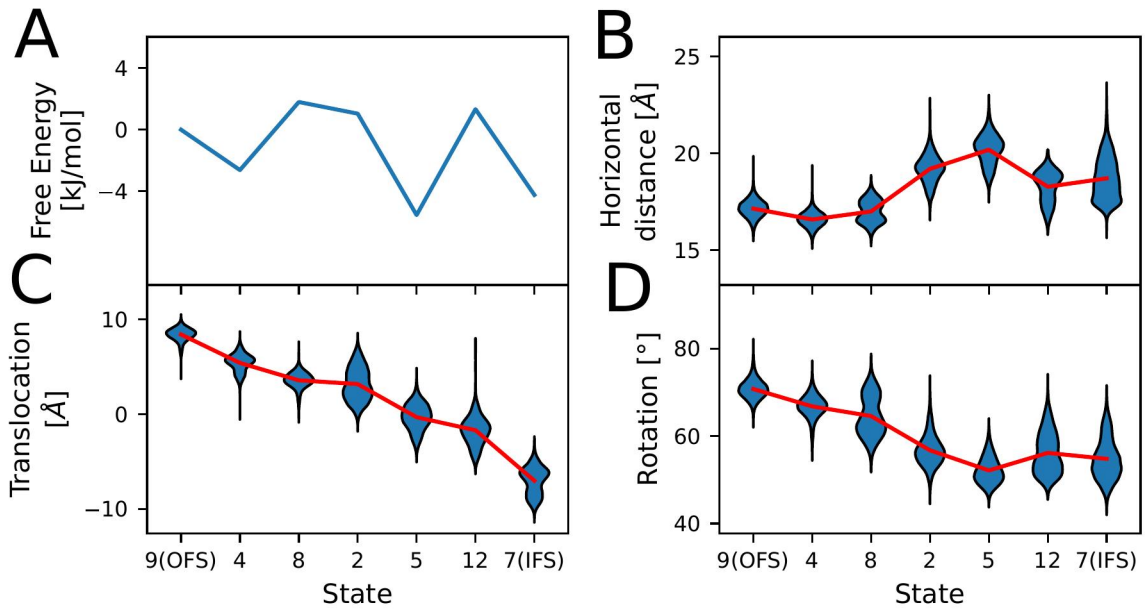

Figure 4.34: Properties along the fourth highest flux path.

Chapter 5

Discussion

The alternating access mechanism [118] postulates that the binding of a ligand molecule induces a conformational change in the transporter protein. This leads to occlusion of the binding site, towards the compartment the ligand just bound from, and opening towards the opposite compartment. Often an intermediate conformation is assumed in which the binding site is occluded from both compartments. On the molecular level, three implementations have been found which match this description of the alternating access mechanism, in all of them the protein is composed of two domains. The rocker switch [119, 120] and rocking bundle [121] mechanisms involve large lateral translation of one or both domains towards each other, which results in occlusion or opening of the binding site towards the compartments. The transported ligand is bound between the two domains and immobile during transport. The third implementation was termed elevator-like mechanism [63]. It also involves two domains and a large conformational change of one domain, but in contrast to the previous ones the bound ligand is not immobile, only binds to one domain and the conformational change features an additional vertical component. One domain remains immobile and is assumed to anchor the protein in the lipid bilayer, while the other domain, the one which also hosts the ligand-binding site, transverses the membrane in a rigid body motion.
This variant of the alternating access mechanism was first described based on the difference between two conformations observed in crystal structures of the archaebacterial Glt_{Ph} [47, 57, 63]. Over the past years, multiple intermediate conformations of this process were proposed, either by experimental methods like X-Ray crystallography and cryogenic electron microscopy [57, 63, 122, 73, 71] or by computational methods like molecular dynamics [82, 123, 83, 124]. Their location in the conformational landscape and functional relevance, however, remained largely unknown.

In EAATs, ASCTs and archaebacterial Glts accessibility to the binding site is gated by a helical hairpin, HP2, which can shield the binding site from the solvent and

hinder ligand binding and unbinding [57, 125]. Along with its function as a gate to the binding site, hairpin 2 also influences translocation dynamics. In the open state, it collides with the trimerization domain and blocks vertical movement of the transport domain [53, 54, 126, 55]. Based on the available crystal structures, it was concluded, that the two domains are stable and show no change to the internal structure, while the conformational change of the protomer as a whole is quite substantial [63, 57]. Compared to the outward-facing state (*2NWX* [57]) the transport domain is shifted by about 18 Å in the inward-facing state (*3KBC* [63]), and rotated by 37°. While in the original proposal of the alternating access mechanism it was assumed, that the two compartments are never directly connected, some proteins of the elevator-like family do feature anion channel activity [23, 24] under transport conditions [127, 128, 129]. Also in proteins with the rocking bundle or rocker-switch mechanism small mutations can lead to ion channel activity [130, 131]. The formation of this anion channel and its coupling to the conformational change, induced by ligand binding, has been recently subject to multiple studies [82, 73]. But it is still discussed controversially, since a complete description of the translocation pathway, which includes pore formation, is missing.

This work aimed to characterize the complete conformational landscape that a protomer of the elevator-like mechanism model $\mathrm{Glt}_{\mathrm{Ph}}$ must traverse to transition between the outward and inward-facing states, including anion pore formation.

5.1 Methodical motivation

Previous studies of the elevator-like mechanism were based on the interpretation of experimentally obtained structures that featured large conformational changes from which a coarse model of the transport mechanism could be derived [57, 63, 122, 73, 71]. Additional studies used experimental setups, that enabled tracking of a molecular feature [132, 65, 55, 59], usually with some uncertainty due to noise, time or experimental resolution. Further information on the molecular level was provided by computational methods [82, 133, 83, 58, 124]. Either using unbiased simulations, to study small and fast conformational changes like the binding of ligands. Or enhanced sampling methods in biased simulations to study large and slow conformational changes. While translocation itself is inaccessible to unbiased simulations, it was investigated in biased simulations using multiple enhanced sampling techniques. These methods utilize an existing hypothesis to define reaction coordinates (RCs) and evaluate protein dynamics along these. The definition of those RCs is a crucial and complicated part. This is highlighted in Grazioso et al. [124] where the opening of hairpin 2 in the outward-facing and hairpin 1 in the inward-facing states was investigated. The role of HP1 as the inward-gate has been discussed in the past, but this has been disproven experimentally [134]. This function of HP2 as the outward and inward gate was invisible in Grazioso et al. [124] due to the RCs chosen. In this case, the RCs represented the distance towards and position along a hypothetical path describing the opening of hairpin 1. In general, ill-defined RCs can lead to wrong conclusions and may just confirm what was expected.

To attenuate this bias, methodical and human, an enhanced sampling method was combined with unbiased simulations and only the unbiased data was evaluated.

5.1.1 Generating seed conformation

The accelerated weight histogram method, see Section 3.2, was used to generate intermediate conformations of the translocation process. These represent an "educated guess" of conformations a protomer might assume during translocation. Based on the general idea that the translational motion consists of a vertical and maybe also lateral movement of the transport domain the accelerated weight histogram method was used to evaluate all combinations of vertical and lateral distances between the centers of mass of both domains. The range of the vertical translation was limited to values observed in crystal structures of *2NWX* [57] (OFC, upper limit) and *3KBC* [63] (IFC, lower limit) and the lateral range was limited by values observed in the unlocked crystal structure (*4X2S* [71], upper limit) and *2NWX* [57] as well as *3KBC*

[63] (lower limit). Also, the bias introduced into the system was limited to 300 $\frac{kJ}{mol}$ or 1000 $\frac{kJ}{mol}$ to make irreversible conformational changes less likely. In comparison with enhanced sampling techniques like COM-pulling [135], essential dynamics [136, 137] or metadynamics [92, 138] AWH was straight forward to set up and did not require extensive calibration of gaussian height and width like in metadynamics, pull speed and spring force like in COM-pulling or step size in essential dynamics. This approach is reminiscent to the methodology found in [83]. They used a simple motion planning algorithm to generate possible intermediate conformation, these were clustered and a total of five intermediates were used to start unbiased simulations. In contrast to the results presented here they constructed *de novo* trimers, each protomer started in an intermediate conformation. While they did observe conformations reassembling *3V8G* [72] and hydration of the domain-domain interface, they did not observe an increased domain-domain distance or a continuous water pathway. This is most likely due to the initial bias of the motion planning algorithm, rather short MD simulations and the use of *de novo* trimers. During the short unbiased simulations the conformations were unable to diverge from the interpolated OFC-IFC transition pathway assumed by motion planing and the combination of a "naive" lipid bilayer with intermediate protomers likely caused nonphysiological protomer-lipid interactions.

In each of the AWH simulations, a single protomer transitioned multiple times between the outward and inward-facing states, exploring different pathways between the two states and multiple conformations in each of the states. Due to the AWH algorithm, the bias was very high at the beginning of the simulation and decreased over time [91]. This resulted in fast transitions within the first 10 to 20 nanoseconds of a simulation. The high bias in the beginning could have pushed protomers into nonphysiological conformations, which might be non-reversible in the timescales accessible.

5.1.2 Modelling process dynamics

Starting unbiased simulations from snapshots of biased simulations allows these to relax, given enough time, into low energy conformations and recover the physiological conformational change. To recover the low energy pathway, one could use the density of relaxed high energy snapshots along some RCs, either the same used during enhanced sampling or new ones [139, 140, 141, 142]. Such a scheme of utilizing multiple independent simulations suits today's hardware capabilities which allow running tens or hundreds of simulations with linear scaling [143, 144] while utilizing the same hardware for a single simulation scales less favorable [145, 74, 146]. But for some conformations

the time necessary to relax into a physiological state might be very long, and inaccessible in one continuous simulation which might result in multiple pathways with similar density [147]. Markov state modeling (MSM) offers a framework to evaluate multiple short and independent unbiased simulations [148], based on the assumption that a dynamic system can be separated into several states and that the probability of transitioning between states only depends on the current state, if transitions are evaluated at the right lag time [149, 150]. While MSMs do require RCs, defined by the user, this step is less critical compared to enhanced sampling methods since no bias is applied along these coordinates, and they can be changed during evaluation without any impact on the simulations. These RCs are used to cluster conformations into a set of states, ill-defined RCs can lead to ill-defined states which leads to ill-defined estimated dynamics [151].

Definition of RCs, choice of clustering algorithm and parameters, deciding on a number of states and lag time selection are tasks left to the user. Each of these steps influences the final result and the optimal parameters of the following steps, a useful MSM thus requires multiple rounds with iterative changes to the modeling parameter. But the possibility of changing RCs in hindsight allows the modeler to quickly adapt to new insight obtained during this cycle. Recently the VAMPNet [105] method was introduced, which replaced this iterative cycle with a neural network that utilizes a variational approach [110], to find an optimal transformation from the original high dimensional feature space into a low dimensional state discrimination. VAMPNets only require two user tunable parameters for the whole workflow and offer an objective scoring function for evaluation, reducing the impact of human bias.

5.2 Plausibility of generated continuous descriptions

Previously, multiple conformations were obtained using experimental methods and proposed as intermediate conformations of the translocation motion. These conformations provided some hints regarding the type of motion required.

- *2NWX* [57] and *3KBC* [63] show the transport domain about 10 Å above, respectively, below the center of the trimerization domain.
- In *4X2S* [71] (and *6WYK* [73]) the distance between transport and trimerization domain is increased perpendicular to the membrane normal.
- The transport domain features a different rotation in *2NWX* [57], *3KBC* [63] and *3V8G* [72].

But they only provide snapshots of a continuous process, without information about their position in the sequence of motion.

To obtain a continuous description of the conformational change required to switch from the outward to the inward-facing state, the enhanced sampling method "accelerated weight histogram" (AWH) was used. The conformational landscape was explored along two coordinates, **1**. the vertical offset of the transport domain above or below the center of the trimerization domain captures the conformational change observed in *2NWX* [57] vs. *3KBC* [63]. **2**. the horizontal distance between transport and trimerization domain perpendicular to the membrane normal captures the conformational change observed in *4X2S* [71]. The rotational motion, described above, was not included as a biased reaction coordinate since the AWH implementation in GROMACS did not support rotational coordinates at that time, but a rotation of the transport domain was still observed in biased as well as subsequent unbiased simulations. As described in Section 4.1, multiple continuous descriptions of the translational movement were obtained from enhanced sampling. The RMSD of whole protomers showed that the two unbiased protomers were structurally stable and did not experience instability, regardless of the position of the biased protomer, as seen in Figure 4.3. The trimerization domain of the translocating protomer was stable with respect to the corresponding crystal structure, as seen in Figure 4.3. Subtle reorganization of the transport domain was found to be caused by the opening of hairpin 2, which gates access to the binding site [57, 125], this dependency can be seen in Figure 4.4. This indicates that the bias introduced by AWH was not high enough to force the biased protomer into non-physiological conformations, shown by the internal stability of both

domains of the biased protomer. And that neither the fast and repeated transitions nor the bias caused instability of the unbiased protomers through the protomer-protomer interface of the trimerization domain.
It is assumed that an open hairpin blocks translocation due to clashes with the trimerization domain [53, 54, 126, 55], as seen in Figure 4.5. The present data seem to confirm this even for conformations featuring an increased distance between the two domains. In total, 129 complete OFC⇔IFC transition events were recorded, Figure 4.6 shows that none of the events reached the outward and inward-facing state equally well. In the best case, both states were approached with an RMSD of just below 4 Å. In comparison with a previous study, where a much simpler elastic network was used to obtain a rough estimate of intermediate conformations [83], each of the AWH simulations covered multiple forward and reverse translocations of the same protomer. The fact that a protomer can undergo an outward to inward transition and then return into the outward-facing conformation with an RMSD comparable to fluctuations observed in an unbiased simulation, adds to the credibility of the employed enhanced sampling protocol.

Another critical factor is the definition of reaction coordinates, especially their competence in describing the translocation and to differentiate between conformation with different stability. While the reaction coordinate's ability to describe the translocation is established, because both starting conformations sampled the opposite state and returned successfully, they struggled with the separation of different conformations. As seen in Figure 4.2 the intermediate area in the center of the figure shows a high structural diversity for the same reaction coordinates. Since AWH was used as an explorative technique, this does not taint the resulting ensemble, but the convergence of an energy profile might have been challenging.

5.3 A novel inward-facing open state

The conformational landscape explored by a translocating protomer can be visualized by time-independent component analysis (TICA). This also allows one to compare systems with the two neighboring protomers in the outward- (OOX) or inward-facing state (IIX). Projecting the conformations of a protomer along the first two TICA components separately for both datasets reveals a striking difference (Figure 4.15). A region along TICA component 2, which is only present in the TICA landscape of the OOX dataset. It is located above an area resembling a "three-way junction" and features multiple ligand unbinding events (Figure 4.15). Given that no considerable ligand unbinding was observed around the position of *3KBC* [63] or nearby, this new region could be considered an alternative **i**nward **o**pen **s**tate (IOS). In terms of stability it features a slightly lower energy than the IFC defined by *3KBC* [63], while the MFPT from *2NWX* [57] (OFC) to *3KBC* [63] (IFC) is 46 μs ($\pm$ 2.5 μs) it takes an average of 48 μs ($\pm$ 3.7 μs) from *2NWX* [57] to the IOS. Compared to the physiological fully-bound outward to inward transitions, the non-physiological fully-bound inward-facing or IOS to outward-facing transitions feature a mean first passage time of 345 μs ($\pm$ 34 μs), respectively, 320 μs ($\pm$ 32 μs). These transition times convert to about 20 000 transitions per second for the outward to inward transition and roughly 3000 transitions per second in the inward to outward direction. Previous studies suggested that the transition rates for $\mathrm{Glt_{Ph}}$ are in the 0.5 to 0.2 transitions per second range, these studies also inferred that the OFC and IFC states feature high dwell times and ligand binding and unbinding to dominate transition rates [65, 152, 71]. While the observation of ligand unbinding is an unexpected and interesting property of this region, it counteracts the analysis of the data using Markov models. A Markov model demands the underlying data to be "Markovian", it should be memoryless and the probability of visiting the next state X_{t+1} should only depend on the current state X_t. Unfortunately, it was reported that the dynamics of hairpin 2 are altered by ligand binding. In the absence of glutamate [126] and presence of Na1 and Na3, the open hairpin state is stabilized, which blocks translocation [53]. During all simulations, a restraint was used to keep one sodium ion bound to the Na2 site [153, 154, 155, 156, 48]. In unbiased simulations started from the *2NWX* [57] and *3KBC* [63] crystal structures, this restraint ensured a closed hairpin and properly bound ligands. Due to this restraint, the hairpin cannot adopt a fully open conformation. It is currently unclear how this affects the protomers ability to exit the IOS, and return to the junction region. If these protomers should be stuck in the IOS, this would lead to artificial low energy in this area since simulations could enter it easily, but it is impossible for them

to exit. In total, only 16 out of the 623 simulations in the OOX dataset feature a distance greater than 15 Å between the bound amino acid and its binding site and can be considered unbound. Furthermore, no correlation between hairpin opening and ligand unbinding was observed, as seen in Figure 4.23. The fact that this region only emerged in the OOX dataset makes one question its plausibility. Although it was visited after a couple of hundred nanoseconds during unbiased simulations and not during enhanced sampling simulations, where the added bias could have pushed the protomer into unfeasible high energy regions. After starting additional, unbiased, IIX simulation in the junction region, a protrusion began to form which might make this region accessible in the IIX dataset, too. Additionally, more OOX simulations were started in the junction region after all simulations that visited the IOS previously were excluded from the dataset, to confirm the reproducibility of that region, like in the IIX dataset a protrusion was visible.

5.4 The elevator-like mechanism is a multi-stage process

The elevator-like implementation [63, 47] of the alternating access mechanism has been characterized as a single motion with two distinct components, a vertical and a rotational one [63]. A horizontal component has been discussed critically [71, 157] in the past, but was recently revitalized [158, 134, 159]. While the outward and inward-facing states show long dwell times [65] and ligand binding has been postulated as a multi-stage induced fit [160] or conformational selection mechanism [126], it remained unknown, if the conformational change during translocation is a single motion or a process with multiple intermediate steps. Previous studies on Glt_{Ph} suggested the presence of at least one intermediate step [161, 132, 65, 162] and multiple probable intermediates were crystallized or proposed by *in silico* methods [72, 71, 73, 82], but their position in the translocation sequence remained elusive. Single-molecule fluorescence resonance energy transfer studies found three distinguishable states for Glt_{Ph} [64, 71]. Direct visualization of translocating protomers using high-speed atomic force microscopy was able to distinguish between two states [65]. A study of the elevator-like nucleoside transporter CNT_{NW} crystallized multiple intermediate conformations, which they clustered into three groups [161]. Two of these intermediates were close to the outward, respectively, inward-facing state while one was halfway in between these two. A similar study on Glt_{Tk} found four different conformations, although some represented the same state but in a ligand-bound and a ligand unbound conformation [56].

The notion of a multi-stage process for the translocation of Glt_{Ph} is supported by the energy profiles obtained from OOX and IIX simulations. The energy profiles along the first two TICA components indicate between one and two intermediate conformations for the outward $\Leftrightarrow$ inward translocation. The first is located in the junction region between or nearby the *4X2S* [71] and *6WYK* [73] structures, in OOX simulations the alternative inward open state is accessible from this region. Also, it is adjacent to the permeable region in both datasets, as seen in Figure 4.25. It is unclear, if protomers assume permeable conformations during the outward-facing to junction region transition or if protomers might diffuse from the junction region into the permeable region. The second possible intermediate is represented by a local energy minimum nearby the *3V8G* [72] structure. In the OOX energy profile, this minimum is separated from the outward-facing minima, while no such barrier is visible in the IIX energy profile. The highest barrier in both energy profiles is found in between the two possible intermediates just described, nearby the position of the *ChC* [82] structure.

The energy profiles also indicate that, for the outward-facing state to junction state transition, the first TICA component is sufficient, but for the junction state to inward-facing state transition the second TICA component is vital. Also, the junction state to IOS transition is dominated by the second TICA component.

The MSM build using the 12 states identified by VAMPnet in the OOX dataset was used to extract transition pathways using transition path theory (TPT) [163, 164, 165] from the outward-facing state into the inward-facing state. A total of 28 pathways were found, but four pathways represented 54% of the total transitions between these two states, for the sake of brevity only those four will be discussed in detail. Figures 4.31, 4.32, 4.33 and 4.34 show that the translational-rotational components are also found in these four pathways. When comparing the curves for rotational and vertical movement, one may notice a similar pattern in those paths, a linear decrease followed by a steep decrease, followed again by a linear decrease. Counterintuitively, this steep change of the vertical distance and simultaneous rotation does not go along with a steep decrease in stability, on the contrary, Figures 4.32 and 4.33 suggest that the states after rotation in these pathways are barely as favorable as those prior to rotation.

During translocation, the protomer visits at least five different states, which were separated by VAMPNet. From the outward-facing $S9$, the protomer always transitions into $S4$, which features an RMSD of 2.4 Å to *2NWX* [57] and an RMSD of 0.9 Å towards the proposed "intermediate outward-facing" *3V8G* [72] structure. For the inward-facing state two close intermediate states are found, $S3$ and $S12$, they feature an RMSD of 2.3 Å, respectively 1.9 Å towards *3KBC* [63] and in both the *6WYK* [73] crystal structure represents the closest match. In the third-highest flux path both, $S3$ and $S12$, are visited, indicating that they might be interchangeable. Definition of the "halfway in-between" intermediates is a bit fuzzy, four states ($S2$, $S5$, $S6$ and $S8$) are visited in the top four pathways. Notably, these four intermediates feature a small probability to enter a water-permeable conformation, as shown in Figure 4.27. According to the MSM $S5$ should have a slight advantage, as it is the most stable one and was assigned a positive energy (Figure 4.18). In terms of their structural similarity towards *2NWX* [57] and *3KBC* [63] as well as their location along the TICA components, they can be considered "halfway in-between" the outward and inward-facing states. Visually, they are similar and their main difference is the rotation of the transport domain. This might render them hard to distinguish experimentally. The three states observed in FRET experiments [64, 71] might correspond to **1** the outward-facing and $S4$ state **2** the three "halfway in-between" states, $S2$, $S5$, $S6$, $S8$ and **3** the inward-facing state plus $S3$ and $S12$.

The energy profiles, the linear-steep-linear pattern of the vertical translation-rotation

motion and the three to four intermediate states along the outward to inward pathways indicate that the elevator-like mechanism is not a single linear motion but a multi-stage process with distinct intermediates.

5.5 Membrane interactions influence protomer dynamics

The current, generally accepted concept of elevator-like glutamate transporters postulates that protomers in the trimer do not interact, and their conformation has no influence on the dynamics of their neighbors [65, 166, 167, 64, 66], while the lipid bilayer is assumed to influence transport dynamics [80, 66, 168]. This is supported by the observation that there is no direct contact between one protomers transport domain and another protomers transport or trimerization domain, due to the lipid bilayer separating the subunits as seen in Figure 2.2.

Since data for the transformation of symmetrical OOO and III trimers into asymmetrical trimer configurations OOI and IIO was generated, it was possible to compare the dynamics of the translocating protomer. Analyzing both datasets using TICA with the same components, like done in the results section, shows that different regions of the conformational landscape are explored along the first two TICA components (Figure 4.15). When comparing the energy profile and the projections of published crystal structures like in Figure 4.15, it can be seen that most experimental structures are situated nearby a local minimum, but the exact locations of these minima are shifted between the datasets. While *3KBC* [63] is on the edge of the minimum in the OOX dataset, its location corresponds to the deepest point of the minimum in the IIX dataset. This shift in conformational preference is especially interesting since it might confirm that, *3KBC* [63] is a good representation of a trimer in the inward-facing state, but an inward-facing protomer in an asymmetric trimer with two protomers in the outward-facing state is likely to settle in a different conformation. In both landscapes, a local energy minimum is visible at the region reassembling a "three-way junction", the minimum in the IIX dataset corresponds to the unlocked intermediate (*4X2S* [71]) while in the OOX dataset no known structure is nearby. Surprisingly, *2NWX* [57], which is believed to represent the outward-facing state, is not close to any minima in the OOX or IIX datasets. At first sight, this might contradict the conformational stability observed in simulations started from the *2NWX* [57] crystal structure, given the present energy surface, one would expect a quick transition from *2NWX* [57] towards *3V8G* [72]. When using the transition probabilities from a Markov state model, one can compute the mean first passage time (MFPT) from a state representing *2NWX* [57] (S9) to a state representing *3V8G* [72] (S4). The mean first passage time [169] for the 2NWX $\rightarrow$ 3V8G transition is 2.98 μs, well beyond the longest continuous simulation conducted during this project. Furthermore, applying TICA on the Cα-Cα of both datasets separately yields significant different compo-

nents, which implies that the slowest correlated motions represented in these datasets are different. This hints at an essential difference between the investigated OOX and IIX systems. Since direct interactions of a transport domain with neighboring protomers are absent in all simulations conducted, the variation is most likely caused by differences in the lipid bilayer. Recent publications [66, 56] suggested curvature of the lipid bilayer depending on the protomer conformation, outward-facing protomers cause an upward curvature while inward-facing conformations lead to a downward curvature. Both publications concluded that the bilayer curvature does not extend far enough to cause a difference in the lipid environment close to a neighboring protomer, although none of them explicitly investigated this. The simulation box (X 145 Å Y 145 Å Z 110 Å), in the unbiased simulations presented here, is too small to obtain a bulk bilayer height which could be used to compare the present results to the published ones. Additionally, the small box size may have led to an amplified influence of the protomers on the lipid membrane. The membrane curvature described in Zhou et al. [66] is reported to extend up to 100 Å. In AWH and unbiased simulations each trimer is separated by about 60 Å from its PBC mirror image, the membrane curvature of one protomer thus might reach another protomer of the same trimer in the simulations presented here. To investigate differences in the lipid bilayer between both systems, lipid density maps were compiled from frames in the same simulations which were clustered together, the datasets were clustered into 400 states along the first two TICA components. These two TICA components were able to better separate different conformations in a low dimensional space than the hand-crafted reaction coordinates used during enhanced sampling. In the next step, cross-correlation was computed between density maps of the same dataset, OOX-OOX and IIX-IIX, as well as between simulations of both datasets, OOX-IIX. The correlation between the density maps, as depicted in Figure 4.12A, shows that density maps of simulations from the same dataset feature high similarity, but a low similarity, if comparing simulations between the datasets, although the translocating protomer is in a similar conformation. Inspecting these density maps of lipids around the transitioning protomer reveals differences of the lipid bilayer which are visible by eye. In panels B and C of Figure 4.12 the difference between lipid density from OOX and IIX simulations for a representative cluster is shown. While the orange surface on the left of each panel is not in contact with the translocating protomer, there is lipid density on the right, partly occupying the crevice between the transport and trimerization domain. Lipid density in this region has been observed previously in experimental structures [168, 56, 132] of the inward and outward-facing state, and was suggested to modulate dynamics of the whole transport domain and hairpin 2 in the outward-facing state. This modu-

lation might facilitate translocation by favoring a closed hairpin 2 or by disrupting domain-domain interactions [168, 71] allowing the transport domain to move more easily, or act as a steric hindrance slowing translocation. Lipids entering the crevice are observed in some OOX simulations but are prevalent in IIX simulations, where it was also observed for neighboring protomers. In the outward-facing state of both datasets, lipid density in the crevice was lower than in the inward-facing state. These lipids show low mobility and are not likely to be displaced during translocation, as suggested in [168], but stay close to the trimerization domain and do not move with the transport domain. One electrophysiology study of wild type EAAT4 and two mutants suggested cooperativity between protomers regarding opening of the anion channel [170]. This would require translocation of one protomer to alter the membrane in a way that allows another protomers transport domain to move away from the trimerization domain. Indeed, the energy profile along the two TICA components shows that the two datasets are shifted along the second component (Figure 4.15). Also, such cooperativity would offer an explanation why four times more permeations were found in OOX simulations compared to IIX simulations and why Figure 4.25C and D show that the transport domain seems to be more likely to move further away from the trimerization domain in OOX simulations. But given the current data, it is not possible to differentiate between altered dynamics due to lipid membrane-mediated subunit cooperativity and differences in lipid-protomer interactions due to insufficient equilibration of the starting structures. A biased protomer in an OOX trimer might have visited the IFC multiple times during enhanced sampling without a lipid entering the crevice. It is unknown if this crevice-lipid-free protomer is a good representation of the outward-facing state or some close to outward intermediate. Furthermore, it is unknown, if entering of lipids into the crevice is facilitated by neighboring protomers in the inward-facing state or lipids enter the crevice independently of the total trimer conformation, although current data suggests that they are more likely to enter the crevice of a protomer in the inward-facing state. While this is the most pronounced and most consistent difference between density maps of OOX and IIX simulations, it remains unclear, if it is solely responsible for the different dynamics observed in OOX and IIX trimers.

5.6 Anion permeation is not an obligatory step of glutamate translocation

The glutamate [171, 128] or cation [172, 173, 55] gated anion channel, which is not thermodynamically coupled to glutamate transport, is a curiosity found in all mammalian EAATs and archaebacterial glutamate transporters. Although its physiological role has been discussed multiple times, its importance to the cellular function is still largely unknown [174, 175, 176, 177, 178]. Some members of the EAAT family are considered relevant mainly due to their chloride conductance and less due to the transport of glutamate [23, 179]. Especially the retina located EAAT5 features a low glutamate capacity and was proposed to act like a "slow-gated glutamate receptor" [180, 181]. Studies of glial cells suggest that chloride conductance of EAAT1 and EAAT2 influences their internal chloride concentrations [182, 176] and mutations in EAAT1, which increases its channel activity [183], leads to apoptosis of Bergmann glial cells during brain development [177].

A first prediction of a chloride conductive structure was published by Machtens et al. 2015 [82], and was obtained *in silico* using computational electrophysiology and validated by an *in vitro* combination of electrophysiology studies and tryptophan quenching of derived mutants. A second structure was published in 2021 [73], this time obtained via cryo-electron microscopy of a cross-linked Glt_{Ph} variant. While no chloride density was observed, the presence of a continuous water pathway, formed in MD simulations under conditions similar to [82], lead to the assumption that it was chloride permeable, too. While continuous water density is a probable cause for ion channel formation [184], only observed ion density is a sufficient proof, but this is often only obtainable in biased simulations [82]. To screen for, presumable, channel conformations in unbiased simulations of the OOX and IIX dataset, the method described in section 3.3.6 was used to detect completed permeation events. Compared to a continuous density of water molecules, this offers the advantage that density might only appear continuous due to the size of histogram bins used during density calculations. In simulations of an OOX trimer, 489.224 completed water permeation events were found, in contrast to 125.300 permeation events in simulations of IIX trimers. Compared to about half a million water permeations, only 41 chloride permeations in the OOX dataset were found, and none in any IIX simulation. In the landscape formed along the first two TICA components, water-permeable conformations form a continuous region with lower permeability at edges and higher permeability at the center, as seen in Figure 4.25 and 4.27. In the TICA projection, water-permeable conformations are located between the junction and the minimum close to the outward-facing

conformation, roughly halfway between the outward and inward-facing states. While the water-permeable region is shifted along TICA component 2 in the OOX and IIX dataset, the position along the first component stays the same. Projection of conformations along the vertical component of the translocation and the horizontal distance between the two domains shows that a horizontal distance of above 32 Å between the domains favors water permeability. As seen in section 4.2.7, water permeation was confirmed for a subset of conformations in states $S2$ and $S5$, Figure 4.27A shows that states $S6$ and $S8$ feature a very small probability of observing permeations when entering these states. Stationary distribution (Figure 4.18) suggests that state $S2$ represents rather unfavorable conformations and a protomer is unlikely to stay in this state for long, state $S5$ on the other hand seems to be slightly more stable. Transition path theory analysis of the 12 state VAMPNet Markov state model shows that only 25% of the total is flux directed through either state $S2$, $S5$ or both. This suggests that states in which water permeation was observed are rarely visited and most of the OFC $\leftrightarrow$ IFC transitions are unlikely to feature channel formation or permeations, as seen in Figure 4.28B. This low probability of encountering pore formation and permeation seems to be in agreement with experimental results, where an absolute open probability of 0.06% was determined for EAAT2 [185]. It should not be ignored that these total open probabilities were acquired by electrophysiology and report on the permeability of charged ions, while the numbers reported above are for water permeation and thus are expected to be higher. Visual inspection of some water-permeable structures suggests that water molecules can permeate not only through the pore described previously [82, 73], but also close by or through hairpin 2. It is unknown, if charged chloride ions can occupy the same space or might be blocked from proceeding by the positive charges of the three bound sodium ions or repelled by the bound amino acid. Interestingly, glutamate transport by EAAT1 was shown to induce swelling of oocytes [186, 187] due to water transport. This water transport was split into an active and a passive component, and it was assumed that the anion channel is not the only pathway for water to traverse the transporter.

The location of the water-permeable regions in the conformational landscape suggests that it is only accessible halfway through translocation. These conformations are likely inaccessible to an outward-facing protomer without ligands bound, since in the absence of glutamate the conformation of hairpin 2 disfavors translocation [53]. This might explain the glutamate dependency of anion conductance observed [188], due to the lack of simulations featuring apo-protomers, it remains unknown how permeation is inhibited in the second half of the transport cycle during apo inward to outward transition. These findings offer insight into the interplay of glutamate transport and anion

channel formation and show that it is not a mandatory step during translocation and is likely governed by additional dependencies which have not yet been characterized.

Chapter 6

Conclusion

The elevator-like mechanism is an odd and interesting implementation of the alternating access mechanism. The large conformational change, which drags the transported ligand through the membrane combined with a thermodynamically uncoupled anion channel and presumable strong protein-lipid interactions, justifies the interest they have been met with during the past three decades.

Here, I used enhanced sampling simulations of fully bound protomers to obtain multiple "educated guesses" of possible translocation pathways from outward to inward-facing state and vice versa. These simulations were informed by rough descriptions of the translocation pathway obtained from published structures of potential translocation intermediates [71, 72, 73] and proposed end states [63, 57]. Since these structures were not easily compiled into a unifying description of the complete translational motion, unbiased simulations were started from snapshots of the pathways obtained from enhanced sampling. With the objective to obtain an unprejudiced description of the translocation, within certain limits, which covers the complete conformational landscape, including formation of the anion pore. To investigate possible differences in the translocation process due to the configuration of the trimer, two simulation systems were used. One featuring two of the three protomers in the outward-facing state, termed OOX, and one with two protomers in the inward-facing state, termed IIX. Striking differences were found between these two systems. They do feature different dynamics, explore different conformations, and feature different conformational preferences in those regions both systems explored. The cause of these differences could not be determined unambiguously, but strong evidence was presented pointing towards lipid bilayer mediated interactions. Lipid density between the two domains was visually identified as differentiating, but it remains unknown if it is solely responsible for the different dynamics. Furthermore, it remains unknown if different trimer configurations favor different protomer-lipid interactions.

The dynamics and conformations contained in the unbiased simulations offer a complete description of the physiological outward to inward transition of a fully bound Glt_{Ph} protomer. This description on the atomistic level allowed identification of multiple steps of the translocation, including a novel inward-facing open state and multiple water-permeable intermediate states. The elevator-like mechanism, as implemented by Glt_{Ph}, was characterized as a multistep process with non-obligatory anion pore formation. Formation of the anion pore might be favored by a trimer configuration with two protomers in the outward-facing state. This is suggested by the ratio of permeation events found in the two different systems, with about four times as many permeations observed in OOX simulations compared to IIX simulations. The location of these water-permeable configurations along possible pathways from the outward-facing state into an inward-facing state offers an explanation for the dependence of anion conductance on glutamate transport. While the interplay between the membrane and the probability of anion pore formation offers a possible explanation why this dependence is thermodynamically uncoupled.

Chapter 7

Outlook

This work opened new questions regarding cooperativity between protomers, formation of the anion channel and the interplay between the lipid bilayer and protomer dynamics. Further analysis of the generated data might provide a more detailed explanation of the differences in lipid density observed between OOX and IIX systems and how these differences affect protomer-bilayer interactions and conformational preferences of a translocating protomer. But the fully-bound outward to inward transition only represents half of the transport cycle, a comparable dataset of protomers in the ligand-less state would be highly desirable. These protomers might show different dynamics, and these new datasets could clarify if the physiological ligand-less inward to outward transition can trigger anion pore formation. A comparison between Glt_{Ph} protomers and those of an EAAT variant in the ligand-less and potassium bound state might provide interesting details about potassium dependency of the mammalian variants. Simulations employing computational electrophysiology are needed to verify that **(1)** chloride ions can occupy the same positions as permeating water molecules, and **(2)** that water permeability found here corresponds to anion conductance. Simulations with a significantly bigger simulation box, with a minimum distance between trimers of 200 Å, might be necessary to properly investigate possible cooperativity between protomers regarding formation of the anion channel. Last but not least, additional simulations are needed to untangle the effect of lipids entering the crevice and trimer configuration, in the current data these two features are highly correlated. But it is unknown, if this is due to altered bilayer dynamics in OOX and IIX trimers, or due to the inability of lipids to enter the crevice in the outward-facing state.

This data would allow future researchers to unify the ligand binding and unbinding processes with those of the forward and reverse translocation and enable them to finally conclude the description of the complete transport cycle.

Bibliography

[1] M. Ankarcrona et al. "Glutamate-Induced Neuronal Death: A Succession of Necrosis or Apoptosis Depending on Mitochondrial Function". In: *Neuron* 15.4 (Oct. 1995), pp. 961–973.

[2] D. D. Yang et al. "Absence of Excitotoxicity-Induced Apoptosis in the Hippocampus of Mice Lacking the Jnk3 Gene". In: *Nature* 389.6653 (Oct. 1997), pp. 865–870.

[3] B. Tuk. "Overstimulation of the Inhibitory Nervous System Plays a Role in the Pathogenesis of Neuromuscular and Neurological Diseases: A Novel Hypothesis". In: *F1000Research* 5 (Aug. 2016).

[4] M. A. Herman and C. E. Jahr. "Extracellular Glutamate Concentration in Hippocampal Slice". In: *Journal of Neuroscience* 27.36 (Sept. 2007), pp. 9736–9741.

[5] M. A. Herman, B. Nahir, and C. E. Jahr. "Distribution of Extracellular Glutamate in the Neuropil of Hippocampus". In: *PLOS ONE* 6.11 (Nov. 2011), e26501.

[6] N. Riveros et al. "Glutamate in Rat Brain Cortex Synaptic Vesicles: Influence of the Vesicle Isolation Procedure". In: *Brain Research* 386.1-2 (Oct. 1986), pp. 405–408.

[7] P. M. Burger et al. "Synaptic Vesicles Immunoisolated from Rat Cerebral Cortex Contain High Levels of Glutamate". In: *Neuron* 3.6 (Dec. 1989), pp. 715–720.

[8] Y. Wang et al. "Counting the Number of Glutamate Molecules in Single Synaptic Vesicles". In: *Journal of the American Chemical Society* 141.44 (Nov. 2019), pp. 17507–17511.

[9] J. D. Clements et al. "The Time Course of Glutamate in the Synaptic Cleft". In: *Science* 258.5087 (Nov. 1992), pp. 1498–1501.

[10] J. A. Dzubay and C. E. Jahr. "The Concentration of Synaptically Released Glutamate Outside of the Climbing Fiber–Purkinje Cell Synaptic Cleft". In: *The Journal of Neuroscience* 19.13 (July 1999), pp. 5265–5274.

[11] E. B. Malarkey and V. Parpura. "Mechanisms of Glutamate Release from Astrocytes". In: *Neurochemistry international* 52.1-2 (Jan. 2008), pp. 142–154.

[12] S. Takamori et al. "Identification of a Vesicular Glutamate Transporter That Defines a Glutamatergic Phenotype in Neurons". In: *Nature* 407.6801 (Sept. 2000), pp. 189–194.

[13] S. Takamori. "VGLUTs: 'exciting' Times for Glutamatergic Research?" In: *Neuroscience Research* 55.4 (Aug. 2006), pp. 343–351.

[14] S. Takamori et al. "Molecular Anatomy of a Trafficking Organelle". In: *Cell* 127.4 (Nov. 2006), pp. 831–846.

[15] T. M. Tzschentke. "Glutamatergic Mechanisms in Different Disease States: Overview and Therapeutical Implications – an Introduction". In: *Amino Acids* 23.1-3 (2002), pp. 147–152.

[16] R. Dingledine et al. "The Glutamate Receptor Ion Channels". In: *Pharmacological Reviews* 51.1 (Mar. 1999), pp. 7–61.

[17] A. Ambrosini et al. "Metabotropic Glutamate Receptors Negatively Coupled to Adenylate Cyclase Inhibit N-methyl-D-aspartate Receptor Activity and Prevent Neurotoxicity in Mesencephalic Neurons in Vitro". In: *Molecular Pharmacology* 47.5 (May 1995), pp. 1057–1064.

[18] P. M. Lea et al. "Neuronal and Glial mGluR5 Modulation Prevents Stretch-Induced Enhancement of NMDA Receptor Current". In: *Pharmacology Biochemistry and Behavior*. Metabotropic Glutamate Receptors 73.2 (Sept. 2002), pp. 287–298.

[19] V. A. Skeberdis et al. "mGluR1-mediated Potentiation of NMDA Receptors Involves a Rise in Intracellular Calcium and Activation of Protein Kinase C". In: *Neuropharmacology* 40.7 (June 2001), pp. 856–865.

[20] R. J. Vandenberg and R. M. Ryan. "Mechanisms of Glutamate Transport". In: *Physiological Reviews* (Oct. 2013).

[21] P. Marcaggi and D. Attwell. "Role of Glial Amino Acid Transporters in Synaptic Transmission and Brain Energetics". In: *Glia* 47.3 (2004), pp. 217–225.

[22] S. F. Traynelis et al. “Glutamate Receptor Ion Channels: Structure, Regulation, and Function”. In: *Pharmacological Reviews* 62.3 (Sept. 2010). Ed. by D. Sibley, pp. 405–496.

[23] W. A. Fairman et al. “An Excitatory Amino-Acid Transporter with Properties of a Ligand-Gated Chloride Channel”. In: *Nature* 375.6532 (June 1995), pp. 599–603.

[24] J. I. Wadiche, S. G. Amara, and M. P. Kavanaugh. “Ion Fluxes Associated with Excitatory Amino Acid Transport”. In: *Neuron* 15.3 (Sept. 1995), pp. 721–728.

[25] H. P. Larsson et al. “Noise Analysis of the Glutamate-Activated Current in Photoreceptors”. In: *Biophysical Journal* 70.2 (Feb. 1996), pp. 733–742.

[26] Ø. Haugeto et al. “Brain Glutamate Transporter Proteins Form Homomultimers *”. In: *Journal of Biological Chemistry* 271.44 (Nov. 1996), pp. 27715–27722.

[27] P. Rao et al. “Designing Novel Nanoformulations Targeting Glutamate Transporter Excitatory Amino Acid Transporter 2: Implications in Treating Drug Addiction”. In: *Journal of personalized nanomedicine* 1.1 (2015), pp. 3–9.

[28] T. M. DeSilva et al. “Expression of EAAT2 in Neurons and Protoplasmic Astrocytes during Human Cortical Development”. In: *The Journal of comparative neurology* 520.17 (Dec. 2012), pp. 3912–3932.

[29] C. M. Diaz et al. “EAAT1 and D-serine Expression Are Early Features of Human Retinal Development”. In: *Experimental Eye Research* 84.5 (May 2007), pp. 876–885.

[30] C. Mim et al. “The Glutamate Transporter Subtypes EAAT4 and EAATs 1-3 Transport Glutamate with Dramatically Different Kinetics and Voltage Dependence but Share a Common Uptake Mechanism”. In: *The Journal of General Physiology* 126.6 (Dec. 2005), pp. 571–589.

[31] S. D. Watts et al. “Cysteine Transport through Excitatory Amino Acid Transporter 3 (EAAT3)”. In: *PloS One* 9.10 (2014), e109245.

[32] D. Y. Tse, I. Chung, and S. M. Wu. “Possible Roles of Glutamate Transporter EAAT5 in Mouse Cone Depolarizing Bipolar Cell Light Responses”. In: *Vision Research* 103 (Oct. 2014), pp. 63–74.

[33] P. Mookherjee et al. “GLT-1 Loss Accelerates Cognitive Deficit Onset in an Alzheimer’s Disease Animal Model”. In: *Journal of Alzheimer’s Disease* 26.3 (2011), pp. 447–455.

[34] T. Chotibut et al. “Ceftriaxone Increases Glutamate Uptake and Reduces Striatal Tyrosine Hydroxylase Loss in 6-OHDA Parkinson’s Model”. In: *Molecular neurobiology* 49.3 (June 2014), pp. 1282–1292.

[35] K. Aoyama et al. “Oxidative Stress on EAAC1 Is Involved in MPTP-induced Glutathione Depletion and Motor Dysfunction”. In: *The European Journal of Neuroscience* 27.1 (Jan. 2008), pp. 20–30.

[36] S. Poletti et al. “Glutamate EAAT1 Transporter Genetic Variants Influence Cognitive Deficits in Bipolar Disorder”. In: *Psychiatry Research* 226.1 (Mar. 2015), pp. 407–408.

[37] P. V. Choudary et al. “Altered Cortical Glutamatergic and GABAergic Signal Transmission with Glial Involvement in Depression”. In: *Proceedings of the National Academy of Sciences of the United States of America* 102.43 (Oct. 2005), pp. 15653–15658.

[38] R. Bernard et al. “Altered Expression of Glutamate Signaling, Growth Factor and Glia Genes in the Locus Coeruleus of Patients with Major Depression”. In: *Molecular psychiatry* 16.6 (June 2011), pp. 634–646.

[39] A. Medina et al. “Glutamate Transporters: A Key Piece in the Glutamate Puzzle of Major Depressive Disorder”. In: *Journal of Psychiatric Research* 47.9 (Sept. 2013), pp. 1150–1156.

[40] R. A. Linker et al. “Fumaric Acid Esters Exert Neuroprotective Effects in Neuroinflammation via Activation of the Nrf2 Antioxidant Pathway”. In: *Brain: A Journal of Neurology* 134.Pt 3 (Mar. 2011), pp. 678–692.

[41] M. Ohgoh et al. “Altered Expression of Glutamate Transporters in Experimental Autoimmune Encephalomyelitis”. In: *Journal of Neuroimmunology* 125.1-2 (Apr. 2002), pp. 170–178.

[42] G. Sulkowski et al. “Modulation of Glutamate Transport and Receptor Binding by Glutamate Receptor Antagonists in EAE Rat Brain”. In: *PLoS ONE* 9.11 (Nov. 2014).

[43] K. Mitosek-Szewczyk et al. “Expression of Glutamate Transporters GLT-1 and GLAST in Different Regions of Rat Brain during the Course of Experimental Autoimmune Encephalomyelitis”. In: *Neuroscience* 155.1 (July 2008), pp. 45–52.

[44] T. Himi et al. “Role of Neuronal Glutamate Transporter in the Cysteine Uptake and Intracellular Glutathione Levels in Cultured Cortical Neurons”. In: *Journal of Neural Transmission (Vienna, Austria: 1996)* 110.12 (Dec. 2003), pp. 1337–1348.

[45] J. Zumkehr et al. “Ceftriaxone Ameliorates Tau Pathology and Cognitive Decline via Restoration of Glial Glutamate Transporter in a Mouse Model of Alzheimer’s Disease”. In: *Neurobiology of Aging* 36.7 (July 2015), pp. 2260–2271.

[46] S. Fan et al. “Ceftriaxone Improves Cognitive Function and Upregulates GLT-1-Related Glutamate-Glutamine Cycle in APP/PS1 Mice”. In: *Journal of Alzheimer’s disease: JAD* 66.4 (2018), pp. 1731–1743.

[47] D. Yernool et al. “Structure of a Glutamate Transporter Homologue from Pyrococcus Horikoshii”. In: *Nature* 431.7010 (Oct. 2004), pp. 811–818.

[48] A. Guskov et al. “Coupled Binding Mechanism of Three Sodium Ions and Aspartate in the Glutamate Transporter Homologue GltTk”. In: *Nature Communications* 7 (Nov. 2016), p. 13420.

[49] O. Boudker et al. “Coupling Substrate and Ion Binding to Extracellular Gate of a Sodium-Dependent Aspartate Transporter”. In: *Nature* 445.7126 (Jan. 2007), pp. 387–393.

[50] N. Zerangue and M. P. Kavanaugh. “Flux Coupling in a Neuronal Glutamate Transporter”. In: *Nature* 383.6601 (Oct. 1996), pp. 634–637.

[51] L. M. Levy, O. Warr, and D. Attwell. “Stoichiometry of the Glial Glutamate Transporter GLT-1 Expressed Inducibly in a Chinese Hamster Ovary Cell Line Selected for Low Endogenous Na+-Dependent Glutamate Uptake”. In: *The Journal of Neuroscience: The Official Journal of the Society for Neuroscience* 18.23 (Dec. 1998), pp. 9620–9628.

[52] S. G. Owe, P. Marcaggi, and D. Attwell. “The Ionic Stoichiometry of the GLAST Glutamate Transporter in Salamander Retinal Glia”. In: *The Journal of Physiology* 577.Pt 2 (Dec. 2006), pp. 591–599.

[53] G. Verdon et al. “Coupled Ion Binding and Structural Transitions along the Transport Cycle of Glutamate Transporters”. In: *eLife* 3 (May 2014). Ed. by B. Roux, e02283.

[54] P. J. Focke, P. Moenne-Loccoz, and H. P. Larsson. “Opposite Movement of the External Gate of a Glutamate Transporter Homolog upon Binding Co-transported Sodium Compared with Substrate”. In: *The Journal of Neuroscience: The Official Journal of the Society for Neuroscience* 31.16 (Apr. 2011), pp. 6255–6262.

[55] D. Kortzak et al. “Allosteric Gate Modulation Confers K+ Coupling in Glutamate Transporters”. In: *The EMBO Journal* 38.19 (Oct. 2019), e101468.

[56] V. Arkhipova, A. Guskov, and D. J. Slotboom. “Structural Ensemble of a Glutamate Transporter Homologue in Lipid Nanodisc Environment”. In: *Nature Communications* 11.1 (Feb. 2020), pp. 1–9.

[57] O. Boudker et al. “Coupling Substrate and Ion Binding to Extracellular Gate of a Sodium-Dependent Aspartate Transporter”. In: *Nature* 445.7126 (Jan. 2007), pp. 387–393.

[58] T. Bastug et al. “Position of the Third Na+ Site in the Aspartate Transporter GltPh and the Human Glutamate Transporter, EAAT1”. In: *PloS One* 7.3 (2012), e33058.

[59] C. Alleva et al. “Molecular Basis of Coupled Transport and Anion Conduction in Excitatory Amino Acid Transporters”. In: *Neurochemical Research* 47.1 (Jan. 2022), pp. 9–22.

[60] A. A. Garaeva et al. “Cryo-EM Structure of the Human Neutral Amino Acid Transporter ASCT2”. In: *Nature Structural & Molecular Biology* 25.6 (June 2018), pp. 515–521.

[61] S. Gendreau et al. “A Trimeric Quaternary Structure Is Conserved in Bacterial and Human Glutamate Transporters”. In: *The Journal of Biological Chemistry* 279.38 (Sept. 2004), pp. 39505–39512.

[62] D. Yernool et al. “Trimeric Subunit Stoichiometry of the Glutamate Transporters from Bacillus Caldotenax and Bacillus Stearothermophilus”. In: *Biochemistry* 42.44 (Nov. 2003), pp. 12981–12988.

[63] N. Reyes, C. Ginter, and O. Boudker. “Transport Mechanism of a Bacterial Homologue of Glutamate Transporters”. In: *Nature* 462.7275 (Dec. 2009), pp. 880–885.

[64] G. B. Erkens et al. “Unsynchronised Subunit Motion in Single Trimeric Sodium-Coupled Aspartate Transporters”. In: *Nature* 502.7469 (Oct. 2013), pp. 119–123.

[65] Y. Ruan et al. “Direct Visualization of Glutamate Transporter Elevator Mechanism by High-Speed AFM”. In: *Proceedings of the National Academy of Sciences* 114.7 (Feb. 2017), pp. 1584–1588.

[66] W. Zhou et al. “Large-Scale State-Dependent Membrane Remodeling by a Transporter Protein”. In: *eLife* 8 (Dec. 2019).

[67] D. Yernool et al. “Structure of a Glutamate Transporter Homologue from Pyrococcus Horikoshii”. In: *Nature* 431.7010 (Oct. 2004), pp. 811–818.

[68] N. Reyes, S. Oh, and O. Boudker. “Binding Thermodynamics of a Glutamate Transporter Homolog”. In: *Nature Structural & Molecular Biology* 20.5 (May 2013), pp. 634–640.

[69] R. M. Ryan, E. L. R. Compton, and J. A. Mindell. “Functional Characterization of a Na+-Dependent Aspartate Transporter from Pyrococcus Horikoshii”. In: *The Journal of Biological Chemistry* 284.26 (June 2009), pp. 17540–17548.

[70] C. Kutzner et al. “Computational Electrophysiology: The Molecular Dynamics of Ion Channel Permeation and Selectivity in Atomistic Detail”. In: *Biophysical Journal* 101.4 (Aug. 2011), pp. 809–817.

[71] N. Akyuz et al. “Transport Domain Unlocking Sets the Uptake Rate of an Aspartate Transporter”. In: *Nature* 518.7537 (Feb. 2015), pp. 68–73.

[72] G. Verdon and O. Boudker. “Crystal Structure of an Asymmetric Trimer of a Bacterial Glutamate Transporter Homologue”. In: *Nature structural & molecular biology* 19.3 (Feb. 2012), pp. 355–357.

[73] I. Chen et al. “Glutamate Transporters Have a Chloride Channel with Two Hydrophobic Gates”. In: *Nature* 591.7849 (Mar. 2021), pp. 327–331.

[74] M. J. Abraham et al. “GROMACS: High Performance Molecular Simulations through Multi-Level Parallelism from Laptops to Supercomputers”. In: *SoftwareX* 1–2 (Sept. 2015), pp. 19–25.

[75] S. Páll et al. “Tackling Exascale Software Challenges in Molecular Dynamics Simulations with GROMACS”. In: *Solving Software Challenges for Exascale*. Ed. by S. Markidis and E. Laure. Lecture Notes in Computer Science. Cham: Springer International Publishing, 2015, pp. 3–27. ISBN: 978-3-319-15976-8.

[76] J. Huang et al. “CHARMM36m: An Improved Force Field for Folded and Intrinsically Disordered Proteins”. In: *Nature Methods* 14.1 (Jan. 2017), pp. 71–73.

[77] B. Webb and A. Sali. “Comparative Protein Structure Modeling Using MODELLER”. In: *Current Protocols in Bioinformatics* 54 (June 2016), pp. 5.6.1–5.6.37.

[78] M. A. Lomize et al. “OPM Database and PPM Web Server: Resources for Positioning of Proteins in Membranes”. In: *Nucleic Acids Research* 40.Database issue (Jan. 2012), pp. D370–376.

[79] M. G. Wolf et al. “G_membed: Efficient Insertion of a Membrane Protein into an Equilibrated Lipid Bilayer with Minimal Perturbation”. In: *Journal of Computational Chemistry* 31.11 (2010), pp. 2169–2174.

[80] B. C. McIlwain, R. J. Vandenberg, and R. M. Ryan. “Transport Rates of a Glutamate Transporter Homologue Are Influenced by the Lipid Bilayer”. In: *The Journal of Biological Chemistry* 290.15 (Apr. 2015), pp. 9780–9788.

[81] J. Wang et al. “Observing Spontaneous, Accelerated Substrate Binding in Molecular Dynamics Simulations of Glutamate Transporters”. In: *PLoS ONE* 16.4 (Apr. 2021), e0250635.

[82] J.-P. Machtens et al. “Mechanisms of Anion Conduction by Coupled Glutamate Transporters”. In: *Cell* 160.3 (Jan. 2015), pp. 542–553.

[83] S. Stolzenberg, G. Khelashvili, and H. Weinstein. “Structural Intermediates in a Model of the Substrate Translocation Path of the Bacterial Glutamate Transporter Homologue GltPh”. In: *The Journal of Physical Chemistry. B* 116.18 (May 2012), pp. 5372–5383.

[84] H. J. C. Berendsen et al. “Molecular Dynamics with Coupling to an External Bath”. In: *The Journal of Chemical Physics* 81.8 (Oct. 1984), pp. 3684–3690.

[85] M. Parrinello and A. Rahman. “Polymorphic Transitions in Single Crystals: A New Molecular Dynamics Method”. In: *Journal of Applied Physics* 52.12 (Dec. 1981), pp. 7182–7190.

[86] G. Bussi, D. Donadio, and M. Parrinello. “Canonical Sampling through Velocity Rescaling”. In: *The Journal of Chemical Physics* 126.1 (Jan. 2007), p. 014101.

[87] B. Hess et al. “LINCS: A Linear Constraint Solver for Molecular Simulations”. In: *Journal of Computational Chemistry* 18.12 (1997), pp. 1463–1472.

[88] S. Miyamoto and P. A. Kollman. “Settle: An Analytical Version of the SHAKE and RATTLE Algorithm for Rigid Water Models”. In: *Journal of Computational Chemistry* 13.8 (1992), pp. 952–962.

[89] Schrödinger, LLC. "The PyMOL Molecular Graphics System, Version 1.8". Nov. 2015.

[90] J. Lidmar. "Improving the Efficiency of Extended Ensemble Simulations: The Accelerated Weight Histogram Method". In: *Physical Review E* 85.5 (May 2012), p. 056708.

[91] V. Lindahl, J. Lidmar, and B. Hess. "Accelerated Weight Histogram Method for Exploring Free Energy Landscapes". In: *The Journal of Chemical Physics* 141.4 (July 2014), p. 044110. arXiv: 1407.7415.

[92] A. Laio and M. Parrinello. "Escaping Free-Energy Minima". In: *Proceedings of the National Academy of Sciences* 99.20 (Oct. 2002), pp. 12562–12566.

[93] G. M. Torrie and J. P. Valleau. "Nonphysical Sampling Distributions in Monte Carlo Free-Energy Estimation: Umbrella Sampling". In: *Journal of Computational Physics* 23.2 (Feb. 1977), pp. 187–199.

[94] A. Amadei, A. B. M. Linssen, and H. J. C. Berendsen. "Essential Dynamics of Proteins". In: *Proteins: Structure, Function, and Bioinformatics* 17.4 (1993), pp. 412–425.

[95] A. Amadei et al. "An Efficient Method for Sampling the Essential Subspace of Proteins". In: *Journal of Biomolecular Structure and Dynamics* 13.4 (Feb. 1996), pp. 615–625.

[96] C. R. Harris et al. "Array Programming with NumPy". In: *Nature* 585.7825 (Sept. 2020), pp. 357–362.

[97] R. J. Gowers et al. "MDAnalysis: A Python Package for the Rapid Analysis of Molecular Dynamics Simulations". In: *Proceedings of the 15th Python in Science Conference* (2016), pp. 98–105.

[98] N. Michaud-Agrawal et al. "MDAnalysis: A Toolkit for the Analysis of Molecular Dynamics Simulations". In: *Journal of Computational Chemistry* 32.10 (2011), pp. 2319–2327.

[99] L. Molgedey and H. G. Schuster. "Separation of a Mixture of Independent Signals Using Time Delayed Correlations". In: *Physical Review Letters* 72.23 (June 1994), pp. 3634–3637.

[100] G. Pérez-Hernández et al. "Identification of Slow Molecular Order Parameters for Markov Model Construction". In: *The Journal of Chemical Physics* 139.1 (July 2013), p. 015102.

[101] M. K. Scherer et al. “PyEMMA 2: A Software Package for Estimation, Validation, and Analysis of Markov Models”. In: *Journal of Chemical Theory and Computation* 11.11 (Nov. 2015), pp. 5525–5542.

[102] F. Noé and F. Nüske. “A Variational Approach to Modeling Slow Processes in Stochastic Dynamical Systems”. In: *Multiscale Modeling & Simulation* 11.2 (Jan. 2013), pp. 635–655.

[103] J.-H. Prinz et al. “Markov Models of Molecular Kinetics: Generation and Validation”. In: *The Journal of Chemical Physics* 134.17 (May 2011), p. 174105.

[104] N. Singhal and V. S. Pande. “Error Analysis and Efficient Sampling in Markovian State Models for Molecular Dynamics”. In: *The Journal of Chemical Physics* 123.20 (Nov. 2005), p. 204909.

[105] A. Mardt et al. “VAMPnets for Deep Learning of Molecular Kinetics”. In: *Nature Communications* 9.1 (Jan. 2018), p. 5.

[106] B. O. Koopman. “Hamiltonian Systems and Transformation in Hilbert Space”. In: *Proceedings of the National Academy of Sciences* 17.5 (May 1931), pp. 315–318.

[107] I. Mezić. “Spectral Properties of Dynamical Systems, Model Reduction and Decompositions”. In: *Nonlinear Dynamics* 41.1 (Aug. 2005), pp. 309–325.

[108] M. O. Williams, I. G. Kevrekidis, and C. W. Rowley. “A Data–Driven Approximation of the Koopman Operator: Extending Dynamic Mode Decomposition”. In: *Journal of Nonlinear Science* 25.6 (Dec. 2015), pp. 1307–1346.

[109] I. Horenko et al. “Data-Based Parameter Estimation of Generalized Multidimensional Langevin Processes”. In: *Physical Review E* 76.1 (July 2007), p. 016706.

[110] H. Wu and F. Noé. “Variational Approach for Learning Markov Processes from Time Series Data”. In: *arXiv:1707.04659 [math, stat]* (Aug. 2019). arXiv: `1707.04659 [math, stat]`.

[111] M. Hoffmann et al. “Deeptime: A Python Library for Machine Learning Dynamical Models from Time Series Data”. In: *Machine Learning: Science and Technology* (2021).

[112] P. E. Hart, N. J. Nilsson, and B. Raphael. “A Formal Basis for the Heuristic Determination of Minimum Cost Paths”. In: *IEEE Transactions on Systems Science and Cybernetics* 4.2 (July 1968), pp. 100–107.

[113] F. Pedregosa et al. “Scikit-Learn: Machine Learning in Python”. In: *Journal of Machine Learning Research* 12.85 (2011), pp. 2825–2830.

[114] L. Buitinck et al. “API Design for Machine Learning Software: Experiences from the Scikit-Learn Project”. In: *arXiv:1309.0238 [cs]* (Sept. 2013). arXiv: 1309.0238 [cs].

[115] M. Ankerst et al. “OPTICS: Ordering Points to Identify the Clustering Structure”. In: *ACM SIGMOD Record* 28.2 (June 1999), pp. 49–60.

[116] J. MacQueen. “Some Methods for Classification and Analysis of Multivariate Observations”. In: *Proceedings of the Fifth Berkeley Symposium on Mathematical Statistics and Probability, Volume 1: Statistics* 5.1 (Jan. 1967), pp. 281–298.

[117] R. Briones et al. “GROmaρs: A GROMACS-Based Toolset to Analyze Density Maps Derived from Molecular Dynamics Simulations”. In: *Biophysical Journal* 116.1 (Jan. 2019), pp. 4–11.

[118] O. Jardetzky. “Simple Allosteric Model for Membrane Pumps”. In: *Nature* 211.5052 (Aug. 1966), pp. 969–970.

[119] Y. Huang et al. “Structure and Mechanism of the Glycerol-3-Phosphate Transporter from Escherichia Coli”. In: *Science* (Aug. 2003).

[120] J. Abramson et al. “Structure and Mechanism of the Lactose Permease of Escherichia Coli”. In: *Science* (Aug. 2003).

[121] L. R. Forrest and G. Rudnick. “The Rocking Bundle: A Mechanism for Ion-Coupled Solute Flux by Symmetrical Transporters”. In: *Physiology (Bethesda, Md.)* 24 (Dec. 2009), pp. 377–386.

[122] G. Verdon and O. Boudker. “Crystal Structure of an Asymmetric Trimer of a Bacterial Glutamate Transporter Homolog”. In: *Nature Structural & Molecular Biology* 19.3 (Feb. 2012), pp. 355–357.

[123] Y. Gu et al. “Molecular Simulations Elucidate the Substrate Translocation Pathway in a Glutamate Transporter”. In: *Proceedings of the National Academy of Sciences of the United States of America* 106.8 (Feb. 2009), pp. 2589–2594.

[124] G. Grazioso et al. “Investigating the Mechanism of Substrate Uptake and Release in the Glutamate Transporter Homologue GltPh through Metadynamics Simulations”. In: *Journal of the American Chemical Society* 134.1 (Jan. 2012), pp. 453–463.

[125] E. Zomot and I. Bahar. "Intracellular Gating in an Inward-facing State of Aspartate Transporter GltPh Is Regulated by the Movements of the Helical Hairpin HP2 *". In: *Journal of Biological Chemistry* 288.12 (Mar. 2013), pp. 8231–8237.

[126] C. Alleva et al. "Na^+-Dependent Gate Dynamics and Electrostatic Attraction Ensure Substrate Coupling in Glutamate Transporters". In: *Science Advances* 6.47 (2020), eaba9854. eprint: `https://www.science.org/doi/pdf/10.1126/sciadv.aba9854`.

[127] D. E. Bergles, A. V. Tzingounis, and C. E. Jahr. "Comparison of Coupled and Uncoupled Currents during Glutamate Uptake by GLT-1 Transporters". In: *The Journal of Neuroscience: The Official Journal of the Society for Neuroscience* 22.23 (Dec. 2002), pp. 10153–10162.

[128] J.-P. Machtens, P. Kovermann, and C. Fahlke. "Substrate-Dependent Gating of Anion Channels Associated with Excitatory Amino Acid Transporter 4". In: *The Journal of Biological Chemistry* 286.27 (July 2011), pp. 23780–23788.

[129] T. S. Otis and M. P. Kavanaugh. "Isolation of Current Components and Partial Reaction Cycles in the Glial Glutamate Transporter EAAT2". In: *The Journal of Neuroscience: The Official Journal of the Society for Neuroscience* 20.8 (Apr. 2000), pp. 2749–2757.

[130] A. Accardi and C. Miller. "Secondary Active Transport Mediated by a Prokaryotic Homologue of ClC Cl- Channels". In: *Nature* 427.6977 (Feb. 2004), pp. 803–807.

[131] H. Jayaram et al. "Ion Permeation through a Cl–Selective Channel Designed from a CLC Cl-/H+ Exchanger". In: *Proceedings of the National Academy of Sciences* 105.32 (2008), pp. 11194–11199. eprint: `https://www.pnas.org/content/105/32/11194.full.pdf`.

[132] Y. Huang et al. "Use of Paramagnetic 19F NMR to Monitor Domain Movement in a Glutamate Transporter Homolog". In: *Nature Chemical Biology* 16.9 (Sept. 2020), pp. 1006–1012.

[133] G. Heinzelmann and S. Kuyucak. "Molecular Dynamics Simulations of the Mammalian Glutamate Transporter EAAT3". In: *PLOS ONE* 9.3 (Mar. 2014), e92089.

[134] A. A. Garaeva et al. "A One-Gate Elevator Mechanism for the Human Neutral Amino Acid Transporter ASCT2". In: *Nature Communications* 10.1 (July 2019), p. 3427.

[135] C. Jarzynski. "Nonequilibrium Equality for Free Energy Differences". In: *Physical Review Letters* 78.14 (Apr. 1997), pp. 2690–2693.

[136] B. L. de Groot et al. "Towards an Exhaustive Sampling of the Configurational Spaces of the Two Forms of the Peptide Hormone Guanylin". In: *Journal of Biomolecular Structure and Dynamics* 13.5 (Apr. 1996), pp. 741–751.

[137] B. L. de Groot et al. "An Extended Sampling of the Configurational Space of HPr fromE. Coli". In: *Proteins: Structure, Function, and Genetics* 26.3 (Nov. 1996), pp. 314–322.

[138] A. Barducci, G. Bussi, and M. Parrinello. "Well-Tempered Metadynamics: A Smoothly Converging and Tunable Free-Energy Method". In: *Physical Review Letters* 100.2 (Jan. 2008), p. 020603.

[139] P. Hänggi, P. Talkner, and M. Borkovec. "Reaction-Rate Theory: Fifty Years after Kramers". In: *Reviews of Modern Physics* 62.2 (Apr. 1990), pp. 251–341.

[140] J. Keck. "Statistical Investigation of Dissociation Cross-Sections for Diatoms". In: *Discussions of the Faraday Society* 33.0 (Jan. 1962), pp. 173–182.

[141] J. C. Keck. "Variational Theory of Reaction Rates". In: *Advances in Chemical Physics*. John Wiley & Sons, Ltd, 1967, pp. 85–121. ISBN: 978-0-470-14015-4.

[142] D. Chandler. "Introduction to Modern Statistical". In: *Mechanics. Oxford University Press, Oxford, UK* 5 (1987).

[143] M. Shirts and V. S. Pande. "COMPUTING: Screen Savers of the World Unite!" In: *Science (New York, N.Y.)* 290.5498 (Dec. 2000), pp. 1903–1904.

[144] I. Buch et al. "High-Throughput All-Atom Molecular Dynamics Simulations Using Distributed Computing". In: *Journal of Chemical Information and Modeling* 50.3 (Mar. 2010), pp. 397–403.

[145] C. Kutzner et al. "Best Bang for Your Buck: GPU Nodes for GROMACS Biomolecular Simulations". In: *Journal of Computational Chemistry* 36.26 (2015), pp. 1990–2008.

[146] B. Kohnke, C. Kutzner, and H. Grubmüller. "A GPU-Accelerated Fast Multipole Method for GROMACS: Performance and Accuracy". In: *Journal of Chemical Theory and Computation* 16.11 (Nov. 2020), pp. 6938–6949.

[147] D. K. Shenfeld et al. "Minimizing Thermodynamic Length to Select Intermediate States for Free-Energy Calculations and Replica-Exchange Simulations". In: *Physical Review E* 80.4 (Oct. 2009), p. 046705.

[148] B. E. Husic and V. S. Pande. “Markov State Models: From an Art to a Science”. In: *Journal of the American Chemical Society* 140.7 (Feb. 2018), pp. 2386–2396.

[149] R. Zwanzig. “From Classical Dynamics to Continuous Time Random Walks”. In: *Journal of Statistical Physics* 30.2 (Feb. 1983), pp. 255–262.

[150] P. Hänggi and P. Talkner. “Memory Index of First-Passage Time: A Simple Measure of Non-Markovian Character”. In: *Physical Review Letters* 51.25 (Dec. 1983), pp. 2242–2245.

[151] D. Shalloway. “Macrostates of Classical Stochastic Systems”. In: *The Journal of Chemical Physics* 105.22 (Dec. 1996), pp. 9986–10007.

[152] N. Akyuz et al. “Transport Dynamics in a Glutamate Transporter Homologue”. In: *Nature* 502.7469 (Oct. 2013), pp. 114–118.

[153] J. Setiadi and S. Kuyucak. “Elucidation of the Role of a Conserved Methionine in Glutamate Transporters and Its Implication for Force Fields”. In: *The Journal of Physical Chemistry. B* 121.41 (Oct. 2017), pp. 9526–9531.

[154] E. Zomot and I. Bahar. “Intracellular Gating in an Inward-Facing State of Aspartate Transporter Glt(Ph) Is Regulated by the Movements of the Helical Hairpin HP2”. In: *The Journal of Biological Chemistry* 288.12 (Mar. 2013), pp. 8231–8237.

[155] J. DeChancie, I. H. Shrivastava, and I. Bahar. “The Mechanism of Substrate Release by the Aspartate Transporter GltPh: Insights from Simulations”. In: *Molecular bioSystems* 7.3 (Mar. 2011), pp. 832–842.

[156] S. Venkatesan et al. “Refinement of the Central Steps of Substrate Transport by the Aspartate Transporter GltPh: Elucidating the Role of the Na2 Sodium Binding Site”. In: *PLoS computational biology* 11.10 (Oct. 2015), e1004551.

[157] N. Akyuz et al. “Transport Dynamics in a Glutamate Transporter Homologue”. In: *Nature* 502.7469 (Oct. 2013), pp. 114–118.

[158] A. A. Garaeva et al. “Cryo-EM Structure of the Human Neutral Amino Acid Transporter ASCT2”. In: *Nature Structural & Molecular Biology* 25.6 (June 2018), pp. 515–521.

[159] V. Arkhipova, A. Guskov, and D. J. Slotboom. “Structural Ensemble of a Glutamate Transporter Homologue in Lipid Nanodisc Environment”. In: *Nature Communications* 11.1 (Feb. 2020), p. 998.

[160] D. Ewers et al. “Induced Fit Substrate Binding to an Archeal Glutamate Transporter Homologue”. In: *Proceedings of the National Academy of Sciences of the United States of America* 110.30 (July 2013), pp. 12486–12491.

[161] M. Hirschi, Z. L. Johnson, and S.-Y. Lee. “Visualizing Multistep Elevator-like Transitions of a Nucleoside Transporter”. In: *Nature* 545.7652 (May 2017), pp. 66–70.

[162] G. B. Erkens et al. “Unsynchronised Subunit Motion in Single Trimeric Sodium-Coupled Aspartate Transporters”. In: *Nature* 502.7469 (Oct. 2013), pp. 119–123.

[163] W. E. and E. Vanden-Eijnden. “Towards a Theory of Transition Paths”. In: *Journal of Statistical Physics* 123.3 (May 2006), p. 503.

[164] P. Metzner, C. Schütte, and E. Vanden-Eijnden. “Transition Path Theory for Markov Jump Processes”. In: *Multiscale Modeling & Simulation* 7.3 (Jan. 2009), pp. 1192–1219.

[165] F. Noé et al. “Constructing the Equilibrium Ensemble of Folding Pathways from Short Off-Equilibrium Simulations”. In: *Proceedings of the National Academy of Sciences* 106.45 (Nov. 2009), pp. 19011–19016.

[166] H. P. Koch and H. P. Larsson. “Small-Scale Molecular Motions Accomplish Glutamate Uptake in Human Glutamate Transporters”. In: *The Journal of Neuroscience: The Official Journal of the Society for Neuroscience* 25.7 (Feb. 2005), pp. 1730–1736.

[167] H. P. Koch, R. L. Brown, and H. P. Larsson. “The Glutamate-Activated Anion Conductance in Excitatory Amino Acid Transporters Is Gated Independently by the Individual Subunits”. In: *Journal of Neuroscience* 27.11 (Mar. 2007), pp. 2943–2947.

[168] X. Wang and O. Boudker. “Large Domain Movements through the Lipid Bilayer Mediate Substrate Release and Inhibition of Glutamate Transporters”. In: *eLife* 9 (Nov. 2020). Ed. by L. R. Forrest, R. W. Aldrich, and E. R. Geertsma, e58417.

[169] P. G. Hoel et al. “Introduction to Stochastic Processes”. In: *IEEE Transactions on Systems, Man, and Cybernetics* SMC-3.5 (Sept. 1973), pp. 533–533.

[170] D. Torres-Salazar and C. Fahlke. “Intersubunit Interactions in EAAT4 Glutamate Transporters”. In: *The Journal of Neuroscience: The Official Journal of the Society for Neuroscience* 26.28 (July 2006), pp. 7513–7522.

[171] P. Kovermann et al. “A Conserved Aspartate Determines Pore Properties of Anion Channels Associated with Excitatory Amino Acid Transporter 4 (EAAT4)”. In: *The Journal of Biological Chemistry* 285.31 (July 2010), pp. 23676–23686.

[172] A. Leinenweber et al. “Regulation of Glial Glutamate Transporters by C-terminal Domains”. In: *The Journal of Biological Chemistry* 286.3 (Jan. 2011), pp. 1927–1937.

[173] C. B. Divito et al. “Glial and Neuronal Glutamate Transporters Differ in the Na+ Requirements for Activation of the Substrate-Independent Anion Conductance”. In: *Frontiers in Molecular Neuroscience* 10 (2017), p. 150.

[174] S. Picaud et al. “Cone Photoreceptors Respond to Their Own Glutamate Release in the Tiger Salamander”. In: *Proceedings of the National Academy of Sciences of the United States of America* 92.20 (Sept. 1995), pp. 9417–9421.

[175] V. Untiet et al. “Glutamate Transporter-Associated Anion Channels Adjust Intracellular Chloride Concentrations during Glial Maturation”. In: *Glia* 65.2 (Feb. 2017), pp. 388–400.

[176] M. Engels et al. “Glial Chloride Homeostasis Under Transient Ischemic Stress”. In: *Frontiers in Cellular Neuroscience* 15 (2021), p. 735300.

[177] P. Kovermann et al. “Increased Glutamate Transporter-Associated Anion Currents Cause Glial Apoptosis in Episodic Ataxia 6”. In: *Brain Communications* 2.1 (Mar. 2020), fcaa022.

[178] J. C. Jen et al. “Mutation in the Glutamate Transporter EAAT1 Causes Episodic Ataxia, Hemiplegia, and Seizures”. In: *Neurology* 65.4 (Aug. 2005), pp. 529–534.

[179] J. L. Arriza et al. “Excitatory Amino Acid Transporter 5, a Retinal Glutamate Transporter Coupled to a Chloride Conductance”. In: *Proceedings of the National Academy of Sciences of the United States of America* 94.8 (Apr. 1997), pp. 4155–4160.

[180] A. Gameiro et al. “The Discovery of Slowness: Low-Capacity Transport and Slow Anion Channel Gating by the Glutamate Transporter EAAT5”. In: *Biophysical Journal* 100.11 (June 2011), pp. 2623–2632.

[181] N. Schneider et al. “Functional Properties of the Retinal Glutamate Transporters GLT-1c and EAAT5 *”. In: *Journal of Biological Chemistry* 289.3 (Jan. 2014), pp. 1815–1824.

[182] V. Untiet et al. “Glutamate Transporter-Associated Anion Channels Adjust Intracellular Chloride Concentrations during Glial Maturation”. In: *Glia* 65.2 (Feb. 2017), pp. 388–400.

[183] N. Winter, P. Kovermann, and C. Fahlke. “A Point Mutation Associated with Episodic Ataxia 6 Increases Glutamate Transporter Anion Currents”. In: *Brain* 135.11 (Nov. 2012), pp. 3416–3425.

[184] J. L. Trick et al. “Functional Annotation of Ion Channel Structures by Molecular Simulation”. In: *Structure(London, England:1993)* 24.12 (Dec. 2016), pp. 2207–2216.

[185] B. Kolen et al. “An Amino-Terminal Point Mutation Increases EAAT2 Anion Currents without Affecting Glutamate Transport Rates”. In: *The Journal of Biological Chemistry* 295.44 (Oct. 2020), pp. 14936–14947.

[186] N. MacAulay et al. “Water Transport by the Human Na+-Coupled Glutamate Cotransporter Expressed in Xenopus Oocytes”. In: *The Journal of Physiology* 530.3 (2001), pp. 367–378.

[187] R. J. Vandenberg et al. “Water and Urea Permeation Pathways of the Human Excitatory Amino Acid Transporter EAAT1”. In: *Biochemical Journal* 439.2 (Oct. 2011), pp. 333–340.

[188] S. A. Picaud et al. “Glutamate-Gated Chloride Channel with Glutamate-Transporter-like Properties in Cone Photoreceptors of the Tiger Salamander”. In: *Journal of Neurophysiology* (Oct. 1995).

Eidesstattliche Versicherung

Ich versichere an Eides Statt, dass die Dissertation von mir selbständig und ohne unzulässige fremde Hilfe unter Beachtung der „Grundsätze zur Sicherung guter wissenschaftlicher Praxis an der Heinrich-Heine-Universität Düsseldorf“ erstellt worden ist.

Ort, Datum	Felix Niklas Groß-Esser